MOUNTAIN-PLAINS CONSORTIUM

MPC 24-519 | T.J. Hansen and M.W. Halling

DURABLE AND CONSTRUCTIBLE MATERIALS IN GLASS REINFORCED CONCRETE TO EFFICIENTLY ACCOMMODATE MAGNETIC FIELDS

A University Transportation Center sponsored by the U.S. Department of Transportation serving the Mountain-Plains Region. Consortium members:

Colorado State University
North Dakota State University
South Dakota State University
University of Colorado Denver
University of Denver
University of Utah
Utah State University
University of Wyoming

Technical Report Documentation Page

1. Report No.
MPC-634

2. Government Accession No.

3. Recipient's Catalog No.

4. Title and Subtitle

Durable and Constructible Materials in Glass Reinforced Concrete to Efficiently Accommodate Magnetic Fields

5. Report Date
March 2024

6. Performing Organization Code

7. Author(s)
Thaddeus J. Hansen
Marvin W. Halling

8. Performing Organization Report No.
MPC 24-519

9. Performing Organization Name and Address

Dept. of Civil and Environmental Engineering
Utah State University
4110 Old Main Hill
Logan, UT 84321

10. Work Unit No. (TRAIS)

11. Contract or Grant No.

12. Sponsoring Agency Name and Address

Mountain-Plains Consortium
North Dakota State University
PO Box 6050, Fargo, ND 58108

13. Type of Report and Period Covered
Final Report

14. Sponsoring Agency Code

15. Supplementary Notes

Supported by a grant from the US DOT, University Transportation Centers Program

16. Abstract

Inductive power transfer systems (IPTS) embedded in concrete pavement panels allow EVs to charge their batteries while in motion. Four prototype concrete slabs were constructed and monitored during high-cycle fatigue loading. After the fatigue tests, each slab was subjected to a static load until failure. Traditional metallic reinforcement was not an option due to the adverse effects of the magnetic field produced by the IPTS.

During the fatigue testing, all alternative slabs experienced differing degrees of cracking. The data from strain gauges were used to compare the deformation due to fatigue damage that occurred in each slab. In addition to the physical testing of the concrete slabs, each alternative slab was modeled in a 3D finite element analysis (FEA) program. The results of the FEA models provided the theoretical ultimate strength of each test slab before they were subjected to fatigue damage; these results were compared with the ultimate residual strengths of the test slabs obtained during physical testing. The data obtained during this research suggest there are several viable top mat reinforcement alternatives, and the FRP grid used as top mat reinforcement provided the greatest durability for the concrete slabs.

17. Key Word

coils (electromagnetism), durability, electromagnetic fields, embedment (building), pavements, test tracks

18. Distribution Statement
Public distribution

19. Security Classif. (of this report)
Unclassified

20. Security Classif. (of this page)
Unclassified

21. No. of Pages
156

22. Price
n/a

Form DOT F 1700.7 (8-72) Reproduction of completed page authorized

Durable and Constructible Materials in Glass Reinforced Concrete to Efficiently Accommodate Magnetic Fields

Thaddeus J. Hansen
Marvin W. Halling

Department of Civil and Environmental Engineering
Utah State University
Logan, Utah 84321

March 2024

Acknowledgments

This project is funded by the ASPIRE National Science Foundation (NSF) Engineering Research Center and Mountain-Plains Consortium (MPC).

Disclaimer

ABSTRACT

Inductive power transfer systems (IPTS) embedded in concrete pavement panels allow EVs to charge their batteries while in motion. Four prototype concrete slabs were constructed and monitored during high-cycle fatigue loading. After the fatigue tests, each slab was subjected to a static load until failure. Traditional metallic reinforcement was not an option due to the adverse effects of the magnetic field produced by the IPTS.

During the fatigue testing, all alternative slabs experienced differing degrees of cracking. The data from strain gauges were used to compare the deformation due to fatigue damage that occurred in each slab. In addition to the physical testing of the concrete slabs, each alternative slab was modeled in a 3D finite element analysis (FEA) program. The results of the FEA models provided the theoretical ultimate strength of each test slab before they were subjected to fatigue damage; these results were compared with the ultimate residual strengths of the test slabs obtained during physical testing. The data obtained during this research suggest there are several viable top mat reinforcement alternatives, and the FRP grid used as top mat reinforcement provided the greatest durability for the concrete slabs.

TABLE OF CONTENTS

LIST OF TABLES

LIST OF FIGURES

LIST OF SYMBOLS AND NOTATION

β_1	Stress block factor
δ	Deflection
δ_i	Extensometer displacement at the i-th data point
$\Delta\varepsilon$	Difference in tensile strain between start and end data points
$\Delta\sigma$	Difference in tensile stress between start and end data points
ε_{cu}	Ultimate concrete strain
ε_{fu}	FRP rupture strain
ε_i	Tensile strain at the i-th data point
$\mu\varepsilon$	Microstrain
ρ_f	Design FRP reinforcement ratio
ρ_{fb}	Balanced reinforcement ratio
σ	Applied maximum stress level
$\sigma_{applied}$	Maximum applied stress in the calibration beam
σ_i	Tensile stress at the i-th data point
a	Depth of equivalent stress block
A	Cross-sectional area of test specimen
A_f	Area of tensile FRP reinforcement
A_s	Area of tension reinforcement
b	Width of the compression face of the member
c	Distance from the extreme compression fiber to the neutral axis
c_b	Depth to neutral axis at balanced condition
d	Distance from the extreme compression fiber to the centroid of tension reinforcement
E	Modulus of elasticity
E_f	Design modulus of elasticity of FRP
f'_c	Compressive strength of concrete
f_f	FRP tensile stress
f_{fu}	Design tensile strength of FRP
F_j	Applied load corresponding to $CMOD_j$
$f_{R,j}$	Residual flexural tensile strength corresponding to $CMOD_j$
F_{tu}	Ultimate tensile strength
f_y	Yield stress of tension reinforcement
h_{sp}	Distance between the top of the notch and the top of the specimen
I	Moment of inertia of specimen
K_1	Correction factor for source of aggregate
l	Span length
L	Span length
L_g	Extensometer gage length
$M_{applied}$	Moment applied to calibration beam
M_n	Nominal flexural resistance
MOR_{beam}	Modulus of rupture of the concrete

N	Fatigue life measured in cycles
N_f	Number of fatigue cycles until failure
$P_{applied}$	Load applied to calibration beam
P_i	Applied force at the i-th data point
P_{max}	Maximum applied force prior to failure
P_{model}	Expected failure load predicted by FEA model
$P_{physical}$	Measured failure load during physical testing
P_{ult}	Estimated ultimate load
R	Calculated modulus of rupture
r	Loading rate
S	Rate of increase in the maximum stress on the tension face
S_m	Section modulus of calibration beam
S_{max}	Maximum tensile fatigue stress in fatigue load cycle
S_{min}	Minimum tensile fatigue stress in fatigue load cycle
V_{out}	Output voltage
w	Weight of specimen per lineal foot
w_c	Unit weight of concrete

LIST OF ABBREVIATIONS

AASHTO	American Association of Highway and Transportation Officials
ACI	American Concrete Institute
AR	Alkali Resistant
ASTM	American Society of Testing and Materials
CFRP	Carbon Fiber Reinforced Polymer
CMOD	Crack-Mouth Opening Displacement
EN	European Standards
EV	Electric Vehicle
EVR	Electric Vehicle and Roadway
FEA	Finite Element Analysis
FHWA	Federal Highway Administration
FRC	Fiber Reinforced Concrete
FRP	Fiber Reinforced Plastic
FRP	Fiber Reinforced Polymer
FS	Factor of Safety
GFRP	Glass Fiber Reinforced Polymer
GGF	General Gauge Factor
HM	High Modulus
HRC	Hybrid Reinforced Concrete
HT	High Tensile Strength
IPT	Inductive Power Transfer
IPTS	Inductive Power Transfer System(s)
K	Modulus of Subgrade Reaction
OSB	Oriented Strand Board
SMASH	Systems, Materials, and Structural Health
USU	Utah State University
WPT	Wireless Power Transfer

EXECUTIVE SUMMARY

Electric vehicles (EVs) are continually becoming a larger portion of the vehicular fleet on a national and global level. Despite their growth in popularity, several challenges still exist that hinder the practicality and the public's acceptance of EVs. The limited travel range of EVs, lack of consistent charging stations, and required time to charge EVs are at the forefront of these challenges. The use of inductive power transfer systems (IPTS) may be part of the solution to the afore-mentioned issues.

IPTS embedded in concrete pavement panels allow EVs to charge their batteries while in motion. In order to justify the implementation of IPTS in concrete pavement panels, it must be shown that the concrete pavement panels will be durable enough to protect the electronic equipment within them. The purpose of this research is to investigate alternative reinforcement options for the top mat of the concrete pavement panels to ensure the proper function of the electronics while increasing the durability and longevity of the concrete panels.

Four prototype concrete slabs were constructed and monitored during high-cycle fatigue loading. The fatigue cycling used a sinusoidal 2 Hz wave to simulate traffic for a total of 500,000 cycles. After the fatigue tests, each slab was subjected to a static load until failure. The four alternative slabs were as follows: (1) a control slab with no reinforcement in the top of the slab, (2) a slab constructed with fiber-reinforced concrete containing synthetic microfibers, (3) a slab with a top mat of glass fiber reinforced polymer (GFRP) deformed rebar, and (4) a slab with a fiberglass reinforced plastic (FRP) grate used as the top mat of reinforcement. Traditional metallic reinforcement was not an option due to the adverse effects of the magnetic field produced by the IPTS.

During the fatigue testing, all alternative slabs experienced differing degrees of cracking. External strain gauges were used to monitor the slabs before and after the initial cracking caused by the fatigue testing. The data from the strain gauges were used to compare the deformation due to fatigue damage that occurred in each slab. In addition to the physical testing of the concrete slabs, each alternative slab was modeled in a 3D finite element analysis (FEA) program. The results of the FEA models provided the theoretical ultimate strength of each test slab before they were subjected to fatigue damage; these results were compared with the ultimate residual strengths of the test slabs obtained during physical testing. The data obtained during this research suggest there are several viable top mat reinforcement alternatives, and the FRP grid used as top mat reinforcement provided the greatest durability for the concrete slabs.

1. INTRODUCTION

1.1 Problem Statement

Traditional gas vehicles cause greenhouse gas emissions through conventional gasoline and diesel fuel, which contribute to global warming and climate change. Producing the fuel to power vehicles requires large amounts of energy and natural resources, leading to increased levels of air and water pollution, habitat destruction, and depletion of non-renewable resources. Traditional motor vehicles also produce pollutants and particulate matter that can directly harm human health. These issues, among others, are bringing a transition to electric vehicles (EVs).

Although the need for EVs is easily justifiable, there are several drawbacks that hinder the public from transitioning to EVs. The limited range of EVs and relatively long charging times make their use impractical to users who travel long distances. In addition, the lack of charging infrastructure in many areas compounds the issue. Although other industries are making several advances to combat the drawbacks that EVs face, this research focuses on several design configurations of inductive power transfer systems (IPTS) embedded in concrete roadway panels.

Embedded IPTS have the capability to charge EVs while they are moving. Creating a system that can efficiently accomplish wireless power transfer, is safe for users, and is durable under the stress induced by traveling vehicles is a multidisciplinary effort. Investigating the structural integrity and durability of the concrete pavement panels that house the IPTS is one of several major parts of the ongoing research efforts.

Structural voids within the concrete panels are created by the electronic equipment required for the IPTS. These voids weaken the panels and create areas of concentrated stress. Another structural issue introduced by the IPTS is related to the magnetic fields and large amounts of heat they generate. Due to the magnetism and heat, traditional metallic reinforcing is not effective in the upper portions of the concrete panels. For these reasons, alternative options for the top mat reinforcement in concrete pavement panels with embedded IPTS need to be investigated to ensure their durability and resiliency throughout the service life of the pavement.

1.2 Objective

The purpose of this research is to investigate embedded IPTS configurations, which can function efficiently and durably. Top mat reinforcement alternatives for embedded wireless charging concrete pavement are used in this research. To accomplish this task, multiple alternatives were constructed and subjected to high-cycle fatigue loading produced by a hydraulic ram to simulate vehicular travel over an extended period of time. The parameters of *high-cycle* fatigue loading are defined in Section 2.5 of this report. Because the objective of this experiment is to focus on the durability and longevity of the pavement panels, they contained “dummy” IPTS that did not function. The sole purpose of the dummy IPTS was to emulate the structural voids created by an authentic IPTS. Each test panel was monitored by external strain gauges throughout the fatigue testing. Strain datasets from each alternative were compared to one another.

After the fatigue testing was complete, each test panel was subjected to monotonic loading until failure to ascertain their residual ultimate strengths after the incurred fatigue damage. The residual ultimate strength was used for two primary purposes. First, it was used to directly compare the residual structural strength of the composite test panels with different reinforcement alternatives. The ultimate residual strength for each test panel was also compared to an expected ultimate strength value without any fatigue damage obtained from a 3D finite element analysis (FEA). Ultimately, the primary goal of this research is to present the best tested alternative for top mat reinforcing in concrete pavement panels with embedded IPTS that can be used in the future production of said panels. A secondary goal is to suggest any additional alternatives for future research that may be discovered during the research process.

1.3 Outline

Chapter 2 encompasses a review of relevant research on topics such as electrified roadways, alternatives to metallic reinforcement in concrete, fiber reinforced concrete (FRC), glass fiber reinforced polymer (GFRP) reinforcement, the flexural and fatigue response reinforced concrete, and the modulus of subgrade reaction. An abundance of research has been previously completed on many of these topics, and only a small portion of it will be covered in this document. The testing procedure used for this research experiment will then be described in Chapter 3. The testing procedure will include the outline of the experimental program, the details of the concrete test panels, and the details of the testing set-up.

Following the testing procedure, methods of data analysis will be described in Chapter 4. The equipment used and its methods of calibration will be presented, as well as the details of the 3D FEA model used to verify the data obtained from the physical models. Chapter 5 will contain both discussion and comparison of the results obtained during the experimental program. Chapter 6 will present a summary of the research experiment and provide recommendations based on its findings.

2. LITERATURE REVIEW

2.1 Historical Background

2.1.1 Electrified Roadways

Sustainable development is defined as development that meets the needs of the present without compromising the ability of future generations to meet their own needs, and its origins can be traced back decades. The World Commission on Environment and Development produced a report that contained a summary of the concerns, challenges, and current endeavors associated with sustainable development (The World Commission on Environment and Development, 1987). Among other issues, the report discusses population growth, urbanization, and various energy sources. The effort to efficiently electrify roadways is an important component of ongoing sustainable development.

While discussing EVs, Chen and Kringos state, “In recent years, no significant improvements have been found for the available energy storage technologies. Recharging opportunities away from home have thus become a critical concern in order to encourage the widespread adoption for the use of EVs” (Chen & Kringos, 2015). Several different solutions are being developed to address this concern. There are two main methods to charge EVs: conductive and contactless. The conductive method requires a physical connection between the EV and the energy source.

The conductive method of electrifying road transportation started in the late 19th century. The original prototype of the trolleybus, a form of electrically powered public transportation, was presented in Berlin by Dr. Ernst Werner von Siemens in 1882 (Blocher). Throughout the 20th century, the trolleybus has seen development and successful operation, but has since declined from popular use. Its drawbacks are tied to its reliance on fixed overhead power lines. The power lines are expensive, tie the trolleybuses to fixed routes, and introduce additional maintenance and safety issues. A solution to improve their flexibility was found in the transfer of the physical connection between the vehicle and the power source from the overhead lines to the road surface. This connection can now be made from electric power rails located in the slot of a conduit below the roadway (Berman, 1978).

Modern conductive charging is commonly used with EVs in the form of plug-in charging stations at parking lots, garages, and stations. Its main deficiencies are related to the spatial distribution of charging stations and the lengthy and inconvenient amount of time required to fully charge an EV. To remove these hindrances, many advances are being made with respect to the contactless charging method. The contactless method encompasses any form of the use of a wireless power transmission (WPT) system to charge an EV.

There are currently six main types of WPT technologies being developed for EVs: inductive power transfer (IPT), capacitive power transfer, permanent magnet coupling transfer, resonant inductive power transfer, on-line inductive power transfer, and resonant antennae power transfer (Chen & Kringos, 2015). Of these alternatives, IPT technology has shown the best performance with respect to efficiency and received the most attention. With IPT, the energy from the power source is transferred to the receiving battery magnetically (Jain & Kumar, 2018). This principle is displayed in Figure 2.1.

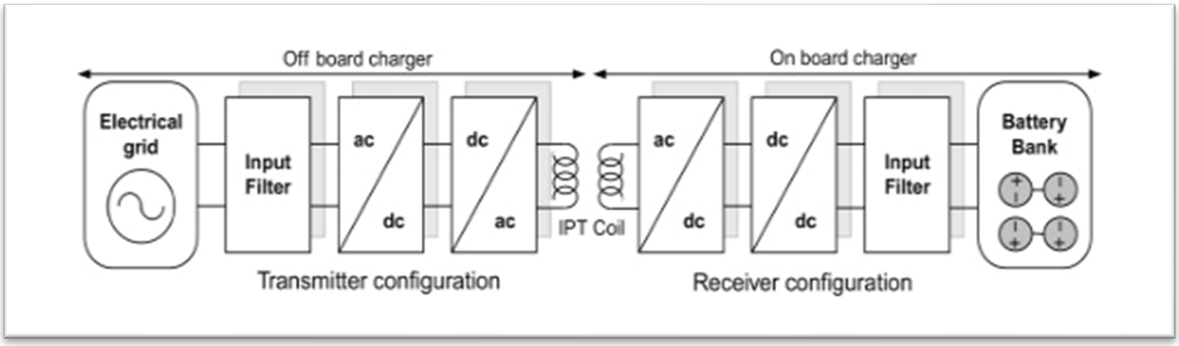

Figure 2.1 Diagram of IPT Technology

A typical IPTS used to charge EVs consists of an on-board device installed near the bottom of the vehicle's chassis and an off-board power delivery device embedded near the surface of the roadway. To enhance the efficiency of the IPTS, a magnetic material such as ferrite can be placed on the opposite side of the delivery device from the on-board receiver. Its purpose is to direct the magnetic flux and improve the coupling between the delivery device and the on-board receiver. Although IPT technology is still being refined to charge EVs, it has been in use for decades. Its applications include factory automation, lighting, instrumentation and electronic systems, biomedical implants, and security systems (Covic & Boys, 2013).

The application of IPT technology began in the industrial sphere and has recently shifted to meet the challenge of powering EVs under both stationary and dynamic conditions. Perhaps the first significant attempt to inductively power an EV was made by Hutin and Le-Blanc in 1894. They proposed a method and apparatus to power an EV using an approximately 3-kHz ac generator (Hutin & Leblanc, 1894). Although the work was abandoned in 1974, Otto proposed a system to inductively charge a moving vehicle in 1972 (Covic & Boys, 2013).

Otto's work was important because it established that power could be inductively coupled to a moving body. Throughout the 1980s, the Partner for Advanced Transit and Highways project developed an IPTS to charge a moving bus with a variable air gap, which is the space between the delivery device and the on-board receiver (PATH, 1994). In 1991, Boys and Green at the University of Auckland produced an IPTS potentially suitable for material handling and other applications (Boys & Green, 1991). Their work became the cornerstone of much of the work in the IPTS realm over the past 30 years because it was the first system where the individual components could be identified and separately improved.

There are several ongoing organizations and projects that are currently investigating the integration of embedded IPTS into roadways, e.g., the Flanders' DRIVE project in Belgium, the Slide-in Electric Road System-Inductive project in Sweden, the KAIST OLEV project in South Korea, and the ASPIRE program through the NSF Research Engineering Center. Unfortunately, the information regarding the structural aspects of roadways with embedded IPTS is still limited in all of these projects (Chen & Kringos, 2015). This signifies an urgent need to investigate the integration of IPTS in realistic roadway structures to enable dynamic EV charging. In their article, Chen & Kringos summarize the structural challenges included with embedding IPTS.

"To build an eRoad (electrified roadway) using IPT technology, facilities such as transmitters (coils, ferrite cores) and other controlling and ICT sensors need to be integrated into the road pavement. It is of paramount importance that this integration does not influence the performance of the individual components. Covic & Boys (2013) pointed out that the problem areas to be solved for IPT charging solution are the development of appropriate roadway infrastructure. The existing technology requires that fragile ferrite materials have to be integrated into the road pavement in such a way to give a long service life in a very hostile environment. In fact, not only the fragile IPT facilities need to be protected, the protection of the road's structural performance itself is similarly essential. If an eRoad is damaged during its designed service lifetime, the IPT systems will be prevented from functioning properly, leaving the eRoad in an overall state of malfunction for charging EVs or even supporting the mobility of "normal" traffic." (Chen & Kringos, 2015)

2.1.2 Alternatives to Metallic Reinforcement

Two of the most prevalent and researched alternatives to metallic reinforcement in concrete specimens are glass fiber reinforced polymer (GFRP) reinforcement and fiber reinforced concrete (FRC). There are many options for different fiber types that can be used. Due to the abundance of research for both reinforcement alternatives, each will have their own section in this literature review.

Hadi and Zhao tested three different types of meshes as confinement for high strength concrete columns. The three different types of meshes were fiberglass fly mesh, aluminum fly mesh, and steel wire mesh (Hadi & Zhao, 2011). In addition to the column specimens, mini-beam specimens were also created and tested. The mini-beams had the same alternative materials placed as flexural reinforcement. Their experimental results are summarized in Table 2.1.

Table 2.1 Hadi and Zhao; Experimental Results

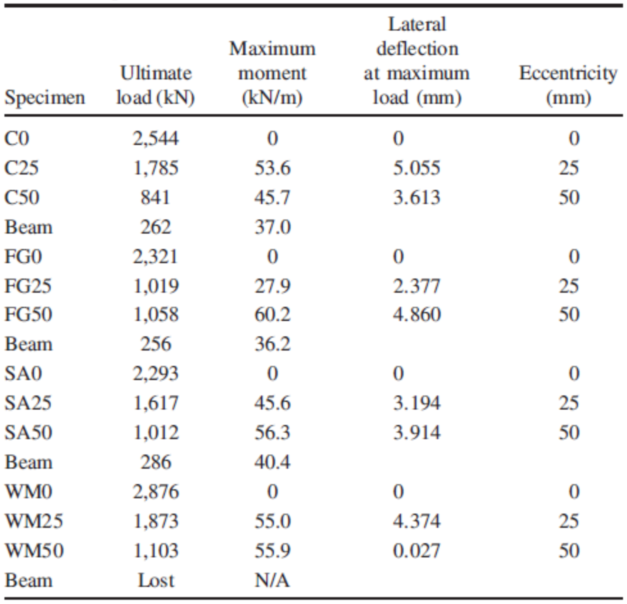

Specimen	Ultimate load (kN)	Maximum moment (kN/m)	Lateral deflection at maximum load (mm)	Eccentricity (mm)
C0	2,544	0	0	0
C25	1,785	53.6	5.055	25
C50	841	45.7	3.613	50
Beam	262	37.0		
FG0	2,321	0	0	0
FG25	1,019	27.9	2.377	25
FG50	1,058	60.2	4.860	50
Beam	256	36.2		
SA0	2,293	0	0	0
SA25	1,617	45.6	3.194	25
SA50	1,012	56.3	3.914	50
Beam	286	40.4		
WM0	2,876	0	0	0
WM25	1,873	55.0	4.374	25
WM50	1,103	55.9	0.027	50
Beam	Lost	N/A		

The results of this study indicate the fiberglass fly mesh increased the load-carrying capacity of the columns when subjected to eccentric loading. The steel wire mesh was the only alternative that significantly increased the load-carrying capacity of the columns when subjected to concentric loading. Both the fiberglass mesh and the aluminum mesh increased the ductility performance of the columns with similar values. Among the beam specimens, the aluminum fly mesh provided the highest load capacity. Similar to the columns, the aluminum fly mesh and the fiberglass fly mesh both improved the ductility of the beams by similar values. After a cost analysis, it was determined that the fiberglass mesh is the most economical material for ductility improvements (Hadi & Zhao, 2011).

A separate study was conducted to test the effectiveness of alkali-resistant (AR) glass fiber meshes and polypropylene fiber meshes as flexural reinforcement of concrete (Mu et al., 2002). Meshes were chosen because they are effective in bridging cracks in the concrete matrix, which is an important factor for the durability of the material. Mini-beam specimens were constructed for each alternative and evaluated using a three-point bending test. Mu et al. found the AR glass fiber mesh to be much more efficient as reinforcement than the polypropylene mesh due to its higher tensile strength and elastic modulus, but with two major drawbacks. The AR glass fiber mesh is 30 times as expensive by volume, and long-term weathering tests revealed the AR glass fibers might exhibit a loss of tensile strength and ductility with aging (Mu et al., 2002).For these reasons, the researchers investigated a method to improve the performance of the polypropylene fiber mesh by enhancing its bond properties. By adding a polymerization of latex during the hydration process, the bond between the mesh and the cementitious matrix was improved. The flexural behavior of the polypropylene fiber mesh-reinforced samples improved, and the cracking moment was found to be higher than that of the glass mesh-reinforced samples. A possible explanation for the improvements is that the latex increases the fluidity of the fresh concrete; thus, the cement matrix becomes denser during vibration and improves the bond to the mesh (Mu et al., 2002).

Geosynthetic reinforcement is another alternative to metallic reinforcement that has been investigated by many researchers. Although geosynthetic reinforcement is traditionally used to reinforce earthen structures such as embankments, shallow foundations, and beneath pavements, its economic advantages and resistance to corrosion make it attractive as concrete reinforcement. There are two categories of geosynthetic reinforcement that have been widely studied: geotextile and geogrid. Geotextiles are fine woven and resemble a fabric, while geogrids consist of parallel arrangements of connected ribs with openings large enough to allow surrounding materials to pass through. It is a general consensus that geogrids perform better as concrete reinforcing than geotextiles (RajeshKumar et al., 2021).

Studies have shown that geosynthetics can improve the load-carrying capacity, ductility, flexural strength, and energy-dissipation capacity compared with unreinforced concrete; however, El-Hanafy et al. do not recommend them as a replacement to steel reinforcement (El-Hanafy et al., 2022). See Figure 2.2 below for a direct comparison of the different slabs constructed and tested by El-Hafany et al.

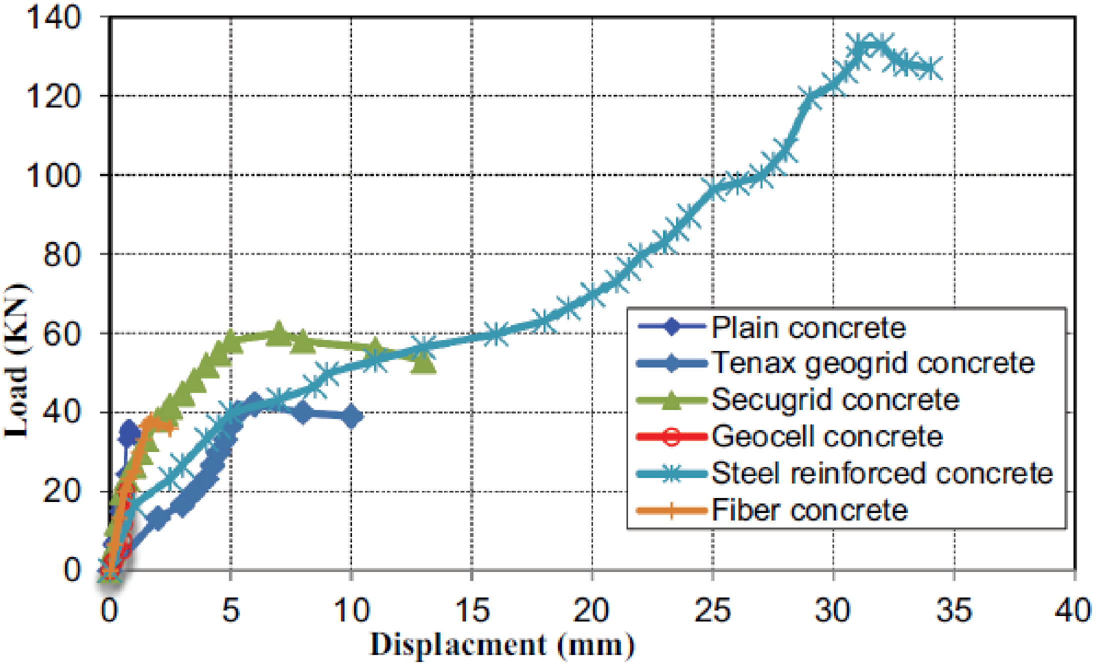

Figure 2.2 Load-Deflection for PC, RC, Fiber Concrete, and Geogrid Slabs (El-Hafany et al., 2022)

On the other hand, a separate study found that geogrid reinforced slabs improved the load-carrying capacity, ductility, and energy absorption as compared with a steel-reinforced slab by 25, 6.5, and 23%, respectively (RajeshKumar et al., 2021). This study also highlighted the inability of geotextiles to adequately bond with the concrete specimens, which is why the geotextiles perform worse than the geogrids. Despite the different conclusions reached by El-Hafany et al. and RajeshKumar et al., both studies agree that geogrid reinforcing allows for significant deformation after the initial cracking and before the ultimate failure.

After the initial cracking, it was found that the specimens with geogrid reinforcing experienced secondary cracking before failure (El-Hafany et al., 2022). In addition to the secondary cracking, these specimens returned to their original position and their cracks closed when unloaded. After reloading, the same load capacity was once again obtained (RajeshKumar et al., 2021). In comparison with unreinforced concrete specimens, this ductile behavior can easily be attributed to the elastic nature of geosynthetic reinforcing. Due to their high modulus of elasticity, geosynthetics require a significant amount of deformation before their tensile strength is completely developed.

It has also been shown that geosynthetics can successfully be used to increase the shear capacity of concrete beams. In their study, Majumder and Saha used geotextiles and geogrids to externally and internally reinforce concrete beams that were otherwise deficient in shear capacity. The geogrids once again performed better than the geotextiles, and they converted the failure mechanism in their specimens from shear to flexural. Although not suggested as a replacement for steel reinforcing, this study found geosynthetic reinforcing provides a remarkable enhancement in load-carrying capacity, energy dissipation, ductility, and post-yielding behavior compared with unreinforced concrete specimens (Majumder & Saha, 2021).

2.1.3 Preceding Research

There have been several recent research projects at Utah State University to investigate GFRP reinforcement and IPTS embedded in concrete pavement slabs. This project builds upon the findings and procedures established by the preceding projects. A brief summary of the research program and conclusions for each preceding project will be presented.

2.1.3.a Wireless Power Transfer Roadway Integration (Gardner, 2017)

Gardner's research can be divided into two main sections. The first section investigated the various wireless power transfer integration techniques and testing methods. The second section focused on the performance of a direct embedment approach as the integration technique. The embedment process involved testing the interaction of individual components of the IPTS with concrete, testing a full-scale concrete pavement slab with an embedded IPTS, and optimizing the electrical performance of multiple embedded IPTS. Through his research, Gardner concluded:

- A minimum wire coating thickness of 0.029 inches essentially eliminated the electrical performance losses associated with directly embedding the IPTS in concrete.
- An IPTS with an aluminum shielding plate between the system and the IPTS reduces the fatigue strength of the structure by as much as 48%.
- Without the aluminum shielding plate, the IPTS reduced the concrete pavement slabs fatigue strength by approximately 30%. The shielding plate was determined to be unnecessary and removed from the final design.
- Concrete microcracking, which accompanies high cycle fatigue scenarios, had little to no effect on the measured electrical performance of an IPTS (inductance and resistance).

A full-scale concrete pavement slab with an embedded IPTS was the culmination of Gardner's research. It was placed in the test track at the Electric Vehicle and Roadway (EVR) facility at Utah State University to be monitored in an in-situ application. Gardner expected his findings to be implemented in the electrical and structural design of future iterations of concrete pavement slabs with embedded IPTS (Gardner, 2017).

2.1.3.b Experimental Static and Cyclic Behavior of Hybrid Non-Metallic Bridge Decks Reinforced with Discrete GFRP Rebar and GFRP Macrofiber (McRory, 2020)

The purpose of this research project was to find a cost-effective solution to non-corrosive bridge deck reinforcement to create more sustainable bridge infrastructure. McRory investigated alternatives, including control panels with traditional steel rebar, panels with only GFRP rebar, and hybrid reinforced concrete (HRC) panels with both GFRP rebar and alkali-resistant fiberglass composite macrofibers. Full scale bridge deck models were constructed and tested under static and fatigue loading conditions.

The static load consisted of an incrementally increased load until failure was reached. The fatigue loading was applied at a frequency of 4 Hz over 1 million cycles for the first set and 2 million cycles for the second set. After the fatigue loading, McRory performed a static test on the decks to compare pre-fatigue and post-fatigue behavior. Based on the testing results, McRory made the following conclusions:

- In static flexure, the HRC decks deflect 29% more than the GFRP decks and 119% more than the steel decks for both pre-fatigue and post-fatigue.

- The steel decks demonstrated the most energy absorption after failure, and the HRC decks showed some post-peak ductility. The post-peak capacity of the GFRP decks is minimal due to the linearly elastic behavior of the GFRP until sudden failure.
- Some bond loss after fatiguing was shown in the GFRP decks, but the bond loss was not seen in the HRC or the steel decks.
- The fatigue loading did not adversely affect the static flexural behavior of any of the alternatives.
- All bridge decks, except for the 1-million cycle GFRP deck, were acceptable per the live load deflection criteria established by the American Association of Highway and Transportation Officials (AASHTO). The deck that failed exceeded the limitations by 1%.
- The HRC and GFRP decks' live load deflection values were similar. The steel deck outperformed both other alternatives with respect to live load deflection.
- All the alternatives performed exceptionally well with regard to the peak crack width.

McRory found the HRC deck panels to be the most viable solution to produce a non-corrosive bridge deck reinforcing system. By comparing the HRC decks to the GFRP decks after fatigue loading, we can see that the bond behavior of the GFRP rebar is enhanced by the alkali-resistant fiberglass composite macrofibers. McRory suggested future research to better understand the shared crack bridging behavior of the discrete GFRP reinforcement and the discontinuous, randomly oriented fibers (McRory, 2020).

2.1.3.c Long-Term Feasibility of Inductive Power Transfer Systems Embedded in Concrete Pavement Panels (Raine, 2022)

In this experiment, Raine tested two concrete pavement slabs with functioning embedded IPTS. One slab was reinforced with steel rebar and the other was reinforced with GFRP rebar. The testing regimen subjected both slabs to fatigue and static loading. The fatigue loading was performed at 2 Hz over 320,000 cycles at three different force loadings. During the fatigue loading, the capabilities of the embedded IPTS were monitored to ensure it remained functional. The static load was increased at a constant rate until catastrophic failure was reached. Raine made the following conclusions based on the test results:

- The electronics of the IPTS embedded in each slab functioned properly during the fatigue cycling. Even after initial failure, both IPTS were still functional.
- Cracking occurred early in the fatigue cycling for both slabs. Adjustments to the structural design of the slabs will be required to enable longer lifespans.
- The aggregate in both slabs was well distributed with no settlement. This proves precasting is a viable production method for slabs with embedded IPTS.

The conclusions of Raine's research led to two main statements. First, embedding IPTS in concrete pavement slabs is a viable solution to increase the useability of EVs. The IPTS technology proved to be capable of surviving adverse loadings and conditions. Second, the GFRP reinforcement is a viable alternative to steel reinforcement in concrete pavement panels. Raine suggested further testing of GFRP reinforced concrete pavement slabs with embedded IPTS to better understand the life cycle of the IPTS (Raine, 2022).

2.2 Durability of Reinforced Concrete

2.2.1 Surface Cracking in Pavements

Surface cracking in both rigid and flexible pavements has long been considered a main cause of deterioration in roadway pavements. The surface cracks allow water to penetrate the pavement, which can widen the cracks during freeze/thaw cycles. Water that has penetrated through the pavement can also reduce the strength of sub-base layers and result in larger cracks and potholes. Surface cracks also affect the aggregate interlock, load transfer efficiency, and tensile stresses in concrete specimens (Zhang et al., 2023). Although the exact location of periodic cracks in pavement structures depends on the configuration of the structure, the periodic cracks always occur in the bending zone of the pavement (Xu et al., 2011).

In their research, Xu et al. found the first stage of surface cracking in pavements consists of initial cracks near the support points of the surface layer when the tensile stress reaches the tensile strength of the surface layer material. New cracks then form and infill at the midpoints between the initial cracks. The crack spacing reduces by half during this infilling process. Xu et al. explain the infilling cracks always form at the midpoint between adjacent cracks because the horizontal stress in the surface layer of the pavement decreases as the distance from the top of the surface layer increases. At a given distance from the top of the surface layer, the horizontal stress reaches a peak value at the midpoint between adjacent cracks. These same horizontal stresses acting parallel to the adjacent cracks change from tensile to compressive when the crack spacing decreases to a certain value. At this point, no more cracks are formed (Xu et al., 2011).

Xu et al. also investigated how different aspects of the pavement design affect the formation and propagation of surface cracks. As the thickness of the surface layer increases, the crack spacing also increases at a ratio of approximately 3:1. Increasing the base layer thickness will also increase the crack spacing, although not as drastically. The crack spacing can also be increased slightly by increasing the elastic modulus of the base layer. Contrarily, increasing the elastic modulus of the surface layer will inversely decrease the crack spacing. Finally, a higher tensile strength of the surface layer will lead to increased crack spacing (Xu et al., 2011).

Other factors associated with concrete pavement structures also affect surface cracking properties. These factors include concrete drying shrinkage, drying temperature, slab-base friction, and bond slippage between the concrete and reinforcement (Xin et al., 1992). Zhang et al. created a one-dimensional analytical model to determine that the bond stiffness coefficient, elastic modulus of the reinforcement, concrete drying shrinkage, and base layer friction coefficient had the greatest impact on crack spacing and crack width (Zhang et al., 2023).

In a separate study, Wang et al. modified the ACI formula to calculate crack widths in GFRP reinforced concrete to predict crack widths more accurately in concrete beams with steel-carbon fiber composite rebar. The modified formula included the effects of the elastic modulus before and after yielding of the reinforcement and the reduced bond strength between the concrete and the reinforcement (Wang et al., 2022). As illustrated in Figure 2.3, their test results showed beams with steel reinforcement had the smallest crack widths, beams with carbon fiber reinforced polymer (CFRP) rebar had the largest crack widths, and beams with hybrid steel and carbon fiber reinforcement had crack widths between the other two alternatives.

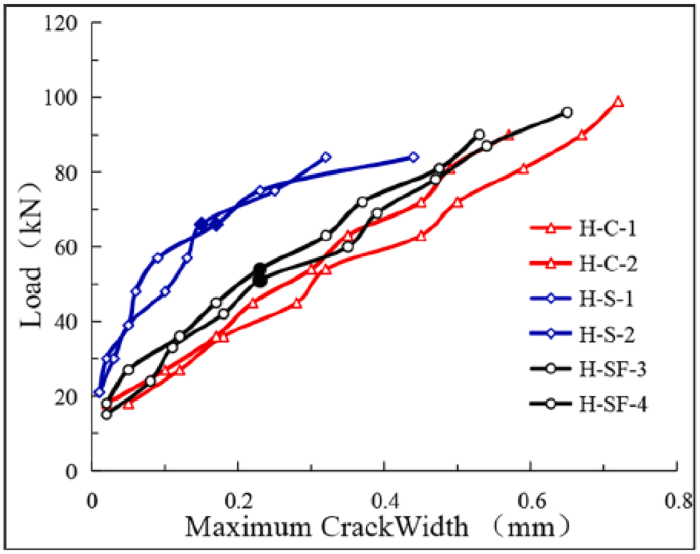

Figure 2.3 Maximum Crack Widths for Different Reinforcing Alternatives (Wang et al., 2022)

2.2.2 Concrete Spalling

Concrete spalling refers to the process of chipping or flaking of the concrete surface. Spalling can be caused by exposure to weather conditions such as freeze-thaw cycles, moisture, chemicals, or extreme heat. It can also be caused by structural issues, such as the corrosion of reinforcing steel or excessive load on the concrete. Spalling affects both the appearance and the structural integrity of the concrete. It can lead to the formation of cracks, which can further weaken the structure and allow water to penetrate deeper into the concrete, causing further damage.

Perhaps the most common cause of concrete spalling is the corrosion of reinforcing steel. The reaction products of the corrosion process are accompanied by a volume expansion, which is the reason for the spalling (Angst et al., 2012). Angst et al. also found there are two corrosion mechanisms that affect the surrounding concrete differently. Chloride contamination results in localized corrosion, which is concentrated in one area as shown in Figure 2.4. The other mechanism, carbonation, results in uniform corrosion of the steel reinforcement. Typically, concrete spalling is strongly delayed with localized corrosion, if it even occurs. However, the reinforcement in the corner of a concrete component will be attacked by chloride penetration from two directions at the same time. As a result, the initiation of the corrosion and concrete spalling of the corner will be advanced (Chen, Airong, et al., 2016). Generally, carbonation and uniform corrosion are the main concerns for volume expansion leading to concrete spalling.

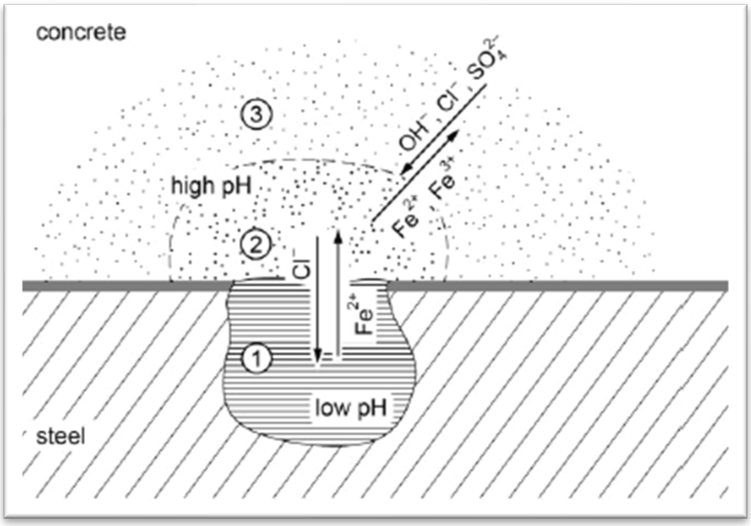

Figure 2.4 Schematic Sketch of Localized Corrosion (Angst et al., 2012)

Bae and Oguzhan studied early cover spalling in high-strength concrete columns. An important finding from their research is that the compressive strength of the concrete is not correlated with the strain at which concrete spalling occurred (Bae & Oguzhan, 2003). A separate study found that steel fibers randomly oriented in the concrete mix are one way to prevent the early spalling of concrete cover (Foster, 2001). It is assumed other fiber types with a similar tensile strength and elastic modulus will perform in a similar manner.

There are three types of concrete spalling that can occur due to extreme heat: thermo-hygral, thermo-mechanical, and thermo-chemical (Liu et al., 2018). Thermo-hygral spalling is induced by moisture clogging and pore pressure buildup inside heated concrete between the temperatures of 220°C and 320°C. Temperatures between 430°C and 660°C can cause restraint-induced thermal stresses resulting in thermo-mechanical spalling. Thermo-chemical spalling is related to the decomposition of hydrated products and rehydration of calcium oxide; it typically occurs at temperatures greater than or equal to 700°C (Liu et al., 2018).

The most widely used method to prevent concrete spalling due to extreme heat is the addition of polypropylene (PP) fibers. PP fibers begin to melt at approximately 150°C and are completely melted around 175°C. When the PP fibers melt, they leave behind a porous network of micro channels that release the pore pressure created during the thermo-hygral spalling process, thus enhancing spalling resistance. The addition of PP fibers alone is moderately effective, but Li et al. found steel fibers and PP fibers together produce a synergistic effect. The empty micro channels created by melted PP fibers are further connected by microcracks generated from the thermal expansion and incompatibility of the two different fiber types. The enhanced connectivity significantly increases the permeability and spalling resistance of concrete (Li et al., 2019).

2.3 Fiber Reinforced Concrete

2.3.1 Introduction to FRC

An abundant source of information regarding fiber reinforced concrete (FRC) can be found in the *Guide to Design with Fiber-Reinforced Concrete* reported by ACI Committee 544 in 2018. Unlike reinforcing bars, fibers are randomly and uniformly distributed throughout a concrete specimen. The average distance between fibers is much smaller than the typical spacing for reinforcing bars. Because of this, the tensile stresses in the concrete are carried by the fibers at very early stages of the cracking process; therefore, crack development patterns change relative to conventionally reinforced concrete (ACI Committee 544, 2018). The addition of fibers can also change the post-crack response of concrete from brittle to ductile under compression, tensile, flexure, and impact loads (Bonakdar et al., 2005).

Before cracking, FRC specimens can be assumed to be homogeneous and isotropic. After cracking, these assumptions no longer hold. Fibers bridge the cracks and begin to carry tensile stresses as soon as the cracks form. This results in the FRC having a tensile load-carrying capacity in a cracked state. This load-carrying capacity is usually referred to as residual strength. Keeping all other variables constant, higher fiber contents will provide higher values of residual strength as long as the concrete mixture can properly accommodate the fibers (ACI Committee 544, 2018).

The stages of FRC failure are schematically shown in Figure 2.5. First, cracks form in the cement matrix followed by some amount of debonding and sliding between the matrix and the fibers. Then the bonded fibers bridge the gap and carry the tensile stresses. This is associated with frictional sliding and deformation of the fibers. Eventually, ultimate failure of the fibers will manifest itself in one of two forms: fiber pullout or fiber rupture. Structural failure of the fibers can be considered as the final stage when the fibers are no longer able to resist tensile stresses and may occur before pullout or rupture. Different fiber types and geometries may not exhibit all the described stages of FRC failure.

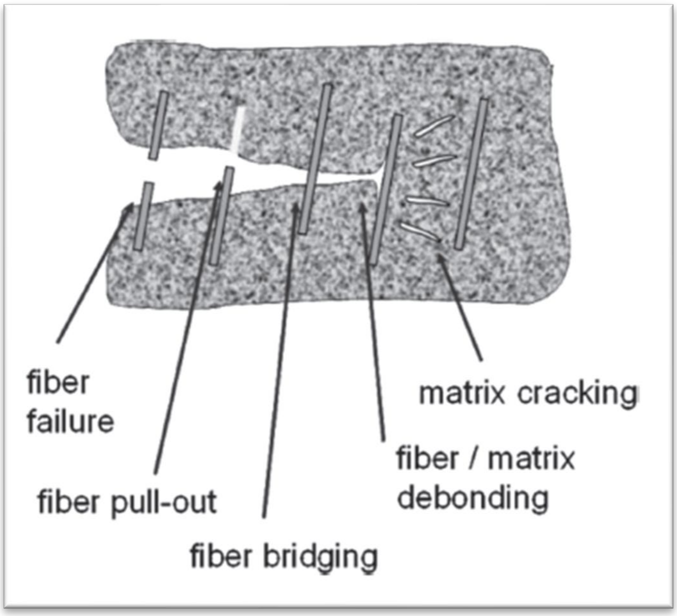

Figure 2.5 Schematic Failure of FRC (ACI Committee 544, 2018)

The presence of fibers influences the flexural response of concrete to a much greater degree than the compressive response. Two different flexural strength values are commonly reported: the first-crack strength and the ultimate strength, or modulus of rupture. The first-crack strength corresponds with when the concrete matrix cracks and the load-deformation curve is no longer linear. Because fibers do not engage until after the concrete matrix is cracked, the presence of fibers in FRC has a negligible effect on the first-crack strength. After cracking, the presence of fibers allows a concrete specimen to absorb much more energy before the ultimate strength is reached. The total energy absorbed before ultimate failure of a specimen is referred to as toughness and is an important characteristic of FRC (ACI Committee 544, 2018).

In recent years, the measure of residual strength has replaced the toughness index for FRC. Residual strength for FRC is defined as the strength of the concrete after it has cracked. The flexural residual strength of FRC in a cracked section is typically between 2.5 and 3 times its tensile residual strength (Vandewalle, 2003). With increased residual strength, FRC also provides increased fracture energy. Originally, fracture energy was quantified as the energy required to begin initial cracking, but Hillerborg's research suggested the total fracture energy parameter be quantified as the energy to propagate the cracks to ultimate failure (Hillerborg, 1985). Similar to flexural response, fibers have been shown to improve the shear response of FRC as well. Fibers provide continuity for tensile stresses across diagonal shear cracks, which reduces the diagonal crack width and spacing. In turn, the aggregate interlock is improved (Talboys & Lubell, 2014). Fiber reinforcement could lead to an omission or at least reduction of stirrups required for shear reinforcement. Past research has proven that stirrups and fibers can be used effectively in combination (Altoubat et al., 2019).

One of the main instances where fibers are employed as the sole method of reinforcement in concrete is slabs-on-ground. This includes residential floors, commercial floors, roads, and pavements. The three-dimensional nature of fiber reinforcement improves the crack resistance of concrete, specifically near the surface, which results in a longer service life for slabs and pavements. Smaller dosages of fibers in slabs are used to control cracks from drying shrinkage and thermal stresses, while larger dosages are used to provide additional bending moment capacity and residual strength after cracking. For these same reasons, FRC has also been used in topping slab applications such as concrete bridge decks and parking garages. In addition to crack resistance, fibers have been shown to improve the durability of bridge decks, slabs, and overlays exposed to water and freeze-thaw cycles (Balaguru & Ramakrishnan, 1986).

2.3.2 Different Types of Fibers in FRC

The ACI Committee 544 classifies fibers used in FRC based on their material types, geometries, and sizes. The length of fibers typically ranges from 1/8 to 2-1/2 inches. The longer fiber lengths are correlated with a decrease in workability of the concrete mix and are more likely to segregate within the mixture (Tabatabaei et al., 2013). A subclassification of macro or micro is often used with the separating limit being a fiber diameter of 0.012 in. The fiber material categories outlined in Committee 544's 2018 report are steel, glass, synthetic, and natural. However, the design guidelines in the document are limited to steel and synthetic macrofibers only (ACI Committee 544, 2018).

Steel fibers used in FRC are generally short enough to allow for random dispersion with common mixing procedures. They are produced in many different geometries, including flat, rectangular, cylindrical, and combinations of these. Steel fibers can also be found with additional anchorage mechanisms such as dimples, twists, and end hooks. The bond between the cement matrix and the steel fibers is enhanced by the anchorage mechanisms, increased surface area, increased surface roughness, or any combination of these. An important performance characteristic of steel fibers is their aspect ratio, i.e., the ratio of the length to the diameter. Typically, the performance of steel fiber reinforcing increases as the fiber aspect ratio increases. The required dosage of steel fibers in an FRC mix depends on the specific application and required performance of the FRC (ACI Committee 544, 2018).

Synthetic fibers, as defined by ACI Committee 544, are made from polyolefin materials, which typically include polypropylene and polyethylene. These fibers are available in various forms such as rope or tape filaments, and they may be embossed or twisted. The bond between synthetic fibers and the concrete is primarily achieved through friction, but some uses of chemical bonding have been reported. Synthetic macrofibers and microfibers serve two distinct purposes. Microfibers are generally used to control cracks resulting from plastic and drying shrinkage. Their contribution to the mechanical properties of hardened concrete is ignored. On the other hand, macrofibers are used to enhance the mechanical properties of hardened concrete. It is common to use a blend of synthetic macrofibers and microfibers to achieve both purposes (ACI Committee 544, 2018).

There are many different types of synthetic fibers, and the 1996 version of ACI Committee 544's report provides details for some of the most popular types. Aramid is a manufactured polymeric material. Kevlar is a trademarked brand name for perhaps the most common aramid fiber. The mechanical properties of aramid fibers are very attractive, but their high cost has been a limitation to their commercial use as concrete reinforcing. They are five times as strong as steel fibers per unit weight and are unaffected by temperatures up to 160°C (ACI Committee 544, 1992). Nguyen et al. experimented with different forms and lengths of aramid fibers and found the optimum length to be 1.5 inches (Nguyen et al., 2016). FRC using aramid fibers has been proven to increase the ultimate tensile strength, modulus of elasticity, flexural performance, and toughness of concrete specimens (Nanni, 1992).

Carbon fibers were initially developed for applications within the aerospace industry. Their high strength to weight relationship and high stiffness properties are very desirable. Like aramid fibers, carbon fibers are expensive compared with most other synthetic fibers. For this reason, their widespread use in commercial development has been limited. Carbon fibers can be manufactured as either high modulus

(HM) or high-tensile strength (HT) fibers. The difference depends on the material source and the manufacturing process. The tensile strength of HT carbon fibers is approximately 130% that of aramid fibers. It has been shown that less expensive carbon fibers can be made from petroleum and coal pitch, but their mechanical properties are far inferior to traditional carbon fibers (ACI Committee 544, 1992). Fatigue testing of FRC using carbon fibers indicates that the concrete specimen initially decreased in strength due to the dynamic loading and then leveled off at some limiting strength. The limiting strength was much greater than the cracking strength of the matrix (Biggs & Bowen, 1974). The same report indicated carbon fibers improve the impact strength, fracture toughness, and dimensional stability of FRC. In blast testing performed on concrete panels, it was found the panels reinforced with carbon fibers outperformed the plain concrete panels by a factor of nearly 10 in terms of the amount of material lost during the blast (Tabatabaei et al., 2013).

There are many additional types of synthetic fibers, such as nylon and polyester. However, the tensile strength of these fibers is considerably less than the tensile strength of aramid and carbon fibers. The fiber types with lower tensile strengths are not good alternatives to use as reinforcing when the desired effect is to improve the mechanical properties of the FRC.

2.3.3 Fatigue of FRC

Researchers began to examine the flexural fatigue response of FRC in the early 1970s. In 1972, Batson et al. tested differing lengths of steel fibers in concrete mini-beams that measured 4 x 6 x 102 inches. All the beams were subjected to 2 million cycles of loading at approximately 80% of their static flexural strength. The beams that did not fail during fatigue cycling had a higher ultimate flexural strength compared with the pre-fatigue beams (Batson et al., 1972). The fibers in the beams failed by pulling out rather than rupturing, which suggests the bond between the fibers and the concrete was the limiting factor. A few years later, a similar study confirmed those same results. O'Neil tested 6 x 6 x 36 in. beams with steel fiber reinforcement over 2 million cycles, and the post-fatigue beams had a greater ultimate flexural strength than the pre-fatigue specimens (O'Neil, 1978).

An experiment in 1989 tested FRC mini-beams in fatigue and included three different fiber types: polypropylene, steel, and hooked-end steel fibers. The mini-beams were initially subjected to 2 million cycles, and the surviving beams were subjected to 2 million more cycles. Once again, the post-fatigue specimens exhibited higher ultimate flexural strength than their pre-fatigue counterparts, even after 4 million cycles. The hooked-end steel fibers showed the best performance with regards to fatigue strength; the endurance limit and fatigue strength both increased with increasing fiber content for all three fiber types (Ramakrishnan et al., 1989).

Johnston et al. also performed fatigue testing on FRC specimens with varying fiber contents, fiber types, and fiber aspect ratios. Of all the tested variables, it was confirmed that the fiber content was the most critical variable regarding the flexural behavior of the beams (Johnston et al., 1991). A few years later, an additional variable was introduced into FRC fatigue testing by adding silica fume to the concrete mix. Under fatigue loading, it was found the silica fume improved the bond between the fibers and the concrete, resulting in improved crack control and mitigation (Wei et al., 1996).

In a comparison of deflection, it was found the maximum deflection at failure in fatigue of FRC specimens was very close to the same amount of deflection on the static testing load-deflection curve at the corresponding load. It can be deduced that fatigue loading does not increase the deflection experienced by FRC specimens (Zhang et al., 1998). In an overview of the published fatigue literature for plain concrete and FRC, Lee and Barr stated FRC appears to have an endurance limit of approximately 2 million cycles. The endurance limit represents the point at which a specimen experiences failure due to fatigue damage. Plain concrete exhibited no endurance limit. They also acknowledged many of the discrepancies in concrete fatigue literature and stated more research is needed to completely understand the fatigue behavior of FRC compared with plain concrete (Lee & Barr, 2004).

A fatigue experiment on three full-scale concrete deck slabs was performed in 2006 by Gopalaratnam et al. The control deck slab had epoxy coated steel reinforcing, the second slab had hybrid reinforcing consisting of GFRP bars and discrete polypropylene fibers, and the third slab had hybrid reinforcing with CFRP bars and discrete polypropylene fibers. All three slabs were subject to 1 million cycles of a 3 Hz sinusoidal loading with an upper limit of 20 kips and a lower limit of 10 kips. The stiffness degradation and overall fatigue performance of the hybrid slabs was similar to that of the control slab. The fibers in the hybrid slabs did decrease the width of the surface cracks that developed (Gopalaratnam et al., 2006).

2.4 GFRP Reinforcing

2.4.1 Introduction to GFRP Reinforcing

Composite materials made of fibers embedded in a polymeric resin, e.g., fiber reinforced polymers (FRP), have become an alternative to steel reinforcement for concrete structures. The development of FRP as reinforcement can be associated with the increased use of composites after World War II. Similar to other synthetic materials, the aerospace industry recognized its advantages as a high strength and lightweight material. The use of FRP quickly expanded to make common products such as golf clubs and fishing poles. However, it was not until the 1960s that FRP was seriously considered as reinforcement in concrete, and it took another decade before FRP bars were commercially available in the late 1970s (ACI Committee 440, 2015).

Glass fiber reinforced polymer (GFRP) reinforcing is one type of an FRP composite material. Perhaps three of its most useful properties are corrosion resistance, higher tensile strength, and higher failure strain compared with steel. The typical density of GFRP bars is between 77 and 131 lb/ft^3. For reference, the density of steel rebar is 493 lb/ft^3 (ACI Committee 440, 2015). The coefficient of thermal expansion for GFRP bars varies in the longitudinal and transverse directions depending on resin type and volume fraction of the glass fibers. The longitudinal coefficient is approximately half that of steel, and the transverse coefficient is approximately twice that of steel. In addition to the coefficient of thermal expansion, the volume content of fibers along with the rate of curing, manufacturing process, and quality control will affect nearly all the mechanical characteristics of GFRP bars (Wu, 1990).

Tests results have shown that GFRP rebars do not degrade, even in the presence of alkaline and corrosive environments (Kemp & Blowes, 2011). The high strain failure of GFRP may provide enough time to alert users before failure takes place, which is important to counteract the brittle behavior of GFRP. Its relationship between stress and strain is linearly elastic up to the point of failure, and its failure strain is found to be 20% higher than steel in reinforced concrete specimens (Jabbar & Saad, 2018).

GFRP, along with all types of FRP, should not be relied upon to resist compression. In general, the compressive strength of FRP bars increases as the tensile strength increases, but the compressive strength of GFRP bars has been reported as approximately 55% of the tensile strength (Mallick, 1988). Though GFRP should not be used as compressive reinforcement, it is acceptable for GFRP tensile reinforcement to experience compression due to changes in load patterns or moment reversals; however, the compressive strength of the GFRP bars should be neglected in these instances (ACI Committee 440, 2015). In addition to compression, FRP bars are relatively weak against shear stresses. This is because there are layers of unreinforced resin between fibers, and the shear strength is governed by the interlaminar strength of the relatively weak polymeric resin.

Jabbar and Saad tested concrete specimens reinforced with GFRP rebars in bending. The test variables were reinforcement ratio, surface finish, and rebar diameter. The results showed deflection was only affected by reinforcement ratio, while crack widths were affected by all three. They also found the GFRP rebar performed poorly in shear resistance due to its anisotropic nature. GFRP bars only have high tensile strength in the direction of the reinforcing fibers within the bars (Jabbar & Saad, 2016).

One experiment showed that an external sand coating on the rebar provided a better bond to the concrete than smooth rebar and helically grooved rebar (El-Nemr et al., 2013). Conversely, a separate study showed the bond strength of concrete increased from least to greatest in the order of sand coated, helically grooved, and ribbed bars (Erdem et al., 2015). It is important to note the bond strength of all FRP bars relies upon the transfer of forces at the interface between the bars and the concrete and also between individual fibers within the bars. Therefore, any environment that negatively affects the polymer resin or the resin interface are likely to decrease the bond strength of an FRP bar.

FRP reinforcing bars subjected to a constant load over a significant amount of time can suddenly fail. This phenomenon is known as creep rupture, and the time period to failure is called the endurance time. In general, GFRP bars have been found to be more susceptible to creep rupture than carbon and aramid FRP bars. Seki et al. investigated creep rupture in GFRP with a rectangular cross-section and found the retained tensile strength followed a linear relationship with logarithmic time, eventually reaching a value of 55% of the initial tensile strength at an extrapolated 50-year endurance time (Seki et al., 1997). Aqueous solutions with high pH values are also known to degrade the tensile strength and stiffness of GFRP over time. However, specific values of degradation vary tremendously according to different test methods (Porter et al., 1998).

2.4.2 Fatigue of GFRP Reinforcing

Mandell observed the fatigue effect in GFRP reinforcing is likely due to interactions between fibers rather than stress corrosion within individual fibers (Mandell, 1982). This suggests the polymeric resin is the governing factor in the fatigue strength of GFRP bars. Additionally, the presence of ribs, wraps, and other surface deformations to improve the bond behavior of GFRP bars have been shown to significantly reduce their fatigue performance (Katz, 1998). The deformations induce local stress concentrations in the polymer resin. Traditionally, direct fatigue testing of GFRP bars has been made complicated due to the difficulty of gripping the specimen without crushing the resin matrix in the grips. Demers reviewed fatigue tests of FRP specimens subjected to cyclic loading of 5 Hz or less and established a linear lower bound 95% confidence level, shown in Equation 2.1, for different stress ranges based on prior research (Demers, 1998).

$$\frac{S_{max}}{S_{min}} = -0.078 * logN + 0.790 \tag{2.1}$$

Where:

- S_{max} = Maximum tensile fatigue stress in fatigue load cycle
- S_{min} = Minimum tensile fatigue stress in fatigue load cycle
- N = Fatigue life measured in cycles

Kumar and GangaRao performed some of the first fatigue testing on bridge decks reinforced with GFRP rebar. Their full-scale experiment tested four different concrete deck slabs reinforced with GFRP bars under cyclic loading at a frequency of 1 Hz. The results showed the degradation of GFRP reinforced decks in the fatigue crack propagation zone compared well with the degradation of steel reinforced decks. Additionally, the GFRP decks had a linear stiffness degradation even after 2 million fatigue cycles; therefore, it was assumed that 2 million cycles represent 80% of the fatigue life of the GFRP reinforced decks (Kumar & GangaRao, 1998).

Klowak et al. subjected a deck with three separate segments to 25-ton fatigue loading for 1 million cycles. After the initial 1 million cycles, the fatigue load was increased to 60 tons for subsequent cycles until failure. The three different segments of deck consisted of the control steel reinforced segment, a carbon fiber reinforced polymer (CFRP) reinforced segment, and a GFRP segment. The FRP segments had external steel straps on the bottom of the segments. Of all three segments, the GFRP segment demonstrated the best fatigue performance (Klowak et al., 2006).

In a separate experiment, El-Ragaby et al. also concluded that GFRP reinforced concrete decks perform better in fatigue and have a longer fatigue life than traditional steel decks. They constructed a total of five full-scale bridge decks, four with GFRP reinforcement and one with steel reinforcement. Each deck was subjected to variable amplitude fatigue loads for 100,000 cycles at 2 Hz. If failure did not occur, the fatigue protocol was repeated with increased loads. Even after 4 million cycles, the GFRP deck did not fail. They concluded that the improved performance was due to the similar modulus of elasticity for GFRP and concrete (El-Ragaby et al., 2007). Similarly, Sivagamasundari and Kumaran performed a direct comparison of steel reinforced slabs and GFRP reinforced slabs subjected to fatigue loading. They found the damage accumulation in the steel slabs was greater than for the GFRP slabs, and they determined the GFRP decks reinforced with sand-coated GFRP bars experienced the highest stiffness and smallest residual deflection under cyclic loading (Sivagamasundari & Kumaran, 2008).

In 2010, Carvelli et al. researched the fatigue performance of four bridge decks designed with GFRP reinforcement per the Eurocode specification. Two hydraulic actuators were used to apply alternating pulsating loads to mimic a cyclic moving load. All slabs performed well according to the Eurocode serviceability requirements. One of the important findings from the research is that no debonding of the GFRP bars was seen in any of the slabs during the cyclic loading (Carvelli et al., 2010).

2.5 Fatigue Response

Schutz cited over 500 sources to create a comprehensive and in-depth review of the history of fatigue (Schutz, 1996). This document only attempts to discuss a few pertinent highlights from the research history of fatigue response. De Joly conducted the earliest reported study on the fatigue response of concrete in 1898. He found both the age of the specimen and the rate of cyclical loading to be major factors in the number of fatigue cycles to failure (Falk, 1904). A similar study agreed with De Joly's findings and proved concrete can fail at a reduced percentage of its ultimate capacity when subjected to repeated loadings. The study also showed that concrete specimens experience a degradation of stiffness under cyclic loading (Van Ornum, 1903).

Further research has shown that most of the permanent deformation due to fatigue loading occurs during the first cycles of the test. Following the initial stage of rapid permanent deformation, the total deformation will slowly increase until failure (Nordby, 1958). Nordby also observed that larger stress ranges during cyclic loading correlate to decreased upper limits of stress. For reinforced concrete beams designed to fail in flexure, the fatigue limit after 1 million cycles was found to be within 60% to 70% of the original static strength of the beams (Nordby, 1958).

In 1968, a review of preceding fatigue literature concluded that two characteristics are important to understand the mechanics of fatigue failure: changes in the stress-strain relationship and crack growth propagation. Fatigue loading creates bond failure between the aggregates and cement matrix, which results in cracks. These cracks then progress through the cement matrix until they are stopped by an aggregate. This process repeats itself until complete failure of the concrete specimen (Raithby & Whiffin, 1968). Raithby later observed that fatigue behavior of concrete imitates its flexural behavior while testing a large number of static and fatigue specimens. He suggested that concrete specimens with higher flexural capacities will have proportionally larger fatigue strengths, and he asserted this relationship can be extrapolated when trying to determine the fatigue strengths of different concrete mixes (Raithby, 1979).

Hsu determined any testing with a cycle count between 100,000 and 10 million cycles can be accepted as high cycle fatigue testing for pavements. This range corresponds to the expected number of cycles a pavement will be subjected to throughout its service life. The range depends largely on population density and will likely increase as population increases, but it is a good target for most research (Hsu, 1981). Around the same time, Sonoda and Horikawa performed a series of fatigue tests on 1/3 scale reinforced concrete decks with moving cyclic loading. They found the moving loads to be much more detrimental to the fatigue strength of the decks than a stationary cyclic load; grid-like cracking patterns resulted from the moving cyclic loads. Due to the two-way cracking, they concluded that transverse reinforcement is more important in the case of moving fatigue loads than stationary fatigue loads (Sonoda & Horikawa, 1982).

Most laboratory research is conducted on small-scale specimens. For ease of testing, flexural scenarios are often tested on beams instead of slabs. Roesler noted that the strength of concrete slabs is much greater than that of comparable beams; the concrete slabs have flexural capacities 1.3 to 3.5 times higher than the comparable beams (Roesler, 2006). Per Raithby's findings, it can be assumed the fatigue strengths of concrete slabs will also be significantly higher than those of their beam counterparts. From the full scale slabs that have been tested in fatigue conditions, Roesler found the development of equations to predict concrete fatigue strengths was governed by four main factors: size effect (specimen geometry, loading configuration, and boundary conditions), theoretical model for stress calculation (plate theory or layered elastic analysis), included bending stresses (temperature and moisture curling in addition to mechanical loading), and the method of counting stress repetitions (Roesler, 2006). Roesler used these findings to determine the fatigue life equation shown in Equation 2.2.

$$N_f = \left[\frac{2.689}{\left(\frac{\sigma}{MOR_{beam}}\right)}\right]^{21.79} \tag{2.2}$$

Where:

- N_f= number of fatigue cycles until failure
- σ = applied maximum stress level
- MOR_{beam} = modulus of rupture of the concrete

When analyzing fatigue response, the S-N curve, which is also called the Wöhler curve, is commonly used. The S-N curve for concrete represents the relationship between the applied maximum stress and the number of load applications, which may cause fatigue failure of the specimen (Hwan, 1986). The development of an S-N curve requires many specimens to be tested to failure at different stress ranges. A curve can then be fit to the set of data points, thereby creating the S-N curve.

2.6 Flexural Response

The flexural response of concrete is well defined in several codes, including the AASHTO *LRFD Bridge Design Specifications* (AASHTO, 2018a), and the ACI 318 *Building Code Requirements for Structural Concrete* (ACI 318, 2019). There are several common assumptions that are made when analyzing reinforced concrete in flexure:

- Plane sections remain plane after loading.
- The maximum usable strain at the extreme concrete compression fiber is 0.003.
- The tensile strength of concrete is neglected.
- A rectangular stress distribution acceptably approximates the compressive stresses.

Typically, an equivalent strip method is used for reinforced concrete in flexure. The concrete slab or deck is divided into strips parallel to its span, and the applied load is reduced by the width of the equivalent strips. AASHTO provides guidance to calculate the width of equivalent strips for different elements (AASHTO, 2018a). An applied load per foot of width is obtained, after which the flexure strength of the reinforced concrete is analyzed using Equations 2.3 through 2.5.

$$M_n = A_s * f_y * \left(d - \frac{a}{2}\right) \tag{2.3}$$

Where:

- M_n = nominal flexural resistance
- A_s = area of tension reinforcement
- f_y = yield stress of tension reinforcement
- d = distance from the extreme compression fiber to the centroid of tension reinforcement
- a = depth of equivalent stress block

$$a = \beta_1 * c \tag{2.4}$$

Where:

- β_1 = stress block factor
- c = distance from the extreme compression fiber to the neutral axis

$$c = \frac{A_s * f_y}{0.85 * f'_c * \beta_1 * b} \tag{2.5}$$

Where:

- f'_c = compressive strength of concrete
- b = width of the compression face of the member

Balanced strain conditions exist in a member when the tension reinforcement reaches its specified yield strength at the same time the concrete in compression reaches its assumed ultimate strain of 0.003. Sections are compression-controlled when the net strain in the tensile reinforcement is less than the assumed strain limit for concrete when the concrete reaches the assumed strain limit. Providing more reinforcement than is required for the balanced strain condition results in compression-controlled sections. Sections are tension-controlled when the net strain in the tensile reinforcement is greater than or equal to 0.005 at the same time the concrete reaches its assumed strain limit of 0.003. When the net tensile strain is between 0.003 and 0.005 as the concrete reaches its strain limit, the section falls within the transition zone between compression-controlled and tension-controlled (AASHTO, 2018a).

2.6.1 FRC Flexure

The previously mentioned assumptions for the flexural response of reinforced concrete also apply to FRC, including that the tensile capacity of the concrete is negligible. The tension force is carried by bonded reinforcement, which is comprised of fibers for structural FRC. There are several issues that have complicated a direct tension test for FRC: concrete crushing at the grips, stiffness of the testing machine, gauge length, mode of test control, and number of cracks observed (ACI Committee 544, 2018). Because of these issues, the standard test methods require calculating the tensile properties of FRC from data obtained during flexural tests.

ASTM C1609/C1609M contains the test that has been accepted in the United States to determine the tensile capacity of FRC. A mini-beam with an 18-inch span is subjected to four-point bending until it reaches a deflection of L/150, or 0.12 inches, at midspan. The loads corresponding to deflection values at maximum deflection, L/150 and L/600, are recorded as data points. The only load control option prescribed in this test method is deflection. Finally, the flexural residual loads are converted into stresses by assuming a linear stress distribution. (ASTM C1609/C1609M, 2012). A conversion can be made between the residual flexural strength and the residual tensile strength of FRC; the flexural strength is approximately 2.5 to 3 times greater than its tensile strength (ACI Committee 544, 2018).

The European test for determining the tensile properties of FRC is the EN 14651 test. A mini-beam with a span of 20 inches and a notch at midspan is tested under three-point bending. A crack displacement transducer is used to monitor the crack-mouth opening displacement (CMOD) at the midspan notch. The magnitude of the force is reported when the CMOD is equal to 0.02, 0.06, 0.1, and 0.14 inches. The peak force is also reported. This test allows the load to be controlled by the displacement of the beam or the rate of the CMOD. Similar to ASTM C1609/C1609M, the flexural residual loads are converted into stresses by assuming a linear stress distribution (EN 14651, 2005).

2.6.2 GFRP Flexure

The common assumptions previously listed for reinforced concrete also apply to concrete reinforced with GFRP. There are two additional assumptions used for all FRP reinforced concrete: the FRP is linear-elastic, and the FRP perfectly bonds with the concrete throughout the loading (ACI Committee 440, 2015). ACI 440.1R-15 also suggests the balanced failure reinforcement ratio for FRP-reinforced concrete be calculated using Equation 2.6.

$$\rho_{fb} = 0.85 * \beta_1 * \frac{f'_c}{f_{fu}} * \frac{E_f * \varepsilon_{cu}}{E_f * \varepsilon_{cu} + f_{fu}} \tag{2.6}$$

Where:

- ρ_{fb} = balanced reinforcement ratio
- β_1 = stress block factor
- f'_c = compressive strength of concrete
- f_{fu} = design tensile strength of FRP
- E_f = design modulus of elasticity of FRP
- ε_{cu} = ultimate concrete strain (0.003)

If the design FRP reinforcement ratio is greater than the balanced ratio, then the member is compression-controlled, meaning the concrete will crush prior to the FRP rupturing. The compression-controlled scenario leads to a closed-form solution to calculate the flexural capacity of an FRP-reinforced specimen. Per ACI 440.1R-15, the tensile stress in the FRP is calculated using Equation 2.7, and then Equations 2.4 through 2.5 can be used by replacing the yield stress of the tension reinforcement with the calculated value of tensile stress in the FRP. The tension-controlled scenario where the design FRP reinforcement ratio is less than the balanced ratio does not have a closed-form solution, but ACI 440.1R-15 allows a simplification to be made and the flexural capacity to be calculated with Equations 2.8 and 2.9.

$$f_f = \left(\sqrt{\frac{\left(E_f * \varepsilon_{cu}\right)^2}{4} + \frac{0.85 * \beta_1 * f'_c}{\rho_f} * E_f * \varepsilon_{cu}} - 0.5 * E_f * \varepsilon_{cu} \right) \leq f_{fu} \tag{2.7}$$

Where:

- f_f = FRP tensile stress
- ρ_f = design FRP reinforcement ratio

$$c_b = \frac{\varepsilon_{cu}}{\varepsilon_{cu} + \varepsilon_{fu}} * d \tag{2.8}$$

Where:

- c_b = depth to neutral axis at balanced condition
- ε_{fu} = FRP rupture strain

$$M_n = A_f * f_{fu} * \left(d - \frac{\beta_1 * c_b}{2}\right) \tag{2.9}$$

Where:

- A_f = area of tensile FRP reinforcement

In the *LRFD Bridge Design Guide Specifications for GFRP-Reinforced Concrete*, AASHTO presents an identical approach to the ACI method for the design of GFRP members as outlined herein (AASHTO, 2018b). There is a slight difference in the resistance factor AASHTO uses compared with ACI. The resistance factor has not been discussed in this document, but AASHTO allows its upper limit to be increased to 0.75 for compression-controlled members, while ACI uses 0.65.

2.7 Modulus of Subgrade Reaction

Structural elements such as concrete pavements, slabs-on-grade, and shallow footings are continuously supported by the underlying soil. The modulus of subgrade reaction stiffness is the parameter that defines the support underlying soils provide to the structural elements above them. The modulus is a ratio of applied soil pressure to deflection, as shown in Equation 2.10 (Walker & Holland, 2016). It is an often misunderstood and misused concept for the thickness design of continuously supported concrete elements. It is inaccurate to assume this parameter has a definite value for any given subgrade (Terzaghi, 1955).

$$K = \frac{pressure}{deflection} = \frac{\sigma}{\Delta} \tag{2.10}$$

Where:

- K = modulus of subgrade reaction

Walker and Holland explain the modulus of subgrade, K, reaction is not a fundamental soil property; rather, it is a parameter that should be adjusted from the subgrade reaction obtained from a plate load test. The adjustments are necessary because K is a function of the following:

- Underlying soil properties with respect to both initial and long-term response.
- Loading intensity that influences the long-term consolidation settlement.
- The area and shape of the loaded surface.
- The stiffness of the structural element, which influences the distribution of pressure.

For short duration loadings over small areas, such as moving wheel loads, long-term soil consolation is not a concern. Therefore, it is acceptable to use the subgrade reaction value from the plate load test as the stiffness parameter, K (Walker & Holland, 2016). In general, selecting a value for K is difficult because the modulus of subgrade reaction is not actually constant under a structural element. For a stiff structural element, the subgrade modulus will increase toward its edges. Assuming a constant, lower-bound value for K will produce upper-bound values of settlement, but it will not always result in a conservative design (Aristorenas & Gomez, 2014). Good engineering judgment must be exercised for each design scenario.

3. TESTING PROCEDURE

3.1 Introduction

This chapter contains an outline of the experiment that was designed and executed to compare different top mat reinforcement alternatives for concrete pavement panels with embedded IPTS. The scope of the experiment involved both high-cycle fatigue tests and static ultimate strength tests. To ensure quality was maintained throughout the experiment, consistency in the test procedures and protocols was paramount. The applicable testing standards designated by both the American Society of Testing and Materials (ASTM) and the European Standards (EN) were followed and are described herein.

Four concrete pavement slabs were constructed, each with a different top mat reinforcement alternative. Because the objective of this experiment is to focus on the durability and longevity of the pavement panels, they contained “dummy” IPTS that did not function. The sole purpose of the dummy IPTS was to emulate the structural voids created by an authentic IPTS. Each test slab was monitored by external strain gauges during the high-cycle fatigue testing.

After the fatigue testing was completed, each test slab was subjected to monotonic loading until failure. The ultimate residual strength was used for two primary reasons. First, it was used to directly compare the residual structural strengths of the composite test slabs between different alternatives. The ultimate strength for each test slab was also compared to a value obtained from a 3D finite element analysis (FEA) model. The purpose of the FEA model was to compare the residual structural strengths of the test panels to the expected ultimate strengths of the panels before being subjected to fatigue damage.

3.2 Concrete Test Slabs

The four concrete test slabs consisted of three slabs with different top mat reinforcement alternatives and one control slab with no reinforcement. The three alternative reinforcement options were as follows: fiber-reinforced concrete (FRC), glass fiber reinforced polymer (GFRP) rebar, and a fiberglass reinforced plastic (FRP) grid. Synthetic olefin macrofibers that were 1.5 in. long were used at a dosage of 5 lbs/cy of concrete for the FRC. The GFRP rebar mat was constructed with #3 bars spaced at 6 in. on center in each direction. The bars were manufactured with surface undulations and sand coatings to provide better bonding to the concrete matrix. The FRP grid was a ½-in.-deep square mesh grate with 3/16-in.-thick bars spaced at 2 in. on center. Two inches of cover was maintained between the top of the slab and the reinforcement for each alternative. Diagrams and photos of all the test slab alternatives can be seen below in Figures 3.1 through 3.10.

Although the method of reinforcing the top of the concrete test slabs varied for each alternative, all other aspects of the slabs remained consistent. Each slab was 4 ft. x 2 ft. x 10 in. The length and width of the test slabs were scaled down for economy and ease of testing, but the depth remained near a value that could be expected for a full-scale slab. A more realistic depth of test slabs was chosen to ensure the vertical stress distribution through the slabs accurately modeled the expected in-situ conditions for full-scale concrete pavement slabs. Plan and elevation diagrams of the test slabs can be seen in Figures 3.1 and 3.2, respectively.

Per the AASHTO *LRFD Bridge Design Specifications*, the contact area for a wheel load is 20 in. x 10 in., and the wheelbase for the design truck is 6 ft. (AASHTO, 2018a). In the test slabs for this experiment, the wheelbase was reduced to 3 ft. and the dimensions for the contact area of the simulated wheel load were also reduced to half the size prescribed by AASHTO. The author recognizes this 50% reduction of dimensions results in a 75% reduction of the overall contact area. Because the applied load was not determined by a given pressure distributed over the contact area, maintaining one-dimensional geometric consistency along the length of the test slabs was prioritized over the correct ratio of contact area.

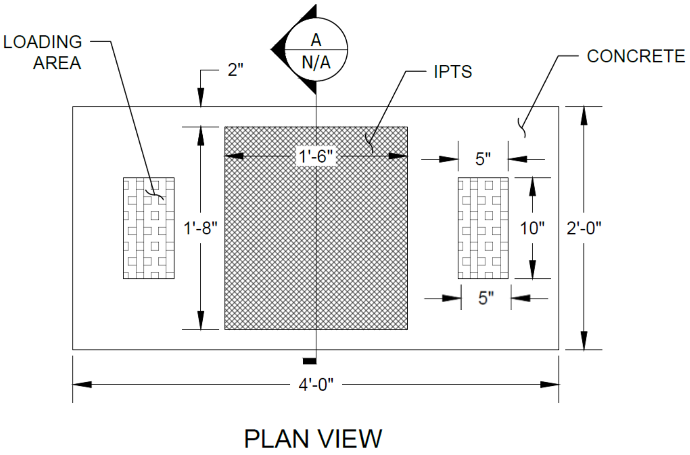

Figure 3.1 Plan Diagram of Test Slabs

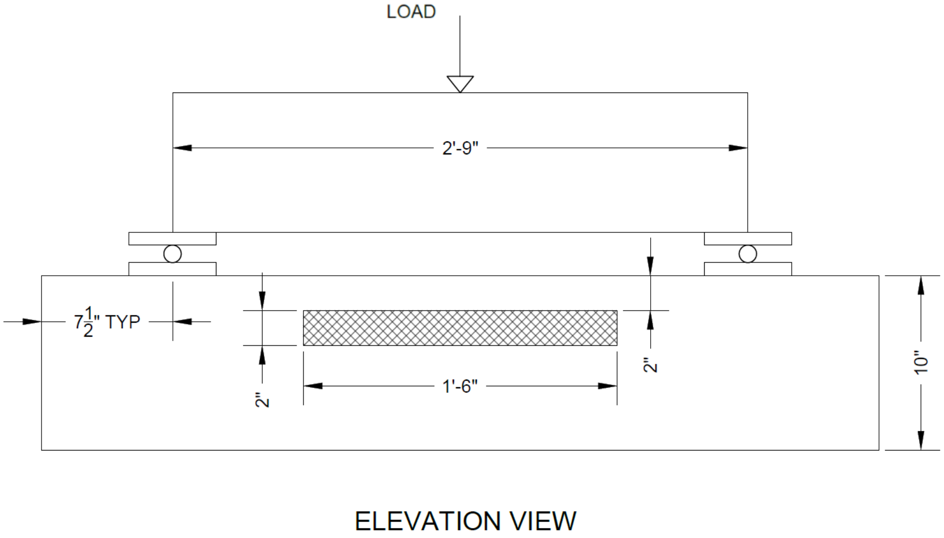

Figure 3.2 Elevation Diagram of Test Slabs

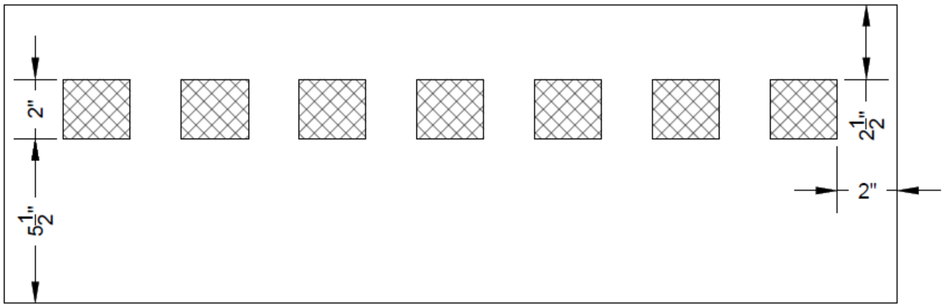

Figure 3.3 Cross-Section Diagram of Control Slab

Figure 3.4 Cross-Section View of Control Slab

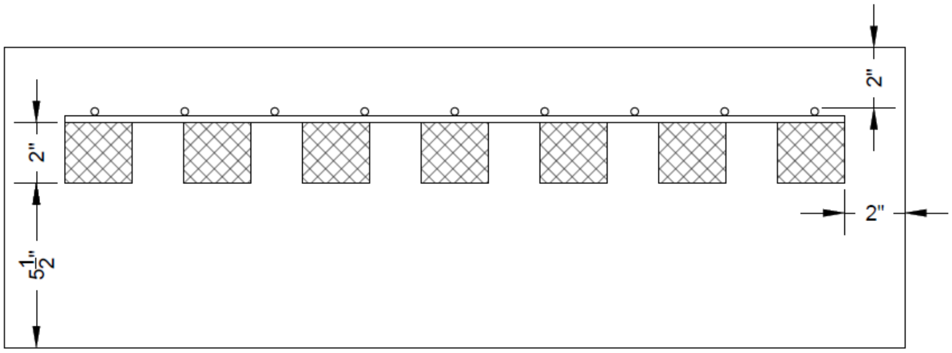

Figure 3.5 Cross-Section Diagram of GFRP Rebar Test Slab

Figure 3.6 Plan View of GFRP Rebar Test Slab

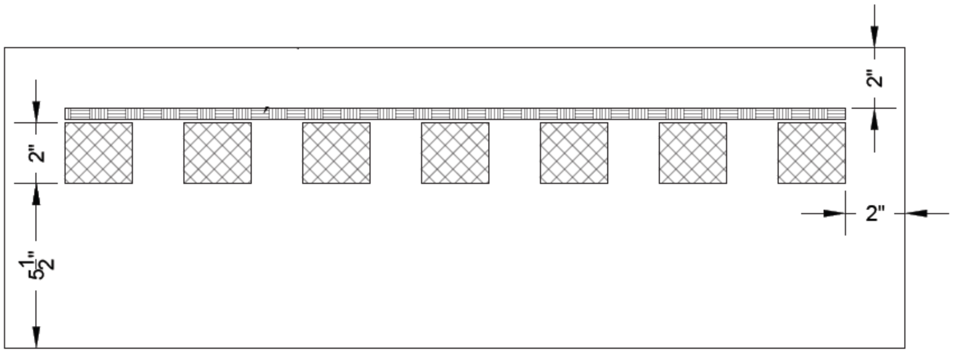

Figure 3.7 Cross-Section Diagram of FRP Grid

Figure 3.8 Isometric View of FRP Grid Test Slab

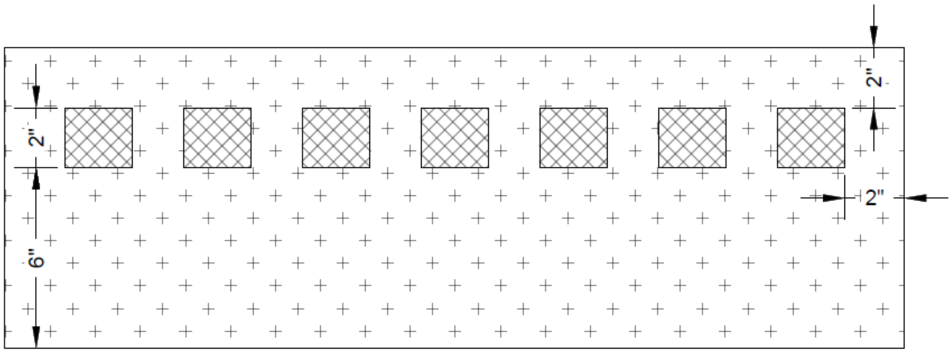

Figure 3.9 Cross-Section Diagram of FRC Test Slab

Figure 3.10 Pouring FRC Test Slab from Drum Mixer

Plastic U-channels and steel wire were placed in the middle 1 ft.–6 in. of all slabs to emulate an authentic embedded IPTS. The plastic U-channels were 2 in. wide, 2 in. deep, and 0.25 in. thick. The channels were placed at 3.875 in. on center to mimic the authentic IPTS that were installed in previous iterations of test slabs. Rubber coated #4 gauge steel wire interwoven across the top of the plastic U-channels was used to replace the Litz wire found in the authentic IPTS. More details of the previous test slabs and their embedded IPTS are provided later in this section.

The concrete used in the construction of all four test slabs was ordered from a local batch plant. The mix design called for a compressive strength of 8,000 psi and a slump of 8.0 in. To further increase the flowability of the fresh concrete, No. 8 pea gravel was used as the coarse aggregate. This same mix design was used to construct the previous iterations of concrete pavement panels in the preceding research performed at Utah State University. Refer to Appendix A for the detailed mix design.

All slabs were constructed at USU's Systems, Materials, and Structural Health (SMASH) Laboratory. The forms were built using oriented strand board (OSB) plywood supported by a 2 ft. x 4 ft. frame to ensure accurate dimensions with little to no deformation during the construction process. An identical mock IPTS was installed in each form and can be seen in the plan view in Figure 3.11. Where applicable, the top mat reinforcement alternative was then attached to the mock IPTS to ensure floating did not occur during the placement of the wet concrete. Upon delivery of the concrete, a slump test measured the slump to be 9.75 in. The macro fibers for the FRC slab were added to the concrete on site at the SMASH Lab. The concrete from the batch plant truck was loaded into a drum mixer where the correct dosage of fibers was added to the drum by hand to prevent clumping of the fibers. Three FRC mini-beams for the EN 14651 test and a sufficient number of concrete cylinders were also constructed. All concrete specimens were placed under an insulated tarp inside the climate controlled SMASH Lab until they were 28 days old. Additional photos from the construction of the test slabs can be seen in Appendix B.

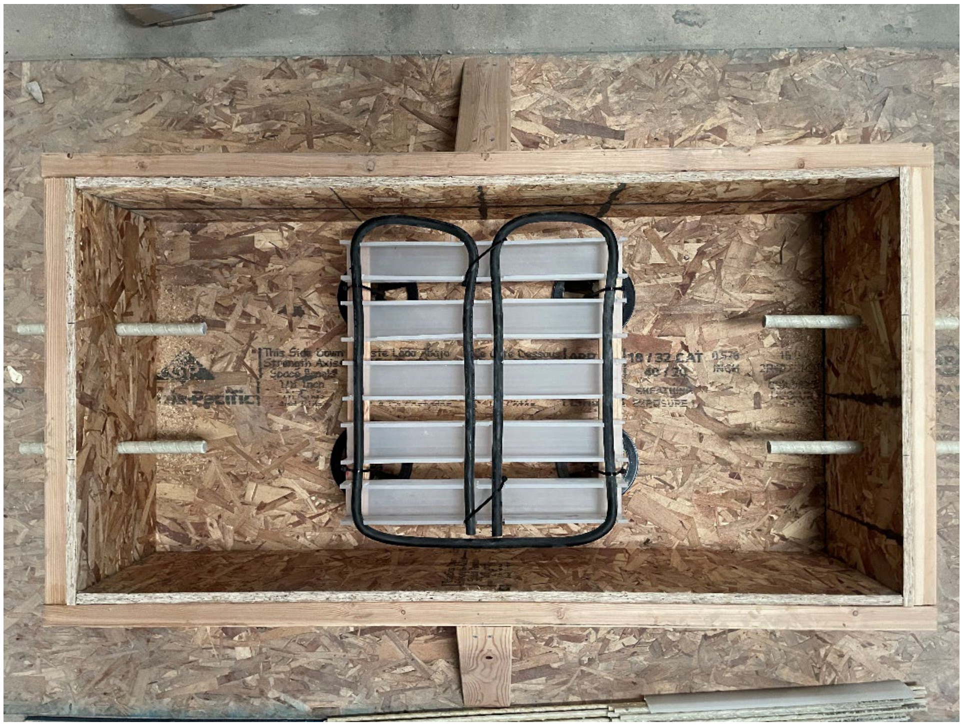

Figure 3.11 Plan View of Mock IPTS

3.2.1 Past Iterations of Concrete Test Slabs at Utah State University

Previous iterations of concrete pavement slabs with embedded IPTS have been constructed and tested in earlier research at USU. Raine tested two slabs with functioning IPTS: one slab with steel reinforcement and one with GFRP reinforcement (Raine, 2022). Another set of two slabs have since been constructed, but they have yet to be structurally tested. The purpose of this subsection is to provide more information on the details of the functioning IPTS used in similar research. A detailed explanation of the electrical components will not be provided, but a simple overview of how the system may affect the structural integrity of the concrete slab will be given.

The IPTS used by other researchers at USU consists of coils of Litz wire as close to the top surface of the concrete slab as feasibly possible. Directly beneath the Litz wire, there are plastic U-channels used to house ferrite bars. The purpose of the ferrite bars is to direct the magnetic field produced by the Litz wire toward the pavement surface. The plastic U-channels are 2 in. wide, 2 in. deep, and placed at 3.875 in. on center. All the channels are the same length and end at the same location, which creates a discrete discontinuity and stress concentrations in the concrete near the top surface of the pavement slabs. This configuration of Litz wire, plastic channels, and ferrite bars forms the top layer of the IPTS and can be seen in Figure 3.13 below.

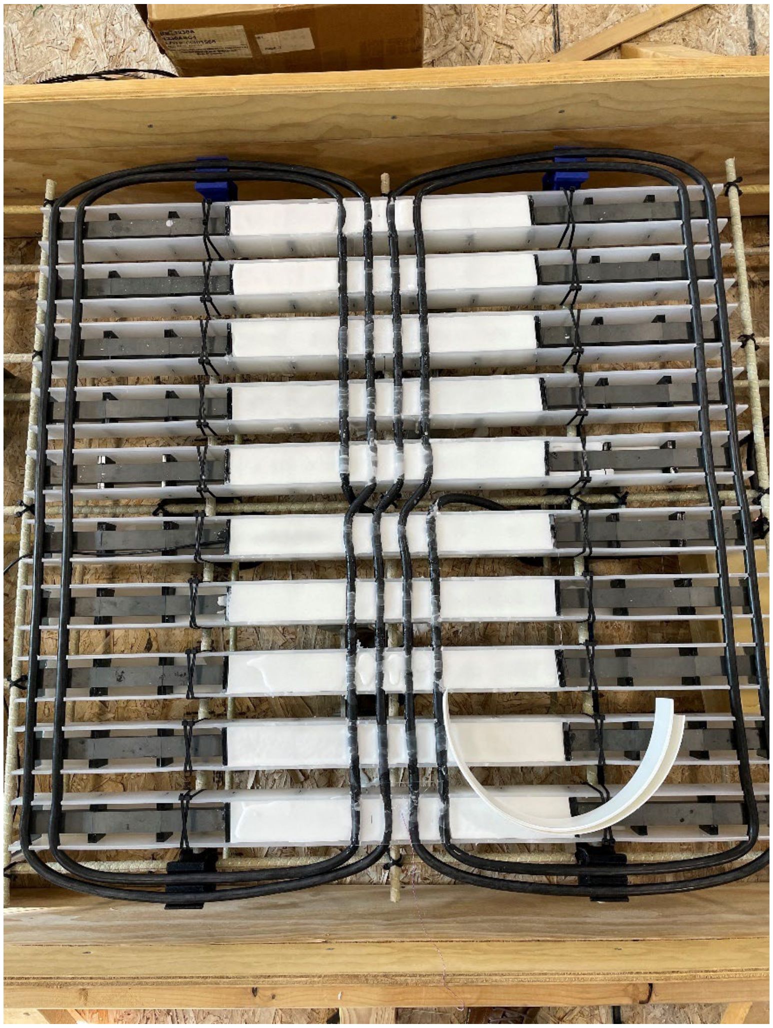

Figure 3.12 Top Layer of Functioning IPTS (Raine, 2022)

Beneath the top layer of the IPTS, there are several resin blocks dispersed throughout the concrete slab. The blocks of resin contain electrical components that are necessary for the system to function and form the inner core of the IPTS. The components are potted in resin to provide them an additional layer of protection. These blocks of resin and their associated wires used to interconnect the entire electrical system create discontinuities and structural voids within the slab as seen in Figure 3.14. The author assumes the resin selected by others for the blocks has adequate compressive strengths, but the bond between the resin and the concrete matrix is anticipated to be relatively weak. Additionally, the edges and corners of the resin blocks create points of stress concentration within the concrete matrix.

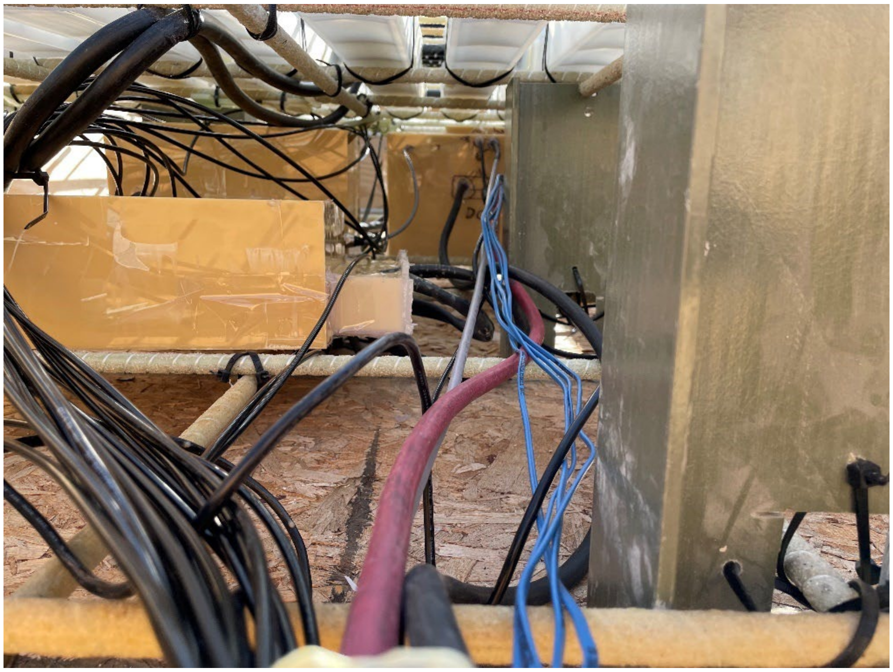

Figure 3.13 Inner Core of Functioning IPTS (Raine, 2022)

3.3 Materials Information and Testing Standards

3.3.1 Plain Concrete

The control slab, GFRP reinforced slab, and FRP reinforced slab all used plain concrete from a local batch plant. During the pouring process of the test slabs, 4 in. x 8 in. concrete cylinders were taken in accordance with ASTM C31 (ASTM C31, 2019). The cylinders were kept under an insulated tarp to maintain heat and moisture throughout the curing process. At least three cylinders were tested in compression and tension at the ages of 3 days, 7 days, and 31 days. Tests were performed at 31 days instead of the standard 28 days due to availability of equipment in the USU lab. The final compressive strength of the concrete was assumed to be equivalent to the value measured at 31 days.

The compressive strength of the concrete cylinders was tested in accordance with ASTM C39 (ASTM C39, 2012). Neoprene pads were used to cap the cylinders to ensure uniform contact between the testing apparatus and the cylinder. Figure 3.14 shows the compression testing setup and a typical failed concrete cylinder. The cylinders were loaded at a rate of 440 lb/min as specified in ASTM C39.

Figure 3.14 Typical Compression Testing Setup and Failed Cylinder

The tensile strength tests for the plain concrete were performed in accordance with ASTM C496 (ASTM C496, 2017). Each cylinder was placed on its side and loaded perpendicular to its longitudinal axis. To ensure uniform loading between the testing apparatus and the concrete cylinders, wooden shims were placed above and below the cylinders per the ASTM specification. The tensile testing setup is shown below in Figure 3.15, and a typical failed cylinder is shown in Figure 3.16.

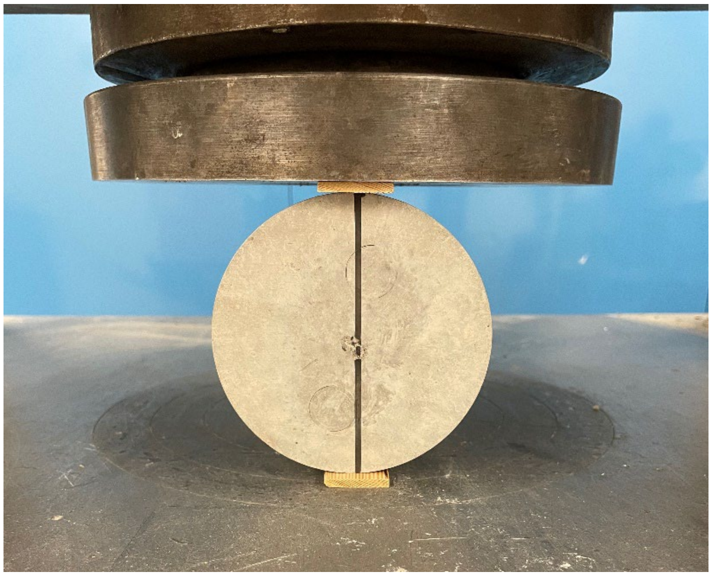

Figure 3.15 Tensile Test of Plain Concrete Cylinder

Figure 3.16 Plain Concrete Cylinder Failed During Tensile Test

3.3.2 Fiber Reinforced Concrete

The FRC slab was created by adding fibers at the SMASH Lab to the concrete from a local batch plant. The concrete to which the fibers were added came from the same truck that contained the concrete for the other test slabs. The fibers used to reinforce the FRC were Sika Fibermesh-650, which are synthetic macrofibers that comply with ASTM C1116/C1116M, Type III. They are typically used in industrial and commercial slabs on grade, precast reinforcement, and as replacement for wire mesh or steel rebar. In concrete, Fibermesh-650 has been proven to reduce cracking, improve residual strength, and enhance durability and toughness.

During the pouring process of the test slabs, 4 in. x 8 in. concrete cylinders were taken in accordance with ASTM C31 (ASTM C31, 2019). The cylinders were kept under an insulated tarp to maintain heat and moisture throughout the curing process. At least three cylinders were tested in compression at the ages of 3 days, 7 days, and 31 days. Tests were performed at 31 days instead of the standard 28 days due to availability of equipment in the USU lab. The final compressive strength of the concrete was assumed to be equivalent to the value measured at 31 days.

The compressive strength of the concrete cylinders was tested in accordance with ASTM C39 (ASTM C39, 2012). Neoprene pads were used to cap the cylinders to ensure uniform contact between the testing apparatus and the cylinder. The cylinders were loaded at a rate of 440 lb/min as specified in ASTM C39.

The tensile strength of FRC requires a different test method than for plain concrete. ASTM C1609/C1609M contains the test that has been accepted in the United States to determine the tensile strength of FRC, while the European standards follow the EN 14651 test. The details for the ASTM C1609/C1609M test are provided in Chapter 2 of this document. The procedure defined in the EN 14651 test was followed to obtain the tensile strength of the FRC. In previous research using the available test equipment at USU, it was confirmed the available test equipment is able to produce more accurate results by following the EN 14651 test rather than the ASTM C1609/C1609M test (McRory, 2020).

Three 6 in. x 6 in. x 22 in. mini-beams were cast using the FRC per the guidelines outlined in EN 14651 (EN 14651, 2005). A diagram of the required mini-beam geometry can be seen below in Figure 3.17. The mini-beams were kept under an insulated tarp to maintain heat and moisture during the curing process. After curing, a 1-in. (25 mm) notch with a width less than 0.2 in. (5 mm) was made at the midspan of each mini-beam using an MK Diamond brick saw with a 0.015-in. cutting blade as shown in Figure 3.18. The mini-beams were then tested under three-point bending with a span of 20 in. (500 mm). Figure 3.19 shows the test setup used in this experiment, and Figure 3.20 shows a typical cracked mini-beam with the CMOD transducer attached.

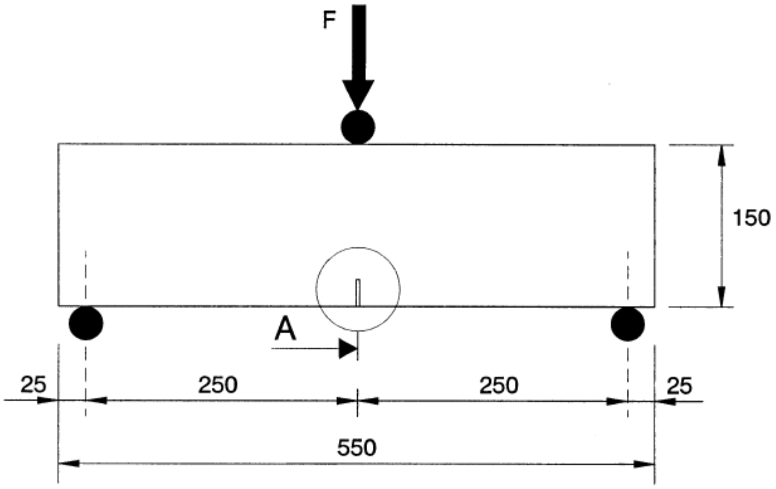

Figure 3.17 Diagram of Mini-Beam for Tensile Testing of FRC in mm (EN 14651, 2005)

Figure 3.18 Notching the FRC Mini-Beams

Figure 3.19 Test Setup to Obtain Flexural Strength of FRC per EN 14651

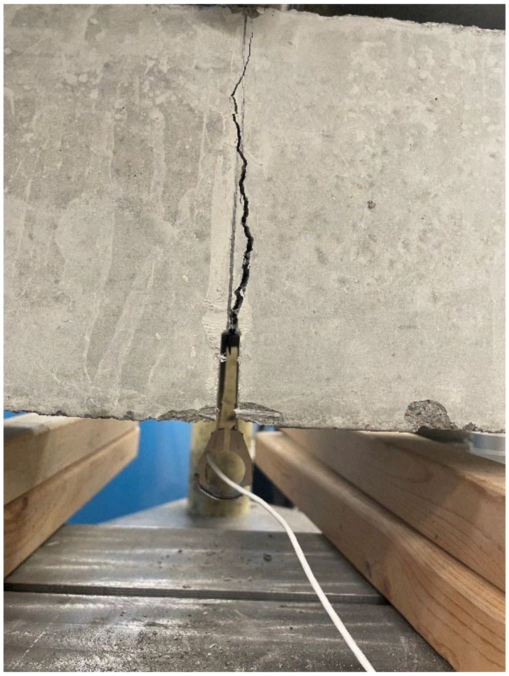

Figure 3.20 Typical Cracked Mini-Beam with CMOD Transducer

The rate of loading for the three-point bending test was controlled by deflection to better suit the feedback mechanism of the testing apparatus. As outlined in the EN 14651 test standard, the mini-beams were loaded at 0.003 in/min until the crack reached 0.005 in. wide; thereafter, the rate of loading was increased to 0.008 in/min until the crack width increased to at least 0.16 in. (EN 14651, 2005). The relationship between deflection and CMOD shown in Equation 3.1 was used to determine the necessary loading rates. After the three-point bending test was performed, the force vs CMOD curve was used to obtain the residual tensile strengths of the FRC for different crack openings. Equation 3.2 was taken from EN 14651 to determine the tensile strengths.

$$\delta = 0.85 * CMOD + 0.04 \tag{3.1}$$

Where:

- δ = Deflection, mm
- $CMOD$ = Crack-mouth opening displacement, mm

$$f_{R,j} = \frac{3 * F_j * l}{2 * b * {h_{sp}}^2} \tag{3.2}$$

Where:

- $f_{R,j}$ = Residual flexural tensile strength corresponding to CMOD_j, N/mm^2
- F_j = Applied load corresponding to CMOD_j, Newtons
- l = Span length, mm
- b = Width of the specimen, mm
- h_{sp} = Distance between the top of the notch and the top of the specimen, mm

3.3.3 GFRP Rebar

The GFRP used in this research was Aslan 100 #3 rebar. The bars are manufactured with a slight surface undulation created by an external helical wrap and a sand coating to enhance their bond strength. The fiber reinforcement within the bars is electrical grade glass fibers at a minimum volume fraction of 70%. Aslan uses a vinyl ester resin to encase the fibers. In a preceding research project at USU, McRory used GFRP rebar produced by the same manufacturer and procured from the same supplier as in this research. For this reason, additional testing to verify the tensile properties of the GFRP rebar is not required. McRory obtained the tensile properties through testing as prescribed in the ASTM D 7205 Standard (McRory, 2020). The bars were procured at different times and were likely not from the same production batch.

3.3.4 FRP Grid

ASTM D 7205 also details the standard method to obtain the tensile properties of an FRP grid specimen (ASTM D 7205, 2016). Linear specimens were cut from the grid to prepare them for tensile testing. Anchors on the linear specimens for the testing apparatus to grab are recommended but not required. As stated in ASTM D 7205, “Alternative methods for attaching the specimens to the testing machine are acceptable, but must allow for the full strength of the [specimen] to be developed and for the failure of the specimens to occur away from the attachments.” Anchors were not used for the testing of the FRP grid. The data from all specimens where the failure did not occur away from the attachments were rejected.

The free length between anchors was 16 in. An extensometer was placed at the mid-length position of each specimen. Per the standard, the minimum gauge length was determined to be 3.2 in. The linear specimens were anchored with textured grips at each end and loaded in direct tension. The rate of loading was deflection controlled at 0.16 in/min. Figure 3.21 shows the test setup used in this research, and a typical failed specimen is shown in Figure 3.22.

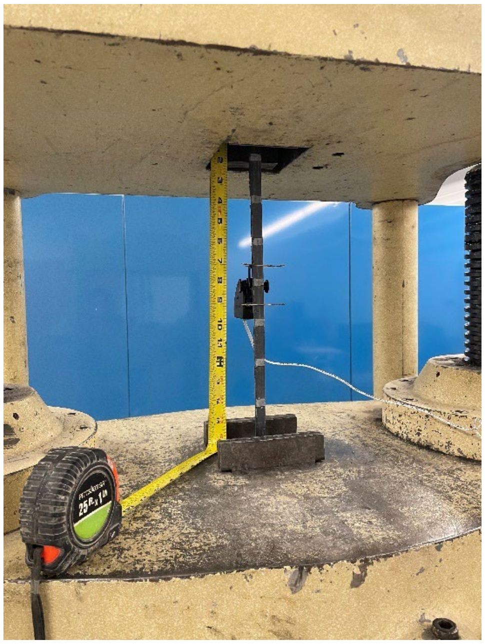

Figure 3.21 FRP Grid Tensile Testing Setup

Figure 3.22 Typical Failed FRP Grid Specimen

After testing, the data were used to calculate the ultimate tensile strength of the specimen, the tensile stress and strain at any given point during testing, and a chord modulus of elasticity. Equations 3.3 through 3.6 were used to calculate these properties.

$$F_{tu}=\frac{P_{max}}{A} \tag{3.3}$$

Where:

- F_{tu} = Ultimate tensile strength, psi
- P_{max} = Maximum applied force prior to failure, lbs.
- A = Cross-sectional area of test specimen, in.^{2}

$$\sigma_i = \frac{P_i}{A} \tag{3.4}$$

Where:

- σ_i = Tensile stress at the i-th data point, psi
- P_i = Applied force at the i-th data point, lbs.

$$\varepsilon_i = \frac{\delta_i}{L_g} \tag{3.5}$$

Where:

- ε_i = Tensile strain at the i-th data point, in/in
- δ_i = Extensometer displacement at the i-th data point, in.
- L_g = Extensometer gage length, in.

$$E_{chord} = \frac{\Delta\sigma}{\Delta\varepsilon} \tag{3.6}$$

Where:

- E_{chord} = Chord modulus of elasticity, psi
- $\Delta\sigma$ = Difference in tensile stress between start and end data points, psi
- $\Delta\varepsilon$ = Difference in tensile strain between start and end data points, in/in

3.4 Procedure for Fatigue Analysis

3.4.1 Testing Setup

To simulate some elasticity that is inherent with all sub-pavement sections, each slab was supported on a bed of gravel 3.5 in. thick. Although it is not likely the 3.5 in. gravel bed accurately simulates an in-situ condition, it does provide some amount of elasticity that will remain constant between the different alternatives. As discussed in Chapter 2, the subgrade modulus of underlying material can affect the performance of structural components. Due to budget constraints, this research project was not able to test identical test slabs on varying support conditions with different subgrade moduli. All feasible steps were taken during the fatigue testing process to ensure the subgrade modulus of the gravel bed remained constant between the alternative test slabs, thereby allowing for good comparison of the results between the test slabs.

On top of the slabs, two 5 in. x 10 in. contact areas supported a spreader beam in a three-point bending setup. The distance between the center point of the contact areas was 3 ft. One contact area contained a pinned support to the spreader beam, and the other contact area carried a roller support. The pinned and roller supports can be seen in Figures 3.23 and 3.24, respectively.

Figure 3.23 Typical Pinned Support

Figure 3.24 Typical Roller Support

At the center of the spreader beam, an MTS 110-kip servo hydraulic actuator was used to apply cyclic loading to the system. The MTS actuator was hanging from a steel strong frame capable of resisting 1,200 kips of shear loading. The entire fatigue testing setup is shown below in Figure 3.25. Each slab was instrumented with five external strain gauges, and a sixth gauge was left unattached to measure any possible drift in the data due to temperature or other ambient anomalies. As shown in Figure 3.26, gauges 1, 2, 5, and 7 were all located along the midpoint of the slabs. Gauges 1, 2, and 5 were parallel to the long dimension of the slabs and gauge 7 was transverse. Gauges 5 and 7 were placed in the middle of the slabs, while gauges 1 and 2 were placed on either side of the top corner of the slabs, but still at midpoint. Gauge 6 was centered above the discontinuity created by the end of the mock IPTS, and gauge 8 was left unattached. This strain gauge configuration assumes the stresses and strains experienced by the test slabs were bisymmetrical about the slab lengths and width axes.

Figure 3.25 Testing Setup for Fatigue Analysis

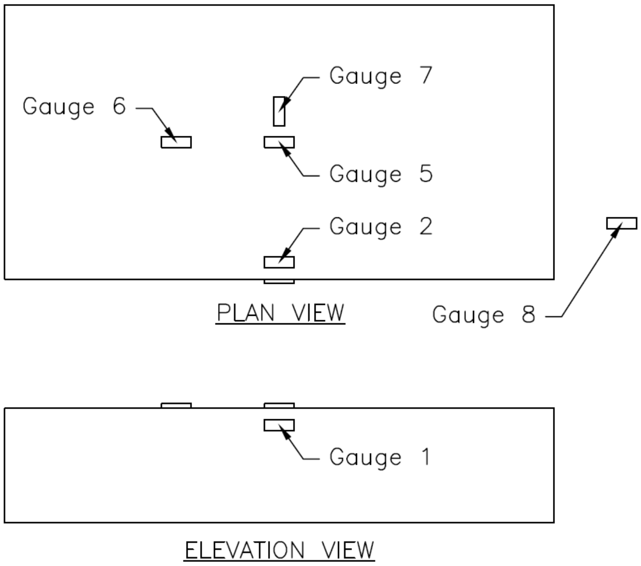

Figure 3.26 Strain Gauge Locations

3.4.2 Loading Scheme

The loading scheme consists of two aspects: loading schedule and loading magnitude. The loading schedule was determined based on previous research. Kumar et al. found the majority of cracking in reinforced concrete specimens subjected to cyclic loading occurs within the first 500,000 cycles (Kumar et al., 1998). Therefore, each test slab was subjected to 500,000 cycles of sinusoidal loading at a frequency of 2 Hz. The loading was broken into three stages, each with a different loading magnitude. The first two stages contained 200,000 cycles each, and the final stage contained 100,000 cycles. Table 3.1 below summarizes the loading scheme.

To accurately simulate realistic traffic conditions, the loading for the first stage of this experiment was derived from the HS-20 design loading defined in the AASHTO *LRFD Bridge Design Specifications* (AASHTO, 2018a). The HS-20 design loading has a maximum axle load of 32 kips with a 6-ft. wheelbase. Assuming constant elastic support beneath a 12-in.-thick pavement slab, this loading results in a maximum tensile stress of 329 psi in the extreme tension fiber at midspan. The load applied to the test slabs was adjusted to produce the same extreme tensile stress of 329 psi, which resulted in a load of 24.4 kips on the test slabs. For the second stage of loading, a review of a compilation of existing state truck weight limit laws revealed a common maximum axle weight of 50 kips (FHWA, 2019). The same process as described above resulted in a conversion of the 50 kips axle load to an applied load of 37.9 kips for the second stage of loading. Appendix C contains the hand calculations used to derive these loads. An applied load of 55 kips was selected for the final stage of loading to ensure cracking of the test slabs and observe their residual strength after cracking.

Table 3.1 Loading Scheme for Fatigue Analysis

Loading Stage	No. Cycles	Magnitude (kips)
1	200,000	24.4
2	200,000	37.9
3	100,000	55.0

To ensure constant engagement and reduce any possible drift of the testing setup during the fatigue cycling, a minimum load of 5 kips was maintained. At the beginning of the testing, the minimum load was applied at a constant rate of increase over a period of 10 seconds and allowed to dwell for 5 seconds before continuing. After the dwell period, the hydraulic actuator began the cyclic loading for the predetermined number of cycles. At the end of the cyclic loading, the minimum force was allowed to dwell for 5 seconds again, after which the minimum load was removed. The MTS hydraulic actuator is controlled by proprietary software, and Figure 3.27 shows the diagram for one loading stage of the fatigue testing. At the completion of loading stages 1 and 2, the following loading stage was immediately started so as to not provide a stress relaxation period for the test slabs.

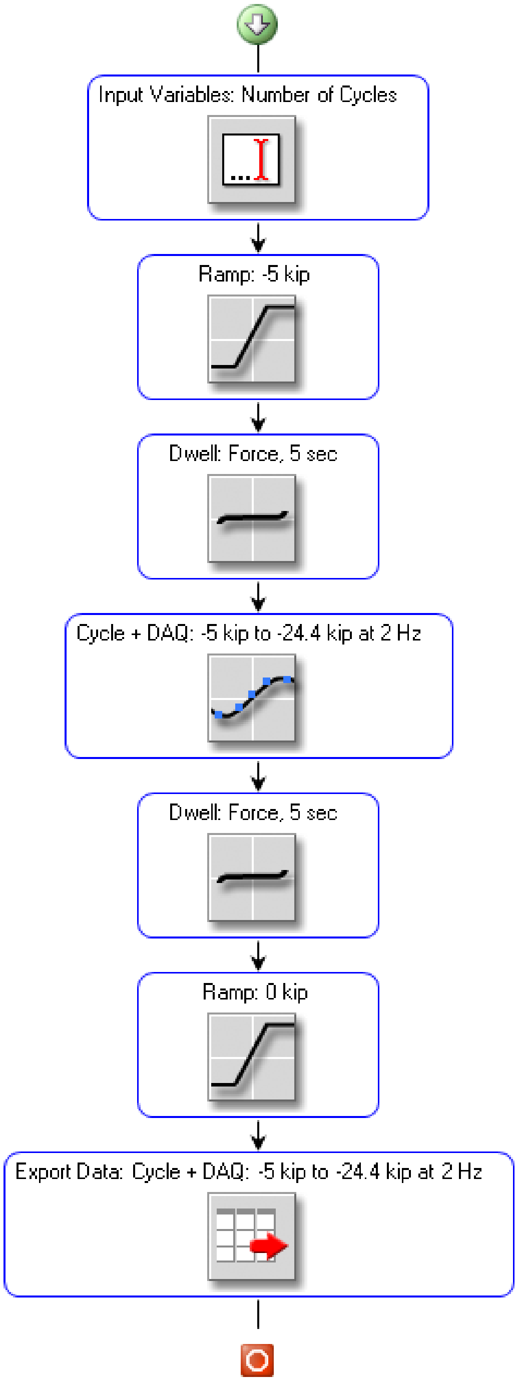

Figure 3.27 Fatigue Testing Loading Stage Diagram

3.5 Procedure for Ultimate Strength Analysis

After the test slabs underwent all three stages of loading for the fatigue analysis, each slab was subject to a monotonic load until failure to obtain the ultimate residual strength. The monotonic load was applied as described in ASTM C293, *Standard Test Method for Flexural Strength of Concrete (Using Simple Beam with Center-Point Loading* (ASTM C293, 2016). Each test slab was flipped so the top mat reinforcement was opposite the applied load. The full width of each slab was supported by a pin connection on one end and a roller connection on the other end. The connections were centered 6 in. away from the ends of the slabs, which resulted in a clear span of 3 ft. A steel rod with a diameter of 1.5 in. was placed on top of the slabs at midspan. The MTS 110-kip servo hydraulic actuator was then used to apply the loading to the steel rod, which distributed the load to the full width of the test slabs. Figure 3.28 shows the ultimate strength analysis testing setup, and Figure 3.29 shows the diagram of the program used to apply the loading through the hydraulic actuator.

Figure 3.28 Testing Setup for Ultimate Strength Analysis

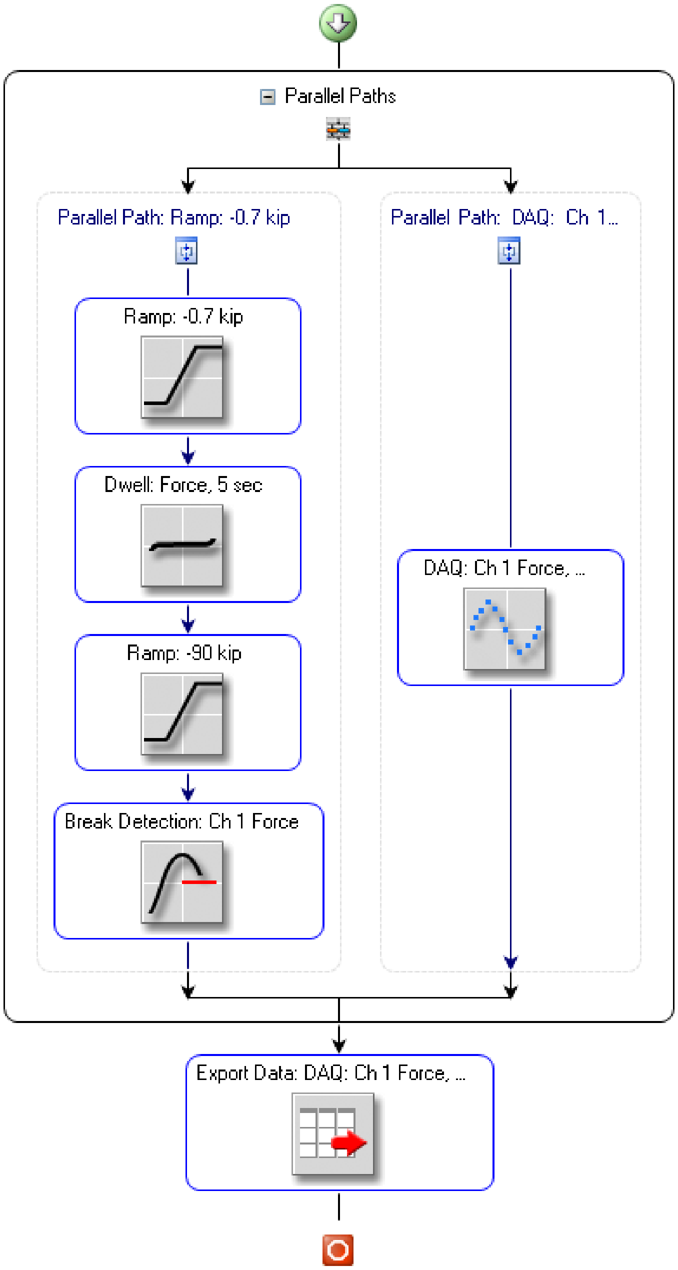

Figure 3.29 Ultimate Strength Testing Loading Diagram

Per ASTM C293, the initial load applied to the test slabs was 3% of the estimated ultimate load. The estimated ultimate load for the control slab was conservatively used as the starting point for all the test slabs. Its estimated ultimate load was calculated using Equation 3.7 (ASTM C293, 2016) and verified using Equation 3.8 (ACI 318, 2019). There was a 1.5% variance between the results from the two equations, and 3% of the minimum value was used as the initial applied load. The loading was increased at a constant rate until specimen failure. Equation 3-9 was used to calculate the required loading rate

(ASTM C293, 2016). Appendix C contains detailed hand calculations for all the equations mentioned above.

$$P_{ult} = \frac{R * 2 * b * d^2}{3 * L} \tag{3.7}$$

Where:

- P_{ult} = Estimated ultimate load, lbs.
- R = Calculated modulus of rupture, psi
- b = Average width of specimen, in.
- d = Average depth of specimen, in.
- L = Span length, in.

$$P_{ult} = \left(\frac{R * I}{0.5 * d} - \frac{w * L^2}{8}\right) * \frac{4}{L} \tag{3.8}$$

Where:

- I = Moment of inertia of specimen, in.^{4}
- w = Weight of specimen per lineal foot, lbs/ft

$$r = \frac{2 * S * b * d^2}{3 * L} \tag{3.9}$$

Where:

- r = Loading rate, lbs/min
- S = Rate of increase in the maximum stress on the tension face, psi/min

3.6 Procedure for 3D Finite Element Analysis

A 3D finite element analysis (FEA) model was created to estimate the ultimate strength values for each test slab prior to being subjected to fatigue damage. The purpose of the FEA model was to compare the expected ultimate strength values for each slab to the measured residual strength values. By assuming the FEA models accurately represent the physical test slabs, the difference between the expected ultimate strength values and the measured residual strength values becomes representative of the amount of damage each test slab experienced during fatigue testing. A test slab that experienced less fatigue damage would be considered more resilient and a favorable alternative.

ANSYS Workbench 2021 R2 was the FEA software used to create the models. The geometry for each alternative was created, including the internal components, and the material properties obtained during testing were assigned to the model components. A uniform pressure over a 1-in. wide strip at the midspan of the slabs was used to apply the load. The boundary conditions were modeled as a pin roller to imitate the physical tests performed in this research. Figures 3.30 through 3.32 show the geometric models for each test slab.

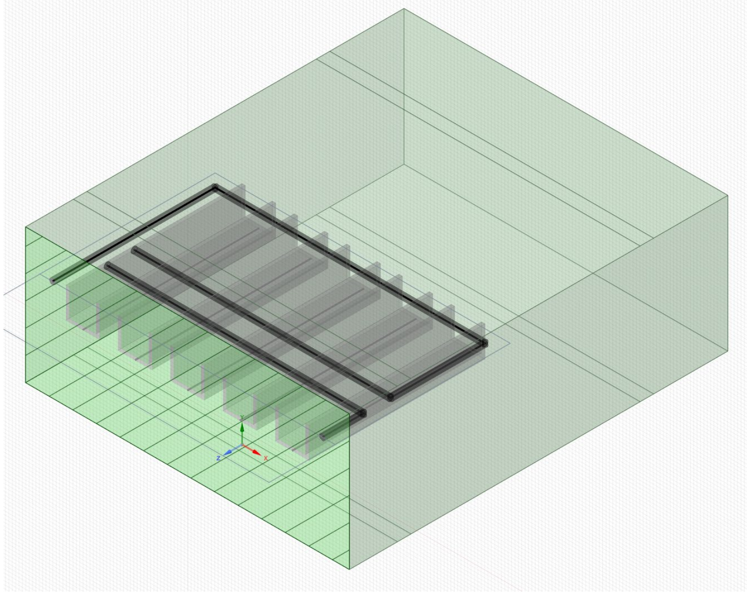

Figure 3.30 Model Geometry for Control Slab and FRC Slab

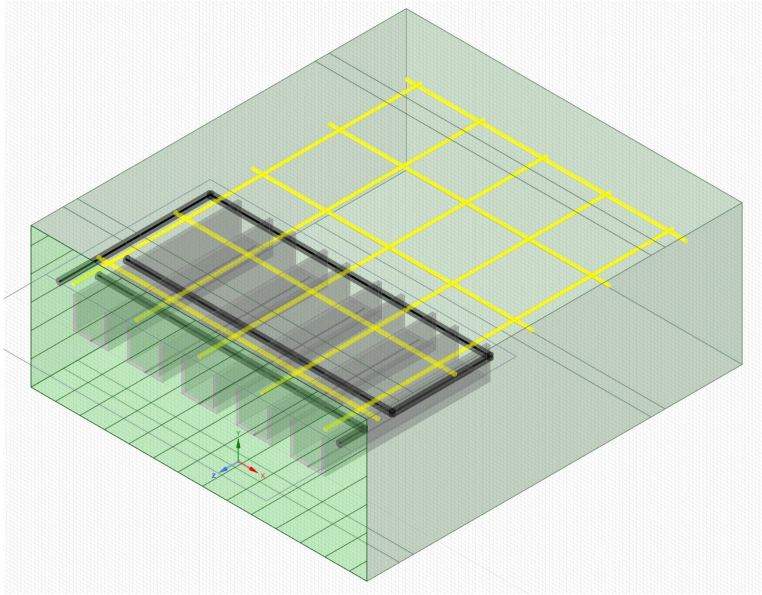

Figure 3.31 Model Geometry for GFRP Rebar Slab

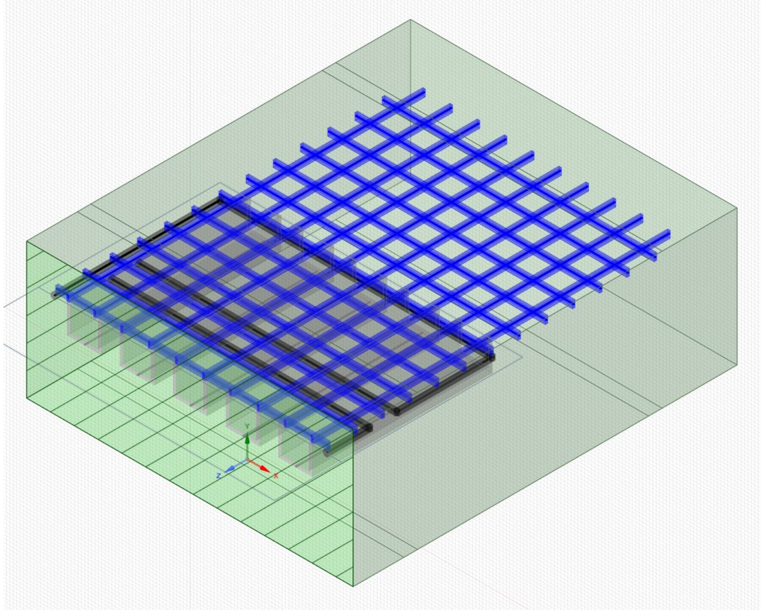

Figure 3.32 Model Geometry for FRP Grid Slab

An iterative analysis of the applied stress in the tensile reinforcement was used to determine the ultimate load capacity of each alternative. Because the control slab and the FRC slab did not have any discrete tensile reinforcement, the stress in the extreme tension fiber of the concrete was analyzed. The pressure applied to the loading contact area was increased until the applied stress in the tensile reinforcement was equal to the maximum allowable stress per the tensile material properties. When the applied stress equaled the maximum allowable stress in the tensile reinforcement, the test slab model was considered to reach its failure point, and its ultimate strength was assessed.

4. DATA ANALYSIS METHODS

4.1 Introduction

This chapter contains the data collection and analysis methodology used throughout this experiment. The datalogger and strain gauges that were used are described, including the measures taken to ensure the equipment was correctly calibrated. To conclude the chapter, the methods of data processing and analysis are detailed.

4.2 Data Collection Equipment

External data collection equipment was only required during the fatigue testing process. All tests to determine material properties used the internal sensors within the Tinius Olsen loading apparatus. The extensometer used during the testing of the FRP grid specimens was connected to the same datalogger as the Tinius Olsen and did not require additional software to record its data. During the ultimate residual strength testing for the slabs, the internal sensors of the MTS 110-kip servo hydraulic actuator were used to measure the deflection and applied force. However, an external datalogger was required to record the data from the strain gauges used during the fatigue testing process.

The datalogger used during the fatigue testing process was the Campbell Scientific CR3000 Micrologger. Its ability to monitor more than six different connectors simultaneously allowed the experiment to monitor the test slabs in several critical locations. Figure 4.1 contains a schematic diagram of the connection interface for the CR3000 (Campbell Scientific). The connections for this experiment were wired into VX Channels 1 and 2. All six strain gauges used in this experiment were BDI ST350 strain transducers, and each gauge was connected to the CR3000 as a resistive bridge. The data from the strain gauges were sampled at a rate of 10 Hz.

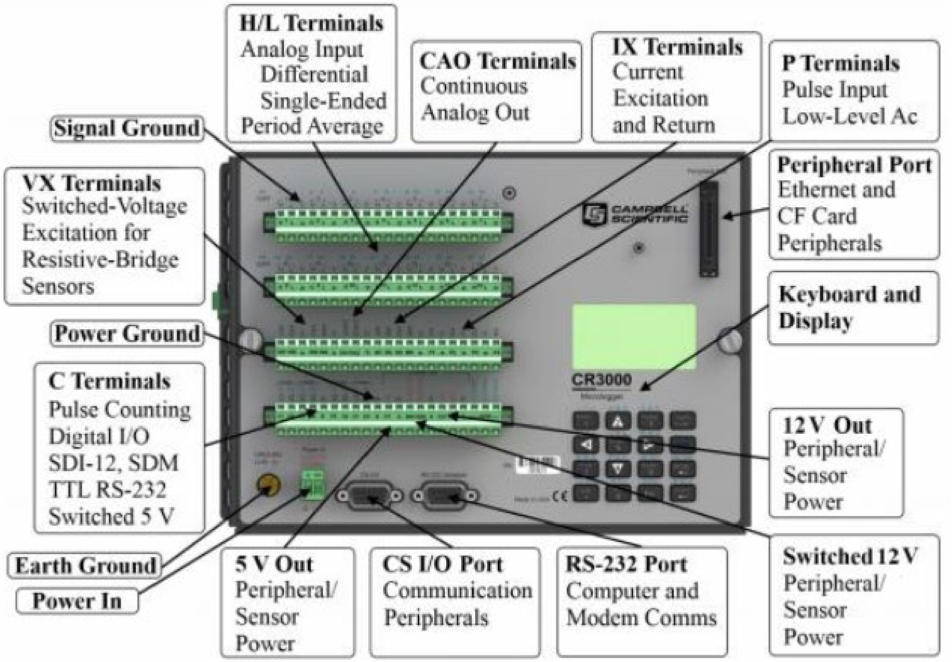

Figure 4.1 Schematic Diagram of the CR3000 Connection Interface (Campbell Scientific)

The BDI ST350 gauges measure minute changes in their electrical bridge circuits to detect changes in strain. Any strain applied to the gauges causes their electrical resistance to fluctuate. After passing a known voltage through the excitation channel to the strain gauges, the CR3000 can record any differences in the outgoing voltage. A general gauge factor (GGF) associated with each individual strain gauge is used to convert the outgoing voltage to a measurement of microstrain. Equation 4.1 was used to calculate the microstrain.

$$\mu\varepsilon = GGF * V_{out} \tag{4.1}$$

Where:

- $\mu\varepsilon$ = Microstrain, in/in*10^-6
- V_{out} = Output voltage, mV

The CR3000 requires written code to be uploaded in order to function as a datalogger. The code used with the CR3000 for data acquisition in this experiment was first developed during Raine's testing of previous concrete slab iterations at USU (Raine, 2022). The code contains modified GGFs for each strain gauge in order to accurately measure the microstrain. Appendix D contains the complete code used for this experiment.

4.3 Strain Gauge Calibration

As previously described, the CR3000 datalogger measures ingoing and outgoing voltage from the strain gauges and then uses a GGF to convert the voltage data to microstrain. The BDI ST350 strain gauges are reusable and can lose their calibration over time; therefore, a method to calibrate and verify the gauges data was devised. A wide flanged beam with known properties was arranged in a simple beam configuration beneath the MTS 110-kip servo hydraulic actuator. The strain gauges were fixed to the bottom of the beam at midspan while the hydraulic actuator was used to apply a known load to the top of the beam at midspan. The strain gauge calibration setup can be seen in Figure 4.2.

Figure 4.2 Strain Gauge Calibration Setup

The measured microstrain from the strain gauges was recorded with no applied load and also when loading was applied by the hydraulic actuator at four different magnitudes: 2000 lbs., 3000 lbs., 4000 lbs., and 5000 lbs. The expected microstrain at each loading magnitude was calculated using Equations 4.2 through 4.4. Using a linear regression method, a trendline for the measured data was used to calculate the R-squared value. The R-squared value represents the accuracy of the measured data relative to the expected data; a value of 1.00 means the datasets are directly correlated with no variance. In this experiment, an R-squared value of 0.95 or greater was deemed acceptable. If the R-squared value was less than 0.95, the GGF was modified and the calibration process repeated until the R-squared value was greater than 0.95. An example table and graph used to calibrate the strain gauges is shown in Figures 4.3 and 4.4. Appendix B contains the remainder of the strain gauge calibration tables and graphs.

$$M_{applied} = \frac{P_{applied} * l}{4} \tag{4.2}$$

Where:

- $M_{applied}$ = Moment applied to calibration beam, lbs*in.
- $P_{applied}$ = Load applied to calibration beam, lbs.
- l = Clear span of calibration beam, in.

$$\sigma_{applied} = \frac{M_{applied}}{S_m} \tag{4.3}$$

Where:

- $\sigma_{applied}$ = Maximum applied stress in the calibration beam, psi
- S_m = Section modulus of calibration beam, in.^{3}

$$\mu\varepsilon_{applied} = \frac{\sigma_{applied} * 10^6}{E} \tag{4.4}$$

Where:

- $\mu\varepsilon_{applied}$ = Microstrain, in/in*10^-6
- E = Modulus of elasticity of calibration beam = 29,000,000 psi

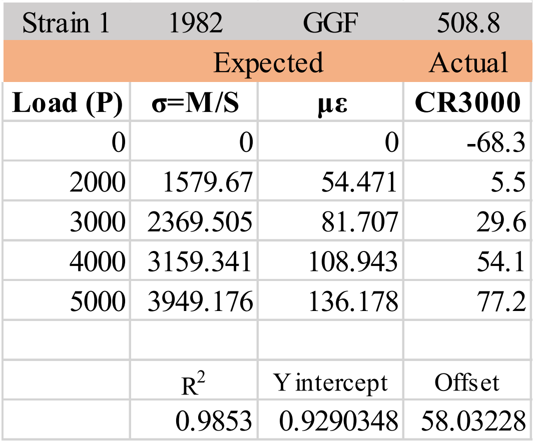

Strain 1	1982	GGF	508.8
	Expected		Actual
Load (P)	**σ=M/S**	**με**	**CR3000**
0	0	0	-68.3
2000	1579.67	54.471	5.5
3000	2369.505	81.707	29.6
4000	3159.341	108.943	54.1
5000	3949.176	136.178	77.2
	R^2	Y intercept	Offset
	0.9853	0.9290348	58.03228

Figure 4.3 Strain Gauge 1 Calibration Table

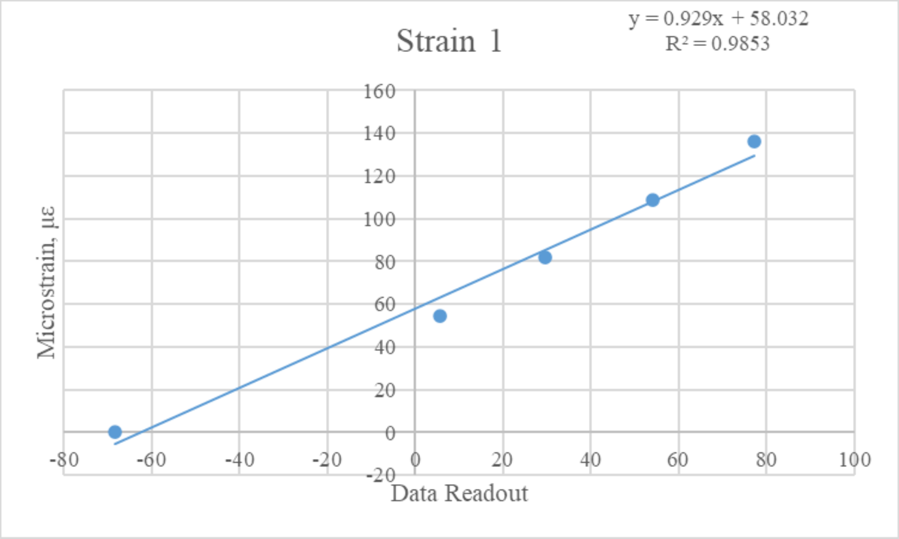

Figure 4.4 Strain Gauge 1 Calibration Graph

4.4 Data Processing

It is possible to apply strain to the BDI ST350 gauges during proper installation to a concrete specimen. For this reason, the data from each gauge were adjusted by a zero offset if required. The average strain value recorded prior to applying any load was used as the zero offset. The data were also inspected for any drift that may have occurred during testing. Strain gauge 8 was left unattached to monitor any potential drift. In all cases, no drift was present; therefore, no adjustment to the data was required.

The general trend of data from each strain gauge was also verified for each test. If the strain data were obviously errant compared with expected values, the data were rejected. Possible reasons for errant data include debonding of the strain gauge connection or major pinching of the strain gauge wire. Any such issues would have been corrected between stages of fatigue loading so the issues would not persist for the testing's entire duration.

The main processing operation applied to each dataset was filtering out the maximum strain values from each loading cycle. Because the loading was applied at 2 Hz and the data were sampled at 10 Hz, every loading cycle resulted in 5 data points. This ratio of data sampling to cyclic loading was chosen to increase the probability of collecting the true maximum strain for each loading cycle, which was then filtered out. This investigation is interested in the overall trend of the strain experienced by the test slabs through the progression of hundreds of thousands of loading cycles. The changes of strain experienced during one single load cycle are considered irrelevant. An example of this filtering process is shown in Figure 4.5 below.

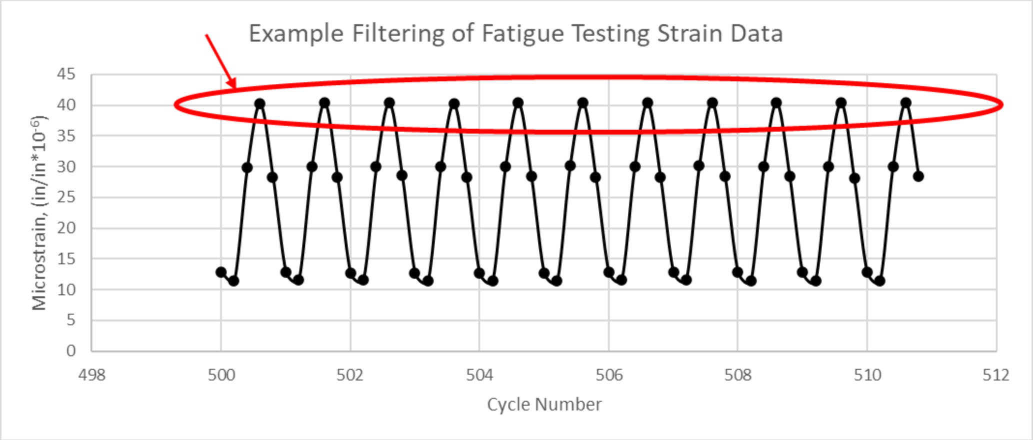

Figure 4.5 Example Filtering of Fatigue Testing Strain Data

5. COMPARISONS AND DISCUSSION OF RESULTS

5.1 Introduction

This chapter presents the data obtained during the procedures described in Chapter 3. Words, figures, and tables will be used to describe the data. First, the data resulting from the material testing on individual components used in the construction of the test slabs will be presented. After which, the results from the fatigue analysis and the ultimate strength analysis of the physical test slabs will be reviewed. Finally, the findings of the 3D finite element analysis (FEA) for each slab will be discussed and compared with the physical results.

5.2 Materials Testing

5.2.1 Plain Concrete

At least three viable concrete cylinders were tested at the age of 3 days, 7 days, and 31 days in both compression and tension. The compressive tests were performed according to ASTM C39 and the tensile tests per ASTM C496. Table 5.1 and Figure 5.1 contain the results from the compressive tests; Table 5.2 and Figure 5.2 display the results from the tensile tests. The average compressive strength of the plain concrete at 31 days was 5,291 psi, which is 34% below the mix design strength of 8,000 psi. The tensile strength was relatively low as expected at 366 psi, and it did not show a significant increase in strength as the specimens aged.

Equations 5.1 and 5.2 were taken from AASHTO *LRFD Bridge Design Guide* and used to calculate the modulus of elasticity, E, of the plain concrete (AASHTO, 2018a). The average compressive strength of 5,291 psi resulted in a concrete unit weight of 145.29 pcf and a modulus of 4,203.79 ksi.

$$E = 33{,}000 * K_1 * {w_c}^{1.5} * \sqrt{f'_c} \tag{5.1}$$

Where:

- K_1 = Correction factor for source of aggregate taken as 1.0
- w_c = Unit weight of concrete, kcf
- f'_c = Compressive strength of concrete, ksi

$$w_c = 0.140 + 0.001 * f'_c \tag{5.2}$$

Table 5.1 Plain Concrete Compressive Testing Results

Age of Specimen (days)	**Specimen No.**	**Compressive Strength (psi)**
3	1	4,287
3	2	4,129
3	3	3,968
3	Average	4,128
7	1	4,453
7	2	4,718
7	3	4,423
7	Average	4,389
31	1	5,234
31	2	5,293
31	3	5,347
31	Average	5,291

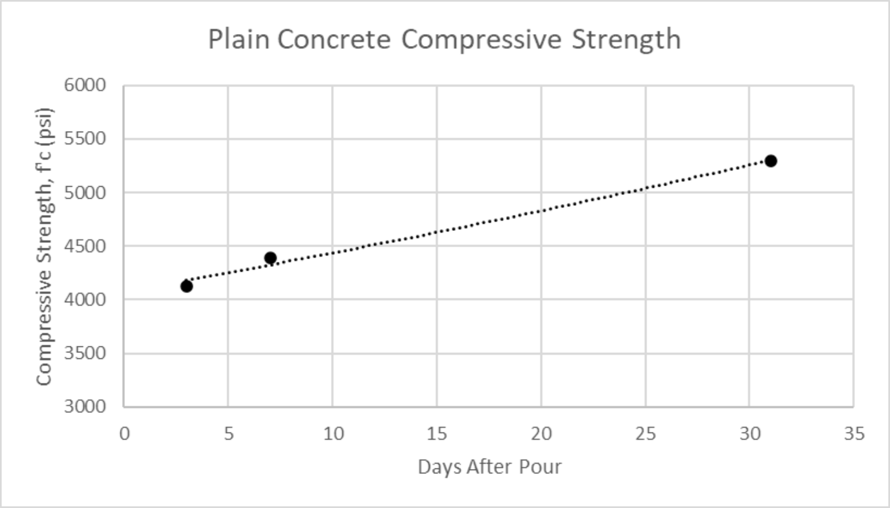

Figure 5.1 Graph of Plain Concrete Compressive Strength

Table 5.2 Plain Concrete Tensile Testing Results

Age of Specimen (days)	Specimen No.	Splitting Tensile Strength (psi)
3	1	455
3	2	324
3	3	326
3	Average	369
7	1	401
7	2	333
7	3	294
7	Average	343
31	1	369
31	2	386
31	3	342
31	Average	366

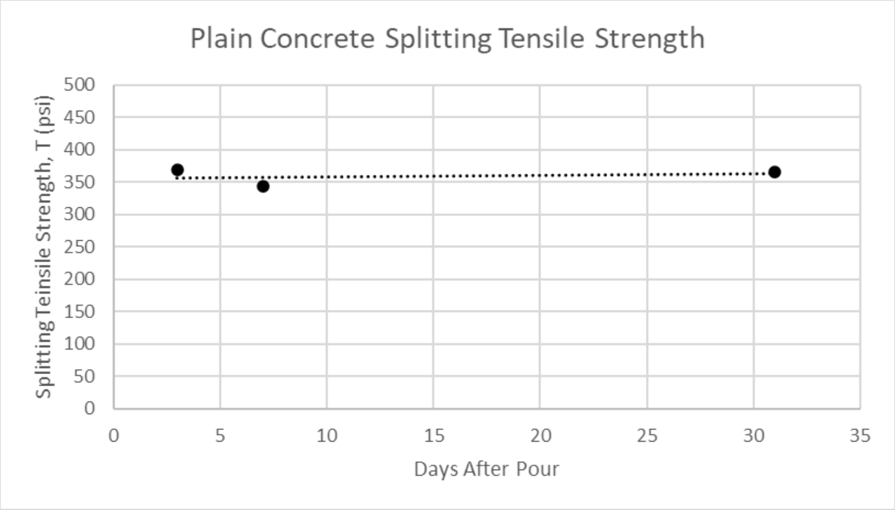

Figure 5.2 Graph of Plain Concrete Tensile Strengths

5.2.2 Fiber Reinforced Concrete

At least three viable concrete cylinders were tested at the age of 3 days, 7 days, and 31 days in compression according to ASTM C39. The results from the compressive tests are displayed below in Table 5.3 and Figure 5.3. The average compressive strength of the FRC at 31 days was 5,521 psi. Equations 5.1 and 5.2 from above were used to calculate a modulus of elasticity of 4,304 ksi for the FRC. The tensile properties of the FRC were obtained through testing three mini-beams using the procedure described in EN 14651. Figures 5.3 through 5.5 show the applied force vs. measured crack opening deflection. Table 5.4 contains the applied load and calculated residual tensile strength for each mini-beam at each design crack opening width prescribed in EN 14651 (EN 14651, 2005). The deflection values are displayed in both millimeters and inches because the data were collected in millimeters per the EN 14651 test protocol and then converted to inches. The maximum tensile strength for each FRC is displayed in Table 5.5, and the average maximum tensile strength is 548 psi, which is a 50% increase compared with the plain concrete.

Table 5.3 FRC Compressive Testing Results

Age of Specimen (days)	Specimen No.	Compressive Strength (psi)
3	1	4,288
3	2	4,169
3	3	4,061
3	Average	4,173
7	1	4,806
7	2	4,529
7	3	3,714
7	Average	4,350
31	1	5,434
31	2	5,521
31	3	5,606
31	Average	5,521

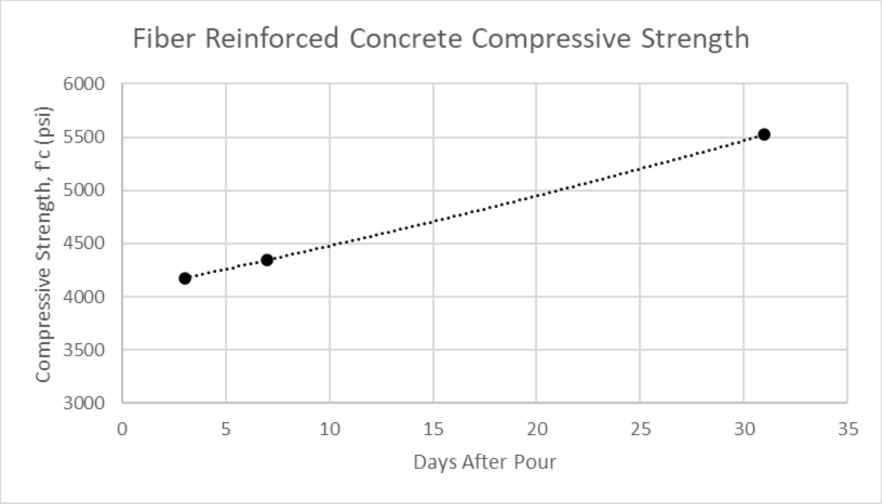

Figure 5.3 Graph of FRC Compressive Strengths

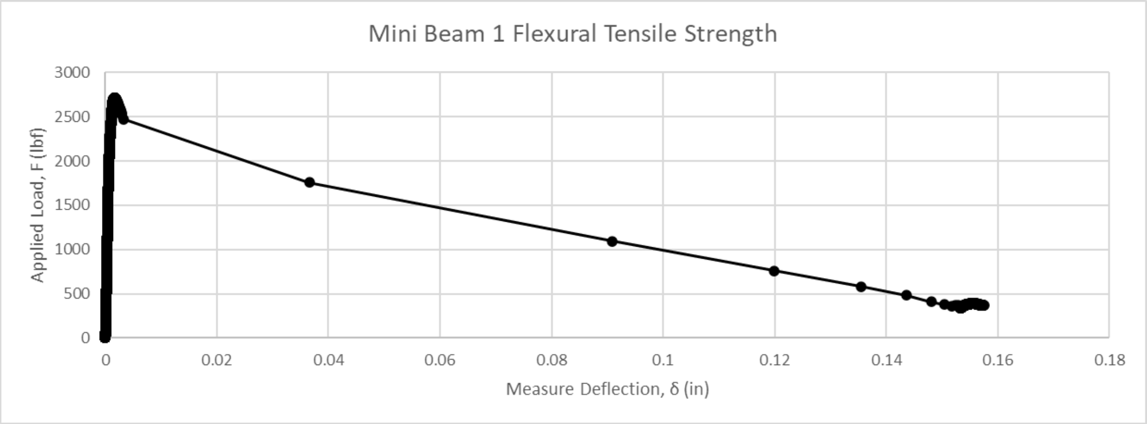

Figure 5.4 Graph of Mini-Beam 1 Flexural Tensile Testing

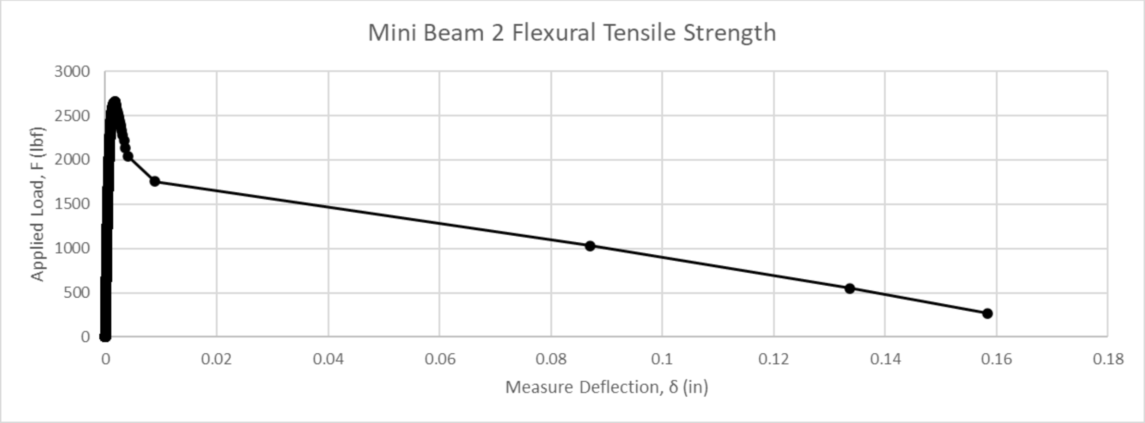

Figure 5.5 Graph of Mini-Beam 2 Flexural Tensile Testing

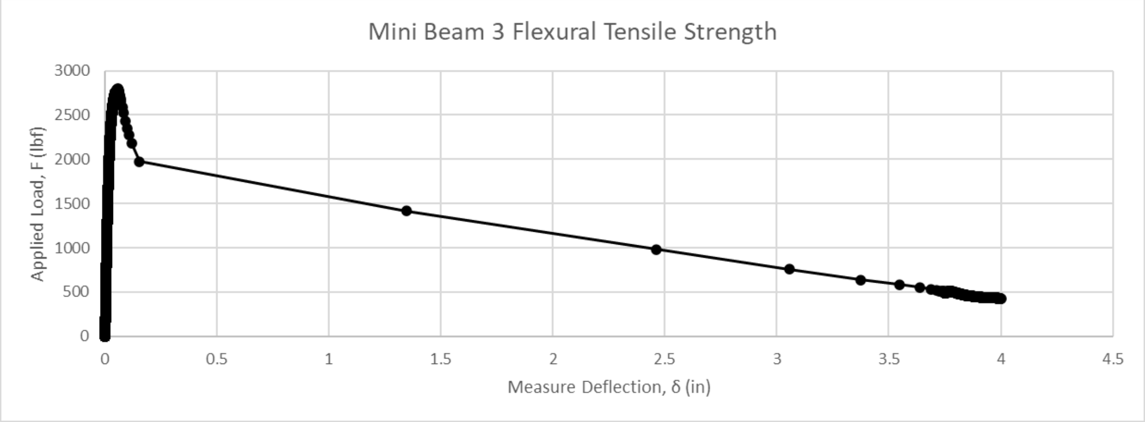

Figure 5.6 Graph of Mini-Beam 3 Flexural Tensile Testing

Table 5.4 Data from Flexural Tensile Testing of Mini-Beams

Mini Beam	Index	δ (mm)	δ (in)	F_i (lbs)	f_R (psi)
1	1	0.08	3.15E-03	2,521	515
	2	1.32	5.20E-02	1,757	359
	3	2.17	8.54E-02	1,757	359
	4	3.02	1.19E-01	1,093	223
2	1	0.08	3.15E-03	2,284	465
	2	1.32	5.20E-02	1,754	357
	3	2.17	8.54E-02	1,754	357
	4	3.02	1.19E-01	1,030	210
3	1	0.08	3.15E-03	2,590	509
	2	1.32	5.20E-02	1,974	388
	3	2.17	8.54E-02	1,417	278
	4	3.02	1.19E-01	980	192

Table 5.5 Maximum Tensile Strengths of Mini-Beams

Mini Beam	F_{max} (lbs)	δ (mm)	δ (in)	$f_{R,max}$ (psi)
1	2,714	0.041	1.61E-03	551
2	2,654	0.043	1.69E-03	540
3	2,793	0.057	2.23E-03	548
AVERAGE	2,720	0.047	1.85E-03	548

5.2.3 GFRP Rebar

McRory recently tested six Aslan 100 GFRP rebar specimens from the same manufacturer and supplier as used in this research. Two of the bars experienced failures inside of the anchors and were rejected. The four failures that occurred within the gauge length of the applied extensometer were recorded and compared. During his testing, McRory removed the extensometer at a load of 50% of the predicted failure load to prevent damage to the sensor. Linear behavior was observed prior to the removal of the sensor and the strain data were extrapolated to the failure point. Table 5.6 summarizes the material properties of the GFRP rebars recorded during McRory's testing (McRory, 2020).

Table 5.6 Material Properties of GFRP Rebar (McRory, 2020)

Property	Mean Value
Tensile Strength	119.7 ksi
Modulus of Elasticity	8,197 ksi
Rupture Strain	1.45%

5.2.4 FRP Grid

Nine linear specimens were prepared from the FRP grid and tested according to ASTM D7205. Specimens 4 and 5 both failed in the anchorage zone during testing, so the data from those specimens were rejected. The data from the remaining seven specimens are displayed in Table 5.7 along with the material properties calculated using the data. During the testing, the extensometer automatically calculated the internal strain experienced by the specimens by dividing its elongation by its original gauge length. The tensile strength was calculated using Equation 5.3, and the modulus of elasticity was calculated using Equation 5.4. The beginning stress point for Equation 5.4 was selected as 6,000 psi, and the ending stress point was 10,000 psi. The average values for the tensile strength and the modulus of elasticity of the FRP grid specimens were 18,328 psi and 3,137 ksi, respectively. As expected, linear behavior was expected up to the point of brittle failure. A typical load-deflection curve and stress-strain curve are shown in Figures 5.7 and 5.8 below.

$$F_{tu} = \frac{P_{max}}{A} \tag{5.3}$$

Where:

- F_{tu} = Ultimate tensile strength, psi
- P_{max} = Maximum applied force prior to failure, lbs.
- A = Measured cross-sectional area of the specimen, in.^{2}

$$E_{chord} = \frac{\Delta\sigma}{\Delta\varepsilon} * \frac{1\ ksi}{1000\ psi} \tag{5.4}$$

Where:

- E_{chord} = Chord modulus of elasticity, ksi
- $\Delta\sigma$ = Difference in applied tensile stress between the starting and ending stress points, psi
- $\Delta\varepsilon$ = Difference in tensile strain between the starting and ending stress points, in/in

Table 5.7 Summary of Data and Properties from FRP Grid Specimen Testing

Specimen No.	P_{max} (lbs)	Area (in^2)	F_{tu} (psi)	E (ksi)
1	1,988	0.108	18,418	3,118
2	1,646	0.108	15,249	2,796
3	1,789	0.107	16,787	2,733
6	2,730	0.106	25,647	3,717
7	1,824	0.108	16,818	3,262
8	1,670	0.107	15,646	3,178
9	2,121	0.107	19,733	3,156
AVERAGE			18,328	3,137

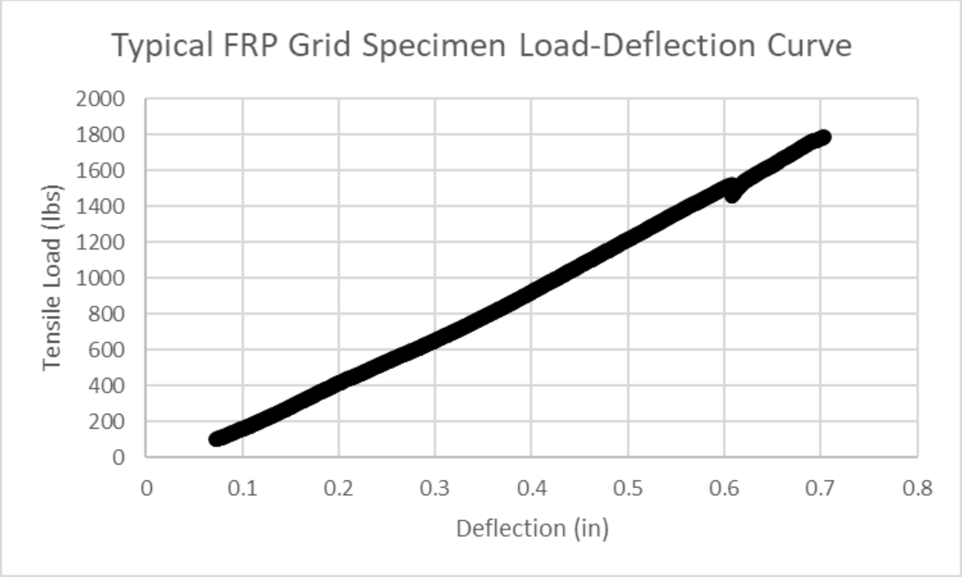

Figure 5.7 Typical FRP Grid Specimen Load-Deflection Curve

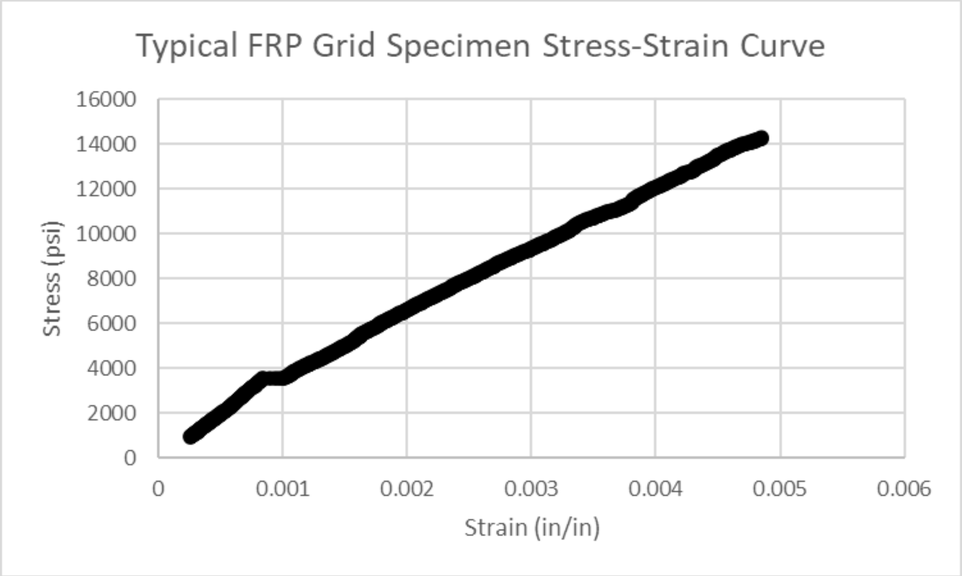

Figure 5.8 Typical FRP Grid Specimen Stress-Strain Curve

5.3 Fatigue Analysis Results

5.3.1 Introduction

Per the research program, each slab was to be subjected to 500,000 cycles of fatigue testing in three different loading stages. During setup for the fatigue testing of the control test slab, an equipment malfunction with the hydraulic actuator led to an immediate failure of the control slab before fatigue testing could take place. Figures 5.9 and 5.10 show the failure of the spreader beam and the resulting crack in the control slab. Because of this malfunction, the control slab was not subjected to the fatigue testing protocol. The other three alternative slabs were subjected to the complete fatigue testing protocol per the original testing procedure. After stage 2 of the FRP grid test slab fatigue testing, the computer had a hard drive failure during the data export process. The hard drive was removed and as much data as possible were recovered. Only the data from the first 56,000 cycles were able to be recovered; the remainder of the data from stage 2 were lost. The data from stage 2 of the fatigue testing for the FRP grid were uniquely affected by this hard drive failure; the data collected during the subsequent stage 3 are still valid.

The data obtained during the fatigue testing were collected using BDI ST350 strain transducers. The configuration of the location of the strain gauges is shown in Figure 3.22. To summarize, gauges 1, 2, 5, and 7 were all located along the midpoint of the slabs. Gauges 1, 2, and 5 were parallel to the long dimension of the slabs and gauge 7 was transverse. Gauges 5 and 7 were placed in the middle of the slabs, while gauges 1 and 2 were placed on either side of the top corner of the slabs, but still at midpoint. Gauge 6 was centered above the discontinuity created by the end of the mock IPTS, and gauge 8 was left unattached. The following subsections will present the data collected from the strain gauges and the measured crack widths for each test slab.

During stage 3 of the fatigue loading, each test slab was subjected to 100,000 cycles of the maximum applied load of 55.0 kips. Prior to stage 3, none of the test slabs experienced major cracking. At differing points during stage 3, all of the test slabs developed a flexural crack in the top of the slab near midpoint that progressed downward through the slab. The data from the strain gauges located along the midpoint of the test slab were inaccurate after cracking for at least one of the following reasons: the crack formed directly under the strain gauge anchor and caused debonding, the crack formed outside of the area between the strain gauge anchors, or the strain gauge anchors debonded without any direct influence from cracking. For this reason, the comparison between test slab alternatives during stage 3 of loading is based on measured crack widths instead of strain gauge data. The crack widths were measured using a digital caliper. For this reason, the widths are reported to the nearest hundredth of an inch so as to not imply a level of accuracy that was not achievable due to the method of measurement.

Figure 5.9 Control Slab Spreader Beam Failure

Figure 5.10 Control Slab Initial Crack

5.3.2 FRC Test Slab Fatigue Testing Data

Figure 5.11 contains the data from the strain gauges during stage 1 of the fatigue testing. During stage 1 of testing, gauges 1 and 6 showed the largest changes in microstrain. Although the exact values for gauges 2, 5, and 7 differ, the data from all three gauges display a similar trend and a slight increase in microstrain. Because gauge 6 recorded a significantly larger change in microstrain than gauge 5, it can be concluded the lower magnitude loading during stage 1 did not have a large effect on the midspan of the test slab.

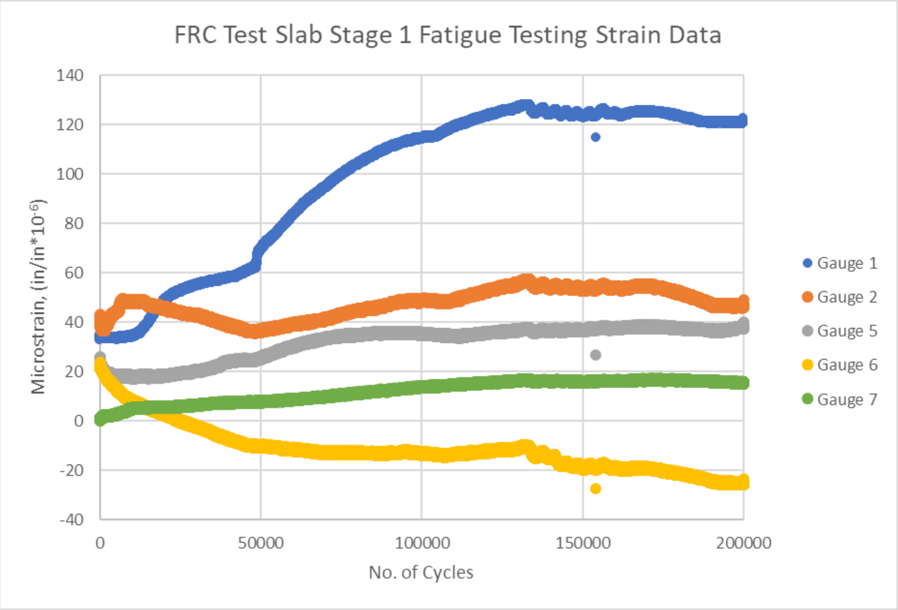

Figure 5.11 FRC Test Slab Stage 1 Fatigue Testing Strain Data

Throughout stage 2 of the testing, all the strain gauges except gauge 7 show a similar trend, which can be seen below in Figure 5.12. This is expected because gauge 7 is the only gauge perpendicular to the long dimension of the slab. The gauges recorded a steep rate of change in microstrain during the first 10,000 cycles of stage 2, after which the rate of change leveled off. Table 5.8 contains a summary of the initial and final microstrain that each gauge experienced during stages 1 and 2 of the FRC test slab fatigue testing. The measured crack width at different points during stage 3 of the fatigue testing is presented in Table 5.9.

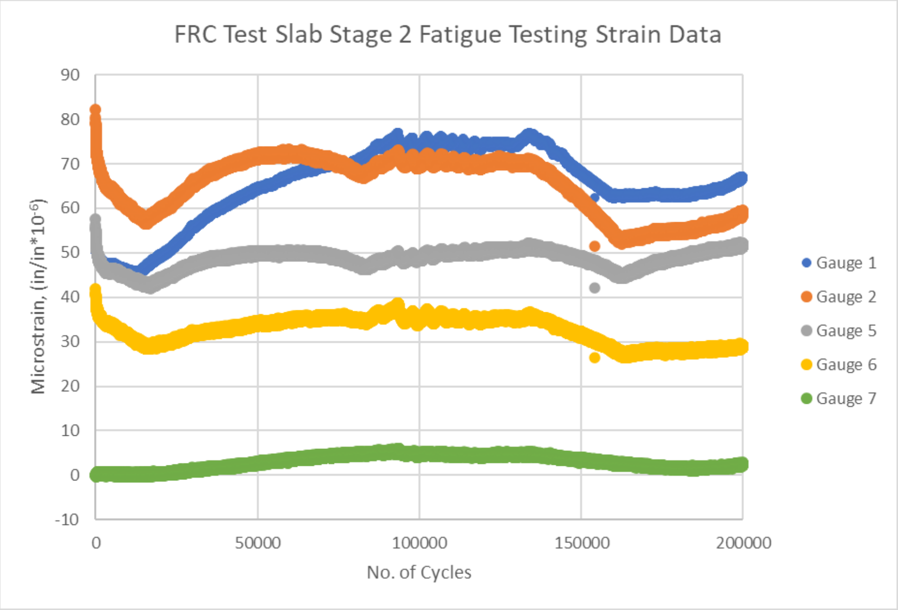

Figure 5.12 FRC Test Slab Stage 2 Fatigue Testing Strain Data

Table 5.8 FRC Slab Summary of Initial and Final Microstrains.

Measurement	**Gauge 1**	**Gauge 2**	**Gauge 5**	**Gauge 6**	**Gauge 7**
Stage 1 Initial Microstrain	32.98	43.23	25.77	23.29	0.16
Stage 1 Final Microstrain	122.73	49.28	40.09	-23.53	15.18
Stage 1 Difference in Microstrain	**89.75**	**6.05**	**14.32**	**46.81**	**15.02**
Stage 2 Initial Microstrain	53.11	82.19	57.62	41.92	-0.16
Stage 2 Final Microstrain	66.66	58.82	51.54	28.73	2.79
Stage 2 Difference in Microstrain	**13.55**	**23.37**	**6.08**	**13.18**	**2.95**

Table 5.9 FRC Slab Measured Crack Widths During Stage 3 Fatigue Testing

No. of Cycles	Measured Crack Width (in)
2,500	0.09
20,000	0.11
50,000	0.15
100,000	0.17

5.3.3 GFRP Rebar Test Slab Fatigue Testing Data

The data from stage 1 of the GFRP rebar test slab fatigue testing are shown below in Figure 5.13. The microstrain recorded by gauges 2 and 5 closely resemble each other, as do the values recorded by gauges 1 and 6. Most of the difference in microstrain recorded by all the gauges occurred within the first 50,000 cycles of stage 1 of the testing. Excluding gauge 7, the microstrain remained mostly constant after 50,000 cycles. Gauge 7 continued to record a steady increase in microstrain throughout the entirety of stage 1 of the fatigue testing.

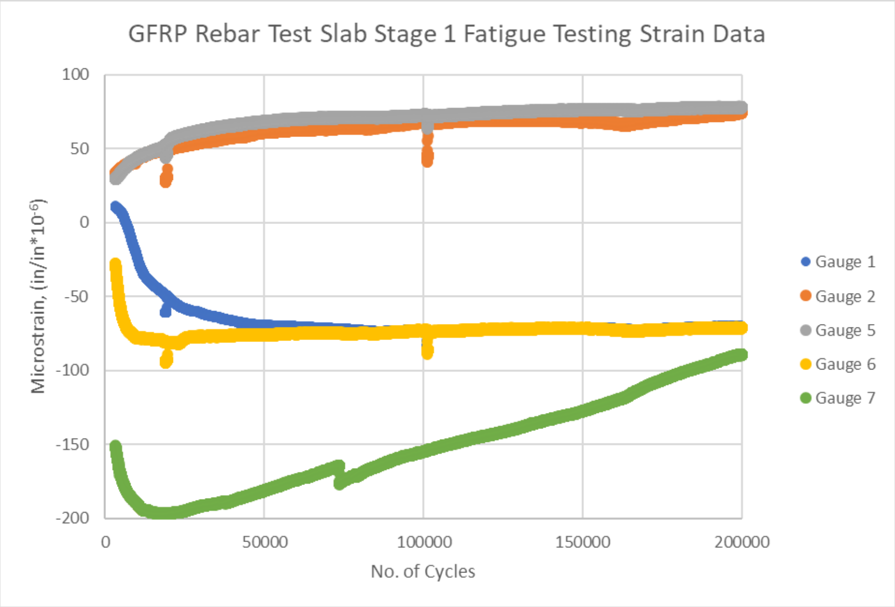

Figure 5.13 GFRP Rebar Test Slab Stage 1 Fatigue Testing Strain Data

Gauge 7 continued to record a substantial increase in microstrain during stage 2 of the testing. All the other gauges recorded consistent values with essentially no change throughout the entirety of stage 2, as shown below in Figure 5.14. Although the trends in the data from gauge 7 during both stages 1 and 2 of fatigue testing appear to be reliable, the transverse strain is not expected to be orders of magnitude larger than the longitudinal strains. Applying reasonably eccentric loads and non-symmetric support conditions to the 3D FEA model of the GFRP rebar slab was not able to replicate the transverse strains recorded during physical testing. For these reasons, the author suspects there was an internal error with the strain gauge used as gauge 7 for the GFRP rebar slab testing. Until the results can be repeated in future research, the data from gauge 7 during stages 1 and 2 of the GFRP rebar slab fatigue testing will be rejected.

A summary of the initial and final microstrain that each gauge experienced during stages 1 and 2 of the GFRP rebar test slab fatigue testing is displayed in Table 5.10. A value of "R" in the tables means the data were rejected. The measured crack width at several points during stage 3 of the fatigue testing is presented in Table 5.11.

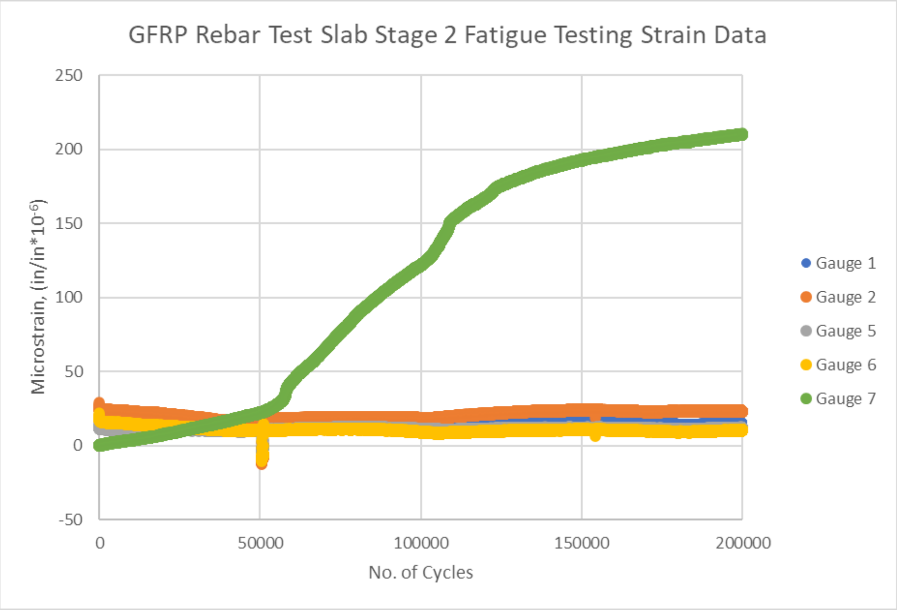

Figure 5.14 GFRP Rebar Test Slab Stage 2 Fatigue Testing Strain Data

Table 5.10 GFRP Rebar Slab Summary of Initial and Final Microstrains

Measurement	Gauge 1	Gauge 2	Gauge 5	Gauge 6	Gauge 7
Stage 1 Initial Microstrain	10.70	33.00	30.10	-27.80	-150.70
Stage 1 Final Microstrain	-70.50	74.20	78.20	-70.60	-89.20
Stage 1 Difference in Microstrain	**81.20**	**41.20**	**48.10**	**42.80**	**61.50**
Stage 2 Initial Microstrain	20.04	27.81	13.74	20.89	R (0.19)
Stage 2 Final Microstrain	14.93	23.65	11.97	10.31	R (210)
Stage 2 Difference in Microstrain	**5.11**	**4.17**	**1.77**	**10.58**	**R (210)**

Table 5.11 GFRP Rebar Slab Measured Crack Widths During Stage 3 Fatigue Testing

No. of Cycles	Measured Crack Width (in)
2,500	0.07
20,000	0.11
50,000	0.14
100,000	0.16

5.3.4 FRP Grid Test Slab Fatigue Testing Data

Similar to the other test slabs, the strain gauges that measured a notable difference in microstrain during stage 1 of the FRP grid test slab fatigue testing measured most of the difference in the first 50,000 cycles. Gauges 1 and 5 experienced relatively small changes in microstrain during stage 1. These results can be seen graphically in Figure 5-15 below. The microstrain recorded by gauges 6 and 7 leveled off after 100,000 cycles, while gauge 2's microstrain continued to steadily decrease through the end of stage 1 of the fatigue testing.

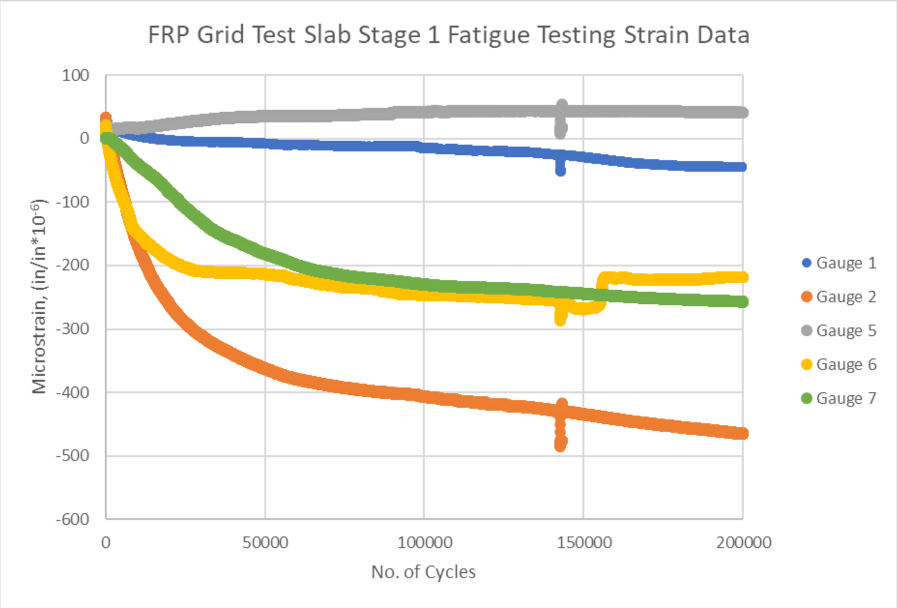

Figure 5.15 FRP Grid Test Slab Stage 1 Fatigue Testing Strain Data

Figure 5.16 shows the data obtained during stage 2 of the FRP grid test slab fatigue testing. As noted previously, only the data from the first 56,000 cycles were able to be recovered from the failed hard drive; the remainder of the data from stage 2 were lost. Repeating Stage 2 of the testing would not have produced viable results to compare with the other test slabs because the FRP grid slab would have experienced more fatigue damage prior to obtaining the results. Although the data from the final 144,000 cycles were lost, the test slab still experienced the fatigue stress from the entire 200,000 cycles of stage 2. Due to budget and schedule constraints, it was not feasible to construct a new FRP grid test slab and repeat the entire fatigue testing.

Despite losing most of the data, it can be seen that all gauges except for gauge 7 experienced a rapid change in microstrain during the initial cycles of stage 2. The first 50,000 cycles show a steady increase in microstrain for gauges 1, 2, and 5; however, the trend cannot be confirmed for the entirety of stage 2. Table 5.12 contains the initial and final microstrain that each gauge experienced during stage 1 of the fatigue testing of the FRP grid test slab. The data from stage 2 are not included in Table 5.12 because it is incomplete. Table 5.13 displays the measured crack width at different points during stage 3 of the fatigue testing.

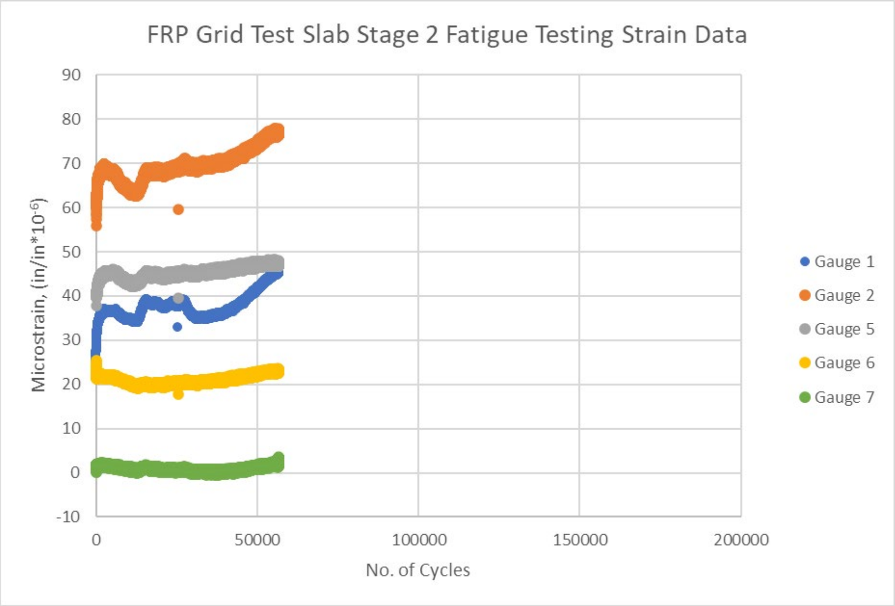

Figure 5.16 FRP Grid Test Slab Stage 2 Fatigue Testing Strain Data

Table 5.12 FRP Grid Slab Summary of Initial and Final Microstrain

Measurement	Gauge 1	Gauge 2	Gauge 5	Gauge 6	Gauge 7
Stage 1 Initial Microstrain	10.07	25.39	19.15	17.82	0.00
Stage 1 Final Microstrain	-44.97	-464.71	40.98	-218.53	-256.86
Stage 1 Difference in Microstrain	**55.03**	**490.10**	**21.83**	**236.51**	**256.86**

Table 5.13 FRP Grid Slab Measured Crack Widths During Stage 3 Fatigue Testing

No. of Cycles	Measured Crack Width (in)
2,500	0.00
20,000	0.00
50,000	0.00
100,000	0.04

5.3.5 Summary and Discussion of Fatigue Testing Data

A common trend seen in the data from the majority of the fatigue testing stages for all slabs is a large change in microstrain during the initial cycles of each stage. This trend suggests the majority of deformation due to the breakdown of the microstructure of the test slabs occurred shortly after the loading magnitude was increased. The increased load damaged the slab rapidly during its initial cycles; after which, the rate of damage drastically decreased throughout the remainder of the loading cycles. Stage 1 of the testing for the FRP grid slab showed a significant change in transverse microstrain, but the transverse microstrain is relatively constant in the available data from stage 2.

In general, the first stage of fatigue loading resulted in larger changes in microstrain than the second stage. The only accepted exception to this trend is gauge 2 on the FRC slab, which recorded larger changes in microstrain during the second stage of fatigue loading. The test slabs experienced more fatigue damage during the first 200,000 cycles than during the following 200,000 cycles even though the loading magnitude was 36% less. This trend suggests the test slabs were resilient to high cycle fatigue damage after the initial onset of structural deterioration.

Appendix B contains a figure for each strain gauge that directly compares the microstrain experienced by each alternative test slab. The figures for stage 1 of the fatigue loading are presented first and are followed by the figures for stage 2. Tables 5.14 and 5.15 directly below contain a summary of the data shown in these figures. The data in the tables are organized to directly compare the alternative test slabs. Table 5.14 shows the FRP grid slab was drastically outperformed by the other two slabs during stage 1. Although the margin between the FRC slab and GFRP rebar slab is much smaller, the FRC slab performed the best during the stage 1 fatigue loading. There is no relevant data for the FRP grid slab in Table 5.15, but the margin between the FRC slab and the GFRP rebar slab is similar to the margin in stage 1; however, the GFRP rebar slab performed the best during stage 2 of the fatigue loading excluding gauge 7.

Table 5.14 Summary of Changes in Microstrain Recorded During Stage 1 Fatigue Loading

	Test Slab Alternative	Gauge 1	Gauge 2	Gauge 5	Gauge 6	Gauge 7
Stage 1	FRC	89.75	6.05	14.32	46.81	15.02
	GFRP Rebar	81.20	41.20	48.10	42.80	61.50
	FRP Grid	55.03	490.10	21.83	236.51	256.86

Table 5.15 Summary of Changes in Microstrain Recorded During Stage 2 Fatigue Loading

	Test Slab Alternative	Gauge 1	Gauge 2	Gauge 5	Gauge 6	Gauge 7
Stage 2	FRC	13.55	23.37	6.08	13.18	2.95
	GFRP Rebar	5.11	4.17	1.77	10.58	R (210)
	FRP Grid	NA	NA	NA	NA	NA

Due to debonding of several strain gauges for various reasons during stage 3 of the fatigue loading, the alternatives were analyzed using measured cracks widths at several points during stage 3. The crack widths in the test slabs were considered important for two main reasons. First, crack growth is representative of the accumulation of fatigue damage in reinforced concrete. Larger cracks in the concrete matrix indicate the reinforcement was less effective in reducing the fatigue stress experienced in the concrete matrix. And second, concrete pavement slabs must protect their embedded IPTS for their entire service lives to be considered a viable option. Large cracks allow water and deicing chemicals to be introduced to the IPTS, which is detrimental to the health of the electronic system.

Table 5.16 displays the measured crack widths below. The crack width for the FRP grid slab is reported as 0.00 in for the first three measurements because no apparent crack was visible. Because of its delayed cracking and much smaller final crack width at the end of stage 3, the FRP grid slab clearly performed the best under the heavy cyclic loading of stage 3 fatigue testing. The results from the FRC slab and the GFRP rebar slab are very similar, but the GFRP rebar slab had a slightly smaller crack width.

Table 5.16 Summary of Crack Widths (in) Measured During Stage 3 Fatigue Loading

	Test Slab Alternative	2,500 Cycles	20,000 Cycles	50,000 Cycles	100,000 Cycles
Stage 3	FRC	0.09	0.11	0.15	0.17
	GFRP Rebar	0.07	0.11	0.14	0.16
	FRP Grid	0.00	0.00	0.00	0.04

It is anticipated that full-scale specimens would experience smaller crack widths than the concrete test slabs in this study. The loading applied in this study produced an equal amount of stress in the extreme tensile fiber of the test slabs as would be expected for a full-scale specimen under the typical design axle load of 32 kips (AASHTO, 2018a). The wheel loads applied to the test slabs in this study had a spacing of three feet between them, while a full-scale specimen would have a spacing of six feet between the wheel loads. This means the test slabs experienced the same amount of subgrade deflection and tensile stress over a smaller arc length. The larger arc length of a full-scale specimen theoretically should reduce the magnitude of cracking in the tensile face of the concrete pavement slabs.

Table 5.17 has been created to help quantify the performance of each alternative test slab during each stage of the fatigue testing. Each alternative was assigned a score between 0 and 10 for each stage of testing based on the measured data. A score of 10 represents the maximum combined microstrain or maximum combined crack width for any given alternative during the given stage of testing. The other alternatives' scores were based on the percentage of the maximum that their combined data equaled; therefore, a lower score represents better performance. In the case of rejected data, the values from the other alternative slabs were averaged and used as placeholders to allow for a quantifiable comparison between the alternatives. An asterisk in Table 5.17 indicates the values were calculated based on an averaged value that was used to replace rejected data.

Table 5.17 Relative Score of Each Test Slab for Each Stage of Fatigue Loading

Fatigue Testing Stage	FRC Slab	GFRP Rebar Slab	FRP Grid Slab
1	1.62	2.59	10.00
2	10.00*	4.16*	NA
3	10.00	9.23	0.77

5.4 Ultimate Strength Analysis Results

For the ultimate strength analysis, each test slab was subjected to a monotonic load to the point of complete failure after the fatigue testing protocol was complete. The ultimate strength of the control slab was evaluated even though the source of its flexural crack at midspan was different from the other test slabs. Appendix B contains figures that show the force vs. time curve for each test slab. Figures 5.17 through 5.20 below show the force vs. displacement curves for each alternative. The displacement was a measurement of the extension of the hydraulic actuator. The sharpness in decline of loading after the peak load for each alternative is representative of the stiffness of the slab at failure. A sudden and sharp decline, as seen in the control slab, GFRP rebar slab, and FRP grid slab, represents a sudden and brittle failure. The gradual decrease in applied load seen in the FRC slab is representative of a ductile failure.

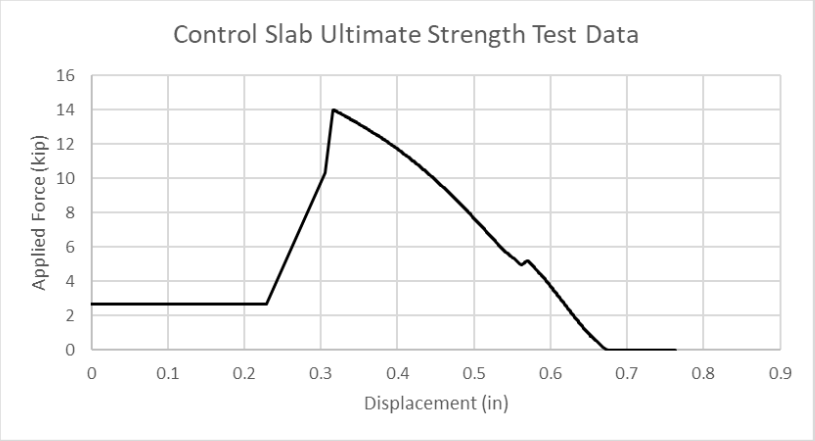

Figure 5.17 Control Slab Ultimate Strength Test Data

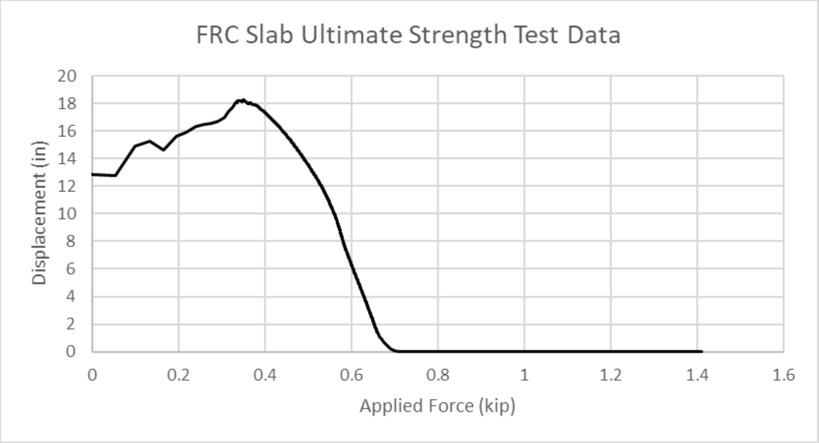

Figure 5.18 FRC Slab Ultimate Strength Test Data

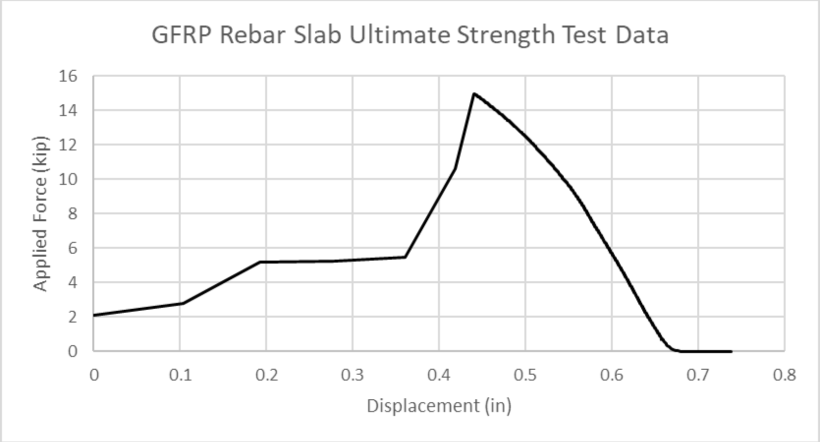

Figure 5.19 GFRP Rebar Slab Ultimate Strength Test Data

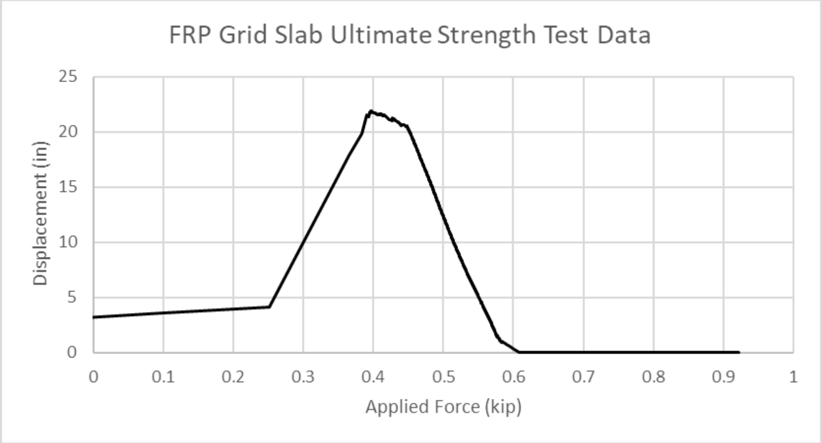

Figure 5.20 FRP Grid Slab Ultimate Strength Test Data

Figures 5.21 through 5.24 each contain an image of a test slab after failure due to the ultimate strength testing. The figures show the control slab, GFRP rebar slab, and FRP grid slab all experienced a failure plane along the transverse section of the Litz wire. The failure plane of the FRC slab seen in Figure 5.22 is the only failure that exhibited delamination of the concrete cover between the top of the slab and the mock IPTS. Figures 5.23 and 5.24 show the GFRP rebar and the FRP grid each failed in rupture in their respective test slabs; the residual bond strength between the concrete matrix and the reinforcing was not the governing factor. On the other hand, the fibers in the FRC test slab failed through the pullout mechanism. The bond strength between the concrete matrix and the macrofibers was weaker than the macrofibers themselves. Figures 5.21 through 5.24 have all been rotated so the top of the test slab is at the top of the figure.

Figure 5.21 Control Slab Exposed Failure Plane

Figure 5.22 FRC Slab Exposed Failure Plane

Figure 5.23 GFRP Rebar Slab Exposed Failure Plane

Figure 5.24 FRP Grid Slab Exposed Failure Plane

Table 5.18 contains a summary of the ultimate residual strengths of each test slab. As expected, the failure load of the control slab is the lowest at 13.99 kips. The failure load of the FRC slab increased by 31% compared with the control slab, and the FRP grid slab increased by 56%. Surprisingly, the failure load of the GFRP rebar slab only increased by 7%. A much larger increase in the residual strength was expected by comparing the pre-fatigue expected ultimate strengths of the GFRP rebar slab and the control slab; this will be further discussed later in this chapter. The deflection at failure is also shown below in Table 5.18. The GFRP rebar and FRP grid slabs both exhibited similar stiff behavior compared with the other test slabs. The FRP grid slab was slightly stiffer than the GFRP rebar slab. The FRC slab and the control slab exhibited similar amounts of deflection at failure. Similar to the concept explained in Section 5.3.5, it is anticipated that full-scale specimens would allow for more deflection before failure due to their longer arc length between the loading supports.

Table 5.18 Summary of Ultimate Residual Strengths

Test Slab Alternative	Failure Load (kip)	Deflection at Failure (in)
Control	13.99	0.356
FRC	18.27	0.351
GFRP Rebar	14.99	0.234
FRP Grid	21.85	0.212

5.5 3D Finite Element Analysis Results

ANSYS Workbench 2021 R2 software was used to create a 3D FEA model of each test slab. The FEA models were used to estimate the expected ultimate strength of each test slab prior to experiencing fatigue damage. Figures 5.25 through 5.28 show screenshots of the models after being analyzed by the software. The colors in the figures represent the factor of safety (FS) with respect to applied stress over maximum allowable stress experienced by the model components. The red color represents an FS of 1.0, and the remaining colors follow a typical scale. The figures for the control and FRC slabs show the stress FS in the concrete because there is no discrete tensile reinforcement. The concrete is hidden for the GFRP rebar and FRP grid slabs to allow the tensile reinforcement to be seen because the ultimate tensile failure is governed by the discrete reinforcement. All slabs are shown with the tension face upwards in the figures because this orientation better suits the lighting and visualization of the software program.

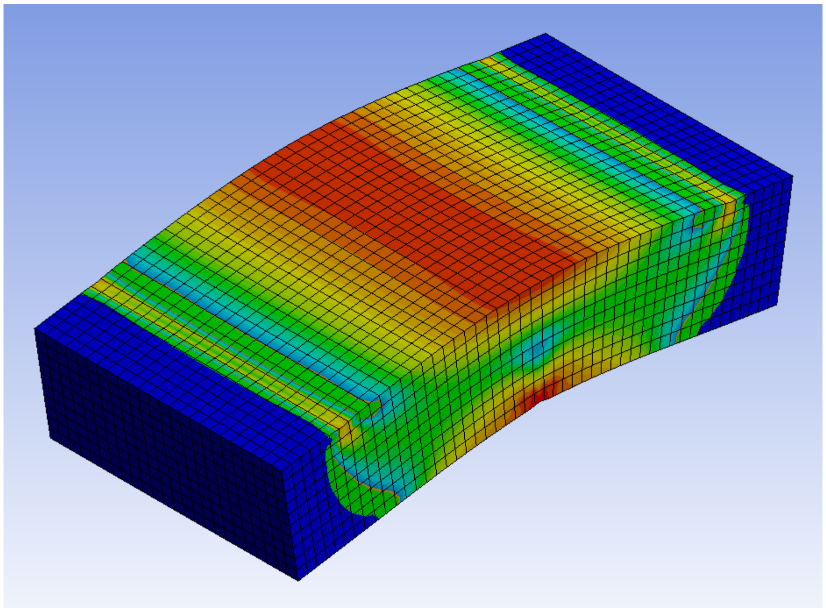

Figure 5.25 Control Slab FEA Model Applied Stress FS

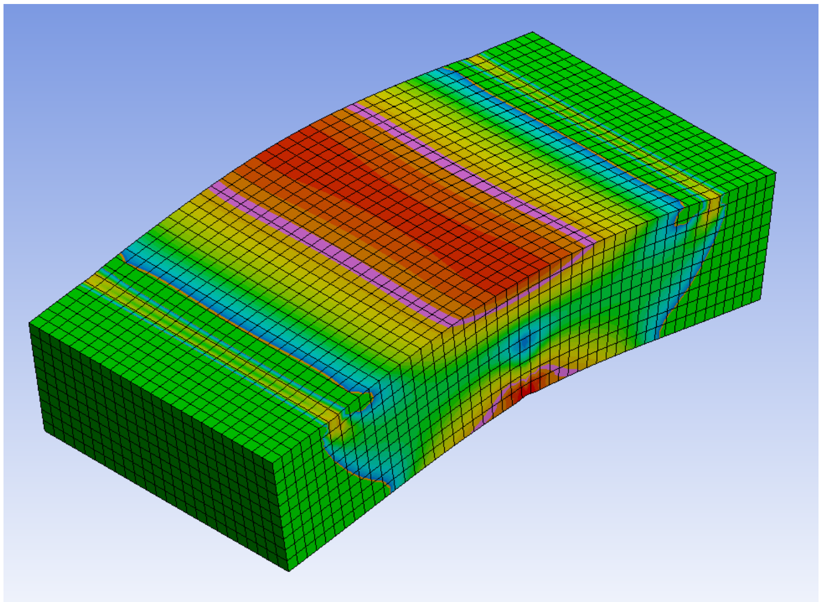

Figure 5.26 FRC Slab FEA Model Applied Stress FS

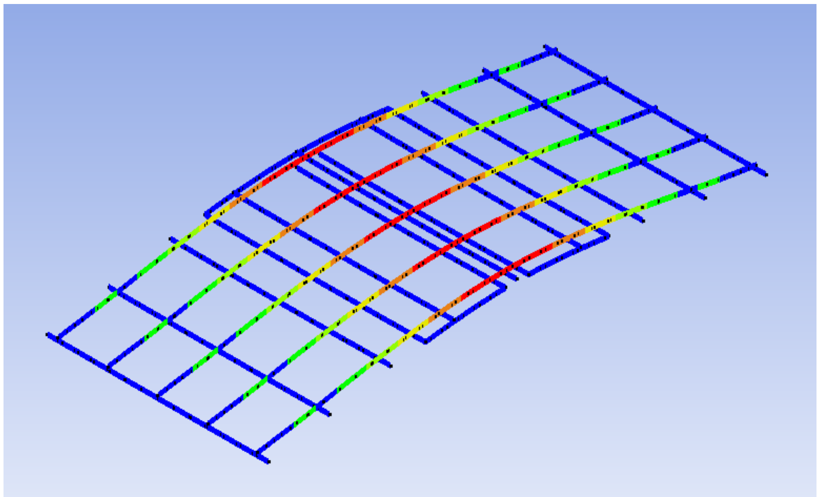

Figure 5.27 GFRP Rebar Slab FEA Model Applied Stress FS

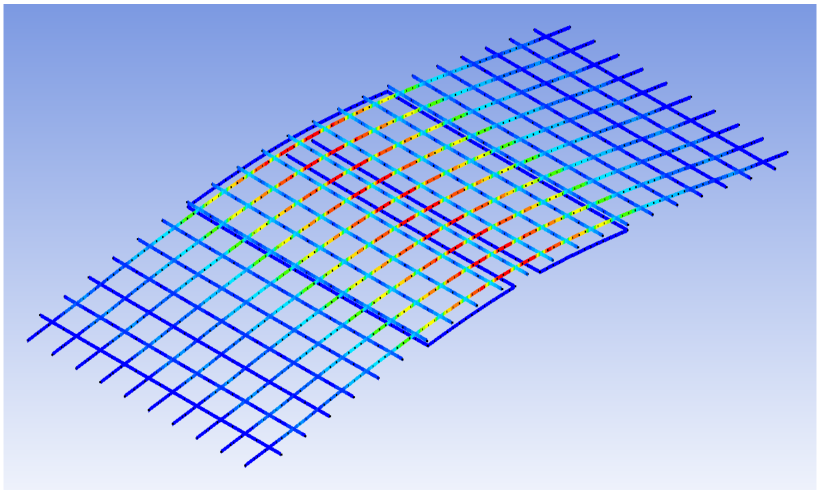

Figure 5.28 FRP Grid Slab FEA Model Applied Stress FS

The expected failure load for every test slab obtained from the 3D FEA models is higher than the measured values obtained by physical testing during this research. Because the FEA models do not account for any damage accumulated during the fatigue testing process, it is expected their results for the ultimate strength of the test slabs are higher than the results from testing the physical slabs after the fatigue process. The difference between the load required to cause ultimate failure in the FEA models and the load required to cause ultimate failure in the physical test slabs corresponds to the loss of residual structural strength incurred during the fatigue testing process. Completely associating the difference between failure loads inherently assumes the FEA models perfectly represent the in-situ conditions during physical testing and the actual construction of the physical test slabs. The author recognizes these assumptions are not completely accurate but does not attempt to quantify their inaccuracy.

Table 5.19 displays a summary of the expected failure loads for each test slab obtained from the 3D FEA models. The table also quantifies the difference between the expected failure loads per the model and the measured failure loads during testing using Equation 5.5. Excluding the GFRP rebar slab, the percentage of strength reduction varies between 15.5% and 24.6%; these results agree well with the results from the physical test slabs. The GFRP rebar slab stands as an outlier with a reduction in strength of 59.2%. The physical test slab did not show any debonding between the GFRP rebar and the concrete matrix, but it is important to note that the "bond strength" of FRP reinforcement includes the bond between the individual fibers and the resin that composes each bar. The degradation of the resin and fiber connection within the GFRP bars is a possible component of this large reduction in residual strength. Other possibilities that may have contributed to this reduction are a weak batch of GFRP rebars from the manufacturing plant, additional damage to the slab inflicted during transportation and testing setup for the slab, and/or workmanship errors during the construction of the test slab.

$$Meaured\ Strength\ Reduction = \frac{P_{model} - P_{physical}}{P_{model}} \tag{5.5}$$

Where:

- P_{model} = Expected failure load predicted by FEA model, kips
- $P_{physical}$ = Measured failure load during physical testing, kips

Table 5.19 Summary of Failure Loads from FEA Analysis

Test Slab Alternative	Failure Load in Model (kip)	Failure Load of Physical Slab (kip)	Measured Strength Reduction (%)
Control	16.56	13.99	15.5
FRC	24.24	18.27	24.6
GFRP Rebar	36.72	14.99	59.2
FRP Grid	27.60	21.85	20.8

6. CONCLUSIONS

Embedding IPTS in concrete pavement slabs is one possible solution to the charging issues associated with EVs. Structural voids within the concrete slabs are created by the electronic equipment required for the IPTS. These voids weaken the panels and create areas of concentrated stress. Another structural issue introduced by the IPTS is related to the magnetic fields and large amounts of heat they generate. Due to the magnetism and heat, traditional metallic reinforcing is not effective in the upper portions of the concrete slabs. The purpose of this research is to investigate several alternatives for top mat reinforcing in concrete pavement slabs with embedded IPTS to ensure the durability and resiliency of the pavement throughout its service life.

Four test slabs with different reinforcing alternatives were constructed and tested in this research. The reinforcing alternatives included a control slab with no top mat reinforcing, an FRC slab with no discrete reinforcing, a slab with GFRP rebar in the top mat, and a slab with an FRP grid used as the top mat reinforcement. Three of the slabs, excluding the control slab, were subjected to 500,000 cycles of fatigue loading in three different loading stages. After the fatigue testing, all four of the test slabs experienced a monotonic load until failure to determine their ultimate residual strength. A 3D FEA model of each slab was created to estimate their ultimate strengths prior to the fatigue damage accumulated during fatigue testing. Based on the testing results, the following conclusions can be made about the previously mentioned top mat reinforcement alternatives for concrete pavement slabs with embedded IPTS:

- If possible, future iterations of the IPTS should avoid placing Litz wire transverse to the long dimension of the slab near the midpoint of the slab.
- An FRC mix with synthetic macrofibers can achieve the required flowability to successfully be used in a pavement slab with the many irregularities created by an embedded IPTS.
- Even a grid structure with clear openings as small as two inches used as the top mat reinforcement will allow for sufficient bonding of the concrete matrix so as to not produce spalling of the concrete cover.
- All the tested alternatives withstood 400,000 cycles of fatigue loading at or above the AASHTO prescribed design magnitude while showing no signs of failure. This indicates each reinforcement alternative is likely a viable option.
- The AASHTO prescribed design level loading magnitude used in stage 1 of the fatigue loading induced as much or more strain in the discontinuities at the ends of the mock IPTS as was induced at the midpoint of the test slabs.
- The majority of the fatigue damage due to the breakdown of the microstructure of the test slabs occurred shortly after the loading magnitude was increased each time it was increased.
- In general, the recorded microstrains indicate the test slabs experienced more fatigue damage during the first 200,000 cycles than during the following 200,000 cycles even though the loading magnitude was 36% less. This suggests the reinforcement alternatives were resilient to high cycle fatigue damage after the initial onset of structural deterioration.
- The FRC slab and the GFRP rebar slab drastically outperformed the FRP grid slab during stage 1 of the fatigue testing.
- The GFRP rebar slab performed better than the FRP grid slab during stage 2 of the fatigue testing except for data recorded by gauge 7, which were rejected.

- The FRC slab and the GFRP rebar slab were both exceptionally outperformed by the FRP grid slab during stage 3 of the fatigue testing.
- Due to its relatively delayed crack formation and small crack width, the FRP grid slab performed the best throughout the entirety of the fatigue testing.
- The FRC slab exhibited a relatively ductile failure at its ultimate residual strength compared with the other test slabs.
- The control slab, GFRP rebar slab, and FRP grid slab all experienced an ultimate failure plane along the discontinuity created by the transverse section of the Litz wire.
- The residual bond strength between the concrete matrix and the discrete reinforcing (GFRP rebar and FRP grid) was not the governing factor during the ultimate strength testing.
- In the FRC slab, the ultimate residual strength failure mechanism was fiber pullout rather than fiber rupture.
- The 3D FEA models indicate the control slab, FRC slab, and FRP grid slab all experienced between 15.5% and 24.6% loss of strength between their anticipated ultimate strength and their tested residual ultimate strength.
- The 3D FEA model for the GFRP rebar slab indicates a 59.2% loss of strength between its anticipated ultimate strength and its tested residual ultimate strength.

The Sika Fibermesh-650 synthetic macrofibers were chosen as the fibers for the FRC alternative in this research due to their availability and affordability. When considering large scale production of concrete pavement panels with embedded IPTS, these factors are important. More alternative fibers should be investigated to verify their performance in FRC concrete pavement slabs with embedded IPTS. The alternative fibers should vary in type and geometry, including surface deformations to increase the bond strength to the concrete. An economic analysis should accompany the performance analysis to ensure the tested fibers are practical.

Future research should seek to verify the testing results and conclusions in this experiment. A common number of specimens used by ASTM to ensure validity of testing results is three specimens. Therefore, future research should seek to test at least three specimens for each alternative to verify the accuracy of the testing results. In addition, full-scale slabs should eventually be tested to verify that the size effects of the specimens do not introduce any unforeseen results between the scaled test specimens and the full-scale slabs. The full-scale slabs should be tested on various support conditions that are recommended by different state transportation departments to investigate the effects that different subgrade moduli have on the pavement slabs. Future researchers should also use robust data acquisition and recording equipment to avoid the loss of any data due to equipment failure.

More grid structures should be tested as alternative tensile reinforcement. Grids made of different materials and with different geometric properties may be tested. A geosynthetic grid with as much stiffness as possible would be a good candidate for future testing.

REFERENCES

AASHTO. (2018a). "AASHTO LRFD Bridge Design Specifications." *American Association of State Highway and Transportation Officials*, Washington, DC.

AASHTO. (2018b). "AASHTO LRFD Bridge Design Guide Specifications for GFRP-Reinforced Concrete." *American Association of State Highway and Transportation Officials*, Washington, DC.

ACI 318. (2019). "ACI 318-19: Building Code Requirements for Structural Concrete." *American Concrete Institute*

ACI Committee 440. (2015). "ACI 440.1R-15: Guide for the Design and Construction of Concrete Reinforced with FRP Bars." *American Concrete Institute*.

ACI Committee 544. (1996). "ACI 544.1R-96: Report on Fiber Reinforced Concrete." *American Concrete Institute*.

ACI Committee 544. (2018). "ACI 544.4R-18: Guide to Design with Fiber-Reinforced Concrete." *American Concrete Institute*.

Altoubat, S., Yazdanbakhsh, A., and Rieder, K. A. (2009). "Shear Behavior of Macro-Synthetic Fiber-Reinforced Concrete Beams without Stirrups," *ACI Materials Journal*, 106 (4), pp. 381-389.

Angst, U., et al. (2012). "Concrete Cover Cracking Owing to Reinforcement Corrosion - Theoretical Considerations and Practical Experience." *Materials and Corrosion*. 63 (12), pp. 1069–1077., https://doi.org/10.1002/maco.201206669.

Aristorenas, G., and Gomez, J. (2014). "Subgrade Modulus – Revisited." *Structure Magazine*, pp. 9-11.

ASTM C1609/C1609M. (2012). "Standard Test Method for Flexural Performance of Fiber-Reinforced Concrete (Using Beam with Third-Point Loading)." *American Society for Testing and Materials.*

ASTM C31. (2019). "Standard Practice for Making and Curing Concrete Test Specimens in the Field." *American Society for Testing and Materials.*

ASTM C39. (2012). "Standard Test Method for Compressive Strength of Cylindrical Concrete Specimens." *American Society for Testing and Materials.*

ASTM C496. (2017). "Standard Test Method for Splitting Tensile Strength of Cylindrical Concrete Specimens." *American Society for Testing and Materials.*

Bae, Sungjin, and Oguzhan Bayrak. (2003). "Early Cover Spalling in High-Strength Concrete Columns." *Journal of Structural Engineering*, 129 (3), pp. 314–323., https://doi.org/10.1061/(asce)0733-9445(2003)129:3(314).

Balaguru, P. N., and Ramakrishnan, V. (1986). "Freeze-Thaw Durability of Fiber Reinforced Concrete," *ACI Journal Proceedings*, 83 (3), pp. 374-382.

Batson, G., Bailey, L., Landers, E., Hooks, J., and Ball, C. (1972). "Flexural Fatigue Strength of Steel Fiber Reinforced Concrete Beams." *Journal Proceedings.* 69(11). https://doi.org/10.14359/11275

Berman N. Roadway vehicle: U.S. Patent 4,129,203. 1978-12-12.

Biggs, A., Bowen, D. H., and Kollek, J. (1974). *Proceedings of the 2nd International Carbon Fibre Conference*, The Plastics Institute, London.

Blocher, Ewald. (n.d.). “On the Road with Electric Power: From the Trolleybus to the Ehighway.” *Siemens.com Global Website.* Accessed September 12, 2021. https://www.siemens.com/global/en/company/about/history/stories/on-the-road-with-electric-power.html.

Bonakdar, A., Bakhshi, M., Shekarchi, M., and Pinto, J. (2005). “Study of Load-Deflection Response and Flexural Toughness Parameters of SFRC with Center Point Loading.” *Proceeding of 3rd International Structural Engineering and Construction Conference.*” pp. 65-72.

Boys, Green. U.S. Patent 5,293,308. 1991.

Campbell Scientific. (n.d.). “CR3000 – Measurement and Control Datalogger.” CR3000: Measurement and Control Datalogger. https://www.campbellsci.com/cr3000.

Carvelli, V., Pisani, M. A., and Poggi, C. (2010). “Fatigue Behaviour of Concrete Bridge Deck Slabs Reinforced with GFRP Bars.” *Composites Part B: Engineering*, 41 (7), pp. 560–567.

Chen, Airong, et al. (2016). “Mesoscopic Simulation of Steel Rebar Corrosion Process in Concrete and Its Damage to Concrete Cover.” *Structure and Infrastructure Engineering*. 13 (4), pp. 478–493., https://doi.org/10.1080/15732479.2016.1164730.

Chen, F., Taylor, N., and Kringos, N. (2015). “Electrification of Roads: Opportunities and Challenges.” *Applied Energy*, 150 (15), pp. 109–119. https://doi.org/10.1016/j.apenergy.2015.03.067

Covic, G. A., and Boys, J. T. (2013). “Inductive Power Transfer.” *Proceedings of the IEEE*, 101 (6), pp. 1276–1289. https://doi.org/10.1109/JPROC.2013.2244536

Demers, C. E. (1998). “Tension–Tension Axial Fatigue of E-Glass Fiber-Reinforced Polymeric Composites: Fatigue Life Diagram.” *Construction and Building Materials*, 12 (5), pp. 303–310. https://doi.org/https://doi.org/10.1016/S0950-0618(98)00007-5

El-Hanafy, Ahmed M., et al. (2022). “Behavior of Concrete Slabs Reinforced by Different Geosynthetic Materials.” *HBRC Journal*, 18 (1), pp. 107–121., https://doi.org/10.1080/16874048.2022.2097363.

El-Nemr, Amr, et al. (2013). “Flexural Behavior and Serviceability of Normal- and High-Strength Concrete Beams Reinforced with Glass Fiber-Reinforced Polymer Bars.” *ACI Structural Journal*, 110 (06), https://doi.org/10.14359/51686162.

El-Ragaby, A., El-Salakawy, E., and Benmokrane, B. (2007). “Fatigue Life Evaluation of Concrete Bridge Deck Slabs Reinforced with Glass FRP Composite Bars.” *Journal of Composites for Construction*, 11 (3), pp. 258–268. https://doi.org/10.1061/(ASCE)1090-0268(2007)11:3(258)

EN 14651. (2005). “Test Method for Metallic Fibre Concrete – Measuring the Flexural Tensile Strength.” *European Standard.*

Erdem, Savas, et al. (2015). “Investigation of Bond between Fibre Reinforced Polymer (FRP) Composites Rebar and Aramid Fibre-Reinforced Concrete.” *International Journal of Composite Materials*, 5 (6), pp. 148–154. https://doi.org/10.5923/j.cmaterials.20150506.02.

Falk, M. S. (1904). “Cements, mortars and concretes: their physical properties.” *Clark*.

FHWA. (2019). “Compilation of Existing State Truck Size and Weight Limit Laws – Appendix A.” Accessed March 10, 2020. https://ops.fhwa.dot.gov/freight/policy/rpt_congress/truck_sw_laws/app_a.htm.

Foster, Stephen J. (2001). “On Behavior of High-Strength Concrete Columns: Cover Spalling, Steel Fibers, and Ductility.” *ACI Structural Journal*, 98 (4), pp. 583–589.

Gardner, Trevor, (2017). “Wireless Power Transfer Roadway Integration.” All Graduate Theses and Dissertations. 6866. https://digitalcommons.usu.edu/etd/6866

Gopalaratnam, V. S., Meyer, J., De Young, K., Belarbi, A., and Wang, H. (2006). “Steel-free hybrid reinforcement system for concrete bridge decks, phase 1.” *Missouri. Dept. of Transportation*.

Hadi, Muhammad N.S., and Hua Zhao. (2011). “Experimental Study of High-Strength Concrete Columns Confined with Different Types of Mesh under Eccentric and Concentric Loads.” *Journal of Materials in Civil Engineering*, 23 (6), pp. 823-832. EBSCOhost, doi:10.1061/(ASCE)MT.1943-5533.0000234.

Hillerborg, A. (1985). “The Theoretical Basis of a Method to Determine the Fracture Energy GF of Concrete.” *Materials and Structures*, 18 (4), pp. 291-296. doi: 10.1007/BF02472919

Hutin, M., and Leblang M. Transformer system for electric railways: U.S. Patent 527,857. 1984-10-23.

Hsu, T. T. C. (1981). “Fatigue of Plain Concrete.” *Journal Proceedings*, 78 (4), pp. 292–305.

Hwan, Byung. (1986). “Fatigue Analysis of Plain Concrete in Flexure.” *Journal of Structural Engineering*, 112 (2), pp. 273-288.

Jabbar, Shahad AbdulAdheem, and Saad B.H. Farid. (2018). “Replacement of Steel Rebars by GFRP Rebars in the Concrete Structures.” *Karbala International Journal of Modern Science*, 4 (2), pp. 216–227. https://doi.org/10.1016/j.kijoms.2018.02.002.

Jain, Shailendra, and Kumar, Lalit (2018). “31 - Fundamentals of Power Electronics Controlled Electric Propulsion.” Power Electronics Handbook (Fourth Edition), *Butterworth-Heinemann*, pp. 1023-1065. ISBN 9780128114070, https://doi.org/10.1016/B978-0-12-811407-0.00035-0.

Johnston, C. D., and Zemp, R. W. (1991). “Flexural Fatigue Performance of Steel Fiber Reinforced Concrete--Influence of Fiber Content, Aspect Ratio, and Type.” *Materials Journal*, 88 (4). https://doi.org/10.14359/1875

Katz, A. (1998). “Effect of Helical Wrapping on Fatigue Resistance of GFRP.” *Journal of Composites for Construction*, 2 (3), pp. 121-125.

Kemp, Michael, and David Blowes. (2011). “Concrete Reinforcement and Glass Fibre Reinforced Polymer.” *Queensland Roads,* 11, pp. 40-48.

Klowak, C., Memon, A., and Mufti, A. (2006). “Static and Fatigue Investigation of Second Generation Steel-Free Bridge Decks.” *Cement and Concrete Composites*, 28 (10), pp. 890–897.

Kumar, Sanjeev V., and Hota V. GangaRao. (1998). “Fatigue Response of Concrete Decks Reinforced with FRP Rebars.” *Journal of Structural Engineering*, 124 (1), pp. 11–16. https://doi.org/10.1061/(asce)0733-9445(1998)124:1(11).

Lee, M. K., and Barr, B. I. G. (2004). “An Overview of the Fatigue Behaviour of Plain and Fibre Reinforced Concrete.” *Cement and Concrete Composites*, 26 (4), pp. 299–305. https://doi.org/https://doi.org/10.1016/S0958-9465(02)00139-7

Li, Ye, et al. (2019). “Synergistic Effects of Hybrid Polypropylene and Steel Fibers on Explosive Spalling Prevention of Ultra-High Performance Concrete at Elevated Temperature.” *Cement and Concrete Composites*, 96, pp. 174–181. https://doi.org/10.1016/j.cemconcomp.2018.11.009.

Liu, Jin-Cheng, et al. (2018) “A New Perspective on Nature of Fire-Induced Spalling in Concrete.” *Construction and Building Materials*, 184, pp. 581–590. https://doi.org/10.1016/j.conbuildmat.2018.06.204.

Majumder, Subhrasmita, and Saha, Showmen. (2021) “Shear Behaviour of RC Beams Strengthened Using Geosynthetic Materials by External and Internal Confinement.” *Structures*, 32, pp. 1665–1678. https://doi.org/10.1016/j.istruc.2021.03.107.

Mallick, P. K. (1988) “Fiber Reinforced Composites, Materials, Manufacturing, and Design.” *Marcell Dekker, Inc*., pp. 469.

Mandell, J. F. (1982) “Fatigue Behavior of Fiber-Resin Composites.” *Developments in Reinforced Plastics, Applied Science Publishers*, 2, pp. 67-107.

McRory, Jared W. (2020) “Experimental Static and Cyclic Behavior of Hybrid Non-Metallic Bridge Decks Reinforced with Discrete GFRP Rebar and GFRP Macrofiber.” All Graduate Theses and Dissertations. 7790. https://digitalcommons.usu.edu/etd/7790

Mu, B., C. Meyer, and S. Shimanovich. (2002) “Improving the Interface Bond Between Fiber Mesh and Cementitious Matrix,” *Cement and Concrete Research*, 32 (5), pp. 783-787. https://doi.org/10.1016/S0008-8846(02)00715-9.

Nanni, A. (1992). “Properties of Aramid Fiber Reinforced Concrete and SIFCON.” *J. of Materials in Civil Engineering*, 2 (1), pp. 1-15.

Nordby, G. M. (1958). “Fatigue of Concrete - A Review of Research.” *Journal Proceedings*, 55 (8). https://doi.org/10.14359/11349

Nguyen, Chung Thi, et al. (2016). “Mechanical Properties of Aramid Fiber Reinforced Concrete.” *The 21st National Convention on Civil Engineering*.

O’Neil, E. F. (1978). “Ultimate Strength of Fiber-Reinforced Concrete under Cyclic, Flexural Loading.” Army Engineer Waterways Experiment Station, Vicksburg, Miss.

PATH. (1994) “Roadway powered electric vehicle project track construction and testing program phase 3D.” *Systems Control Technology, Inc*., California PATH research paper UCB-ITS-PRR 94-07, 10551425

Porter, M. L., Hughes, B. W., Barnes, B. A., and Viswanath, K. P., (1993) “Non-Corrosive Tie Reinforcing and Dowel Bars for Highway Pavement Slabs.” *Report No. HR-343*, Iowa Highway Research Board and Iowa Department of Transportation.

Raine, Nathan J. (2022). “Long Term Feasibility of Inductive Power Transfer Systems Embedded in Concrete Pavement Panels.” All Graduate Theses and Dissertations. 8457. https://digitalcommons.usu.edu/etd/8457

Raithby, K. D. (1979). “Flexural Fatigue Behaviour of Plain Concrete.” *Fatigue of Engineering Materials and Structures, 2.*

Raithby, K. D., and Whiffin, A. C. (1968). “Failure of Plain Concrete Under Fatigue Loading - A Review of Current Knowledge.”

RajeshKumar, K., et al. (2021) “Structural Performance of Biaxial Geogrid Reinforced Concrete Slab.” *International Journal of Civil Engineering*, 20 (3), pp. 349–359. https://doi.org/10.1007/s40999-021-00668-y.

Ramakrishnan, V., Wu, G. Y., and Hosalli, G. (1989). “Flexural Fatigue Strength of Fiber Reinforced Concrete, Endurance Limit and Impact Strength.” *Transportation Research Record No, 1226*, 17.

Roesler, J.R. (2006). “Fatigue Resistance of Concrete Pavements.” *6th International DUT–Workshop on Fundamental Modelling of Design and Performance of Concrete Pavements*.

Schutz, W. (1996). “A history of fatigue.” *Engineering Fracture Mechanics*, 54 (2), pp. 263–300. https://doi.org/https://doi.org/10.1016/0013-7944(95)00178-6

Seki, H., Sekijima, K., and Konno, T. (1997). “Test Method on Creep of Continuous Fiber Reinforcing Materials.” *Proceedings of the Third International Symposium on Non-Metallic (FRP) Reinforcement for Concrete Structures (FRPRCS-3)*, 2, pp. 195-202.

Sivagamasundari, R., and Kumaran, G. (2008). “A Comparative Study on the Flexural Behaviour of One-Way Concrete Slabs Reinforced with GFRP Reinforcements and Conventional Reinforcements when Subjected to Monotonic and Repeated Loading.” *Open Civil Engineering Journal*, 2, pp. 24–34.

Sonoda, K., and Horikawa, T. (1982). “Fatigue Strength of Reinforced Concrete Slabs Under Moving Loads.” *Fatigue of Steel and Concrete Structures*, pp. 455–462.

Tabatabaei, Zahra S., et al. (2013). “Experimental and Numerical Analyses of Long Carbon Fiber Reinforced Concrete Panels Exposed to Blast Loading.” *International Journal of Impact Engineering*, 57, pp. 70–80. https://doi.org/10.1016/j.ijimpeng.2013.01.006.

Talboys, L. N., and Lubell, A. S. (2014) “Shear in SFRC Slabs Reinforced with High-Strength Steel.” *ACI Structural Journal*, 111 (6), pp. 1431-1440. doi: 10.14359/51687103

Terzaghi, K. (1955). “Evaluation of Coefficient of Subgrade Reaction." *Geotechnique*, 5 (4), pp. 297-326.

Van Ornum, J. L. (1903). “The Fatigue of Cement Products.” *Proceedings of the American Society of Civil Engineers*, 29 (6), pp. 627–629. ASCE.

Vandewalle, L. (2003). “Test and Design Methods for Steel Fiber Reinforced Concrete – σ-ε Design Method – Final Recommendation.” *Materials and Structures*, 36 (262), pp. 560-567. doi: 10.1617/14007

Walker, W., and Holland, J. (2016). “Modulus of Subgrade Reaction – Which One Should be Used?” *Structural Services Engineering Bulletin*.

Wang, Lei, et al. (2022). “Cracks Width Prediction of Steel-FRP Bars Reinforced High-Strength Composite Concrete Beams.” *Structures*, 43, pp. 424–433. https://doi.org/10.1016/j.istruc.2022.06.064.

Wei, S., Yun, Y., and Jianming, G. (1996). “Study of the Fatigue Performance and Damage Mechanism of Steel Fiber Reinforced Concrete.” *Materials Journal*, 93 (3). https://doi.org/10.14359/9804

World Commission on Environment and Development. Our common future. Oxford: Oxford University Press, 1987.

Wu, W. P. (1990). “Thermomechanical Properties of Fiber Reinforced Plastics (FRP) Bars.” *West Virginia University*, pp. 292.

Xin, Dapeng et al. (1992). “One-Dimensional Model for Analysis of CRC Pavement Growth*.” Journal of Transportation Engineering*, 118, pp. 557-575. ASCE

Xu, Chang, et al. (2011). “Analysis of Periodic Cracks in Surface Layer of Pavement Structures.” *Engineering Failure Analysis*, 18 (1), pp. 411–420. https://doi.org/10.1016/j.engfailanal.2010.09.023.

Zhang, Y., Roesler, J., and Dahal, S. (2023). “Predicting transverse crack properties in continuously reinforced concrete pavement.” *Construction and Building Materials*, 364. https://doi.org/10.1016/j.conbuildmat.2022.129842.

Zhang, J., Stang, H., and Li, V. C. (1998). “Fatigue Performance in Flexure of Fiber Reinforced Concrete.” *Materials Journal*, 95 (1). https://doi.org/10.14359/351.

APPENDICES

APPENDIX A. CONCRETE MIX DESIGN

Submittal # 20-GRP-001082 Version 3
GRP FRANK HOUSTON
11/2/2020

Please find the enclosed mix designs listed below with current materials certification reports.

This submission contains the following mix designs:

Mix Code	Description
9357PS	**9.3 ENG 40-60AGG PAIR SUP**

Please note, concrete strength and performance are guaranteed when tested and placed in accordance with all applicable ACI guidelines, AASHTO and ASTM Standard Specifications. Geneva Rock Products requests to be added to the distribution list for all test results. Please order by mix design number.

If you have any questions or concerns, do not hesitate to call us at (801)281-7900.

Respectfully Submitted,

Frank Houston

FRANK HOUSTON

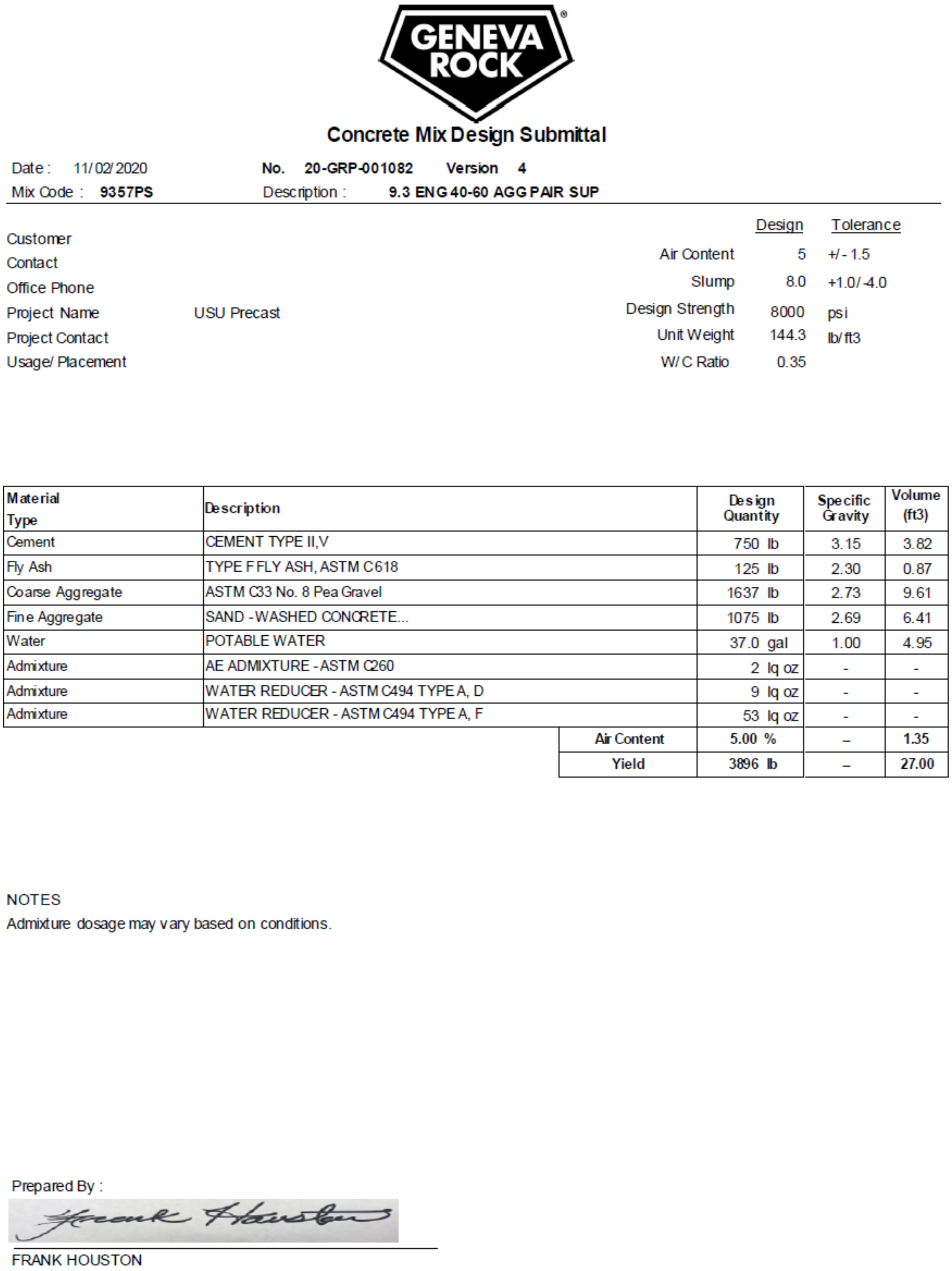

GENEVA ROCK

Concrete Mix Design Submittal

Date : 11/02/2020 **No. 20-GRP-001082 Version 4**

Mix Code : **9357PS** Description : **9.3 ENG 40-60 AGG PAIR SUP**

Customer	
Contact	
Office Phone	
Project Name	USU Precast
Project Contact	
Usage/ Placement	

	Design	Tolerance
Air Content	5	+/- 1.5
Slump	8.0	+1.0/-4.0
Design Strength	8000	psi
Unit Weight	144.3	lb/ft3
W/C Ratio	0.35	

Material Type	**Description**	**Design Quantity**	**Specific Gravity**	**Volume (ft3)**
Cement	CEMENT TYPE II,V	750 lb	3.15	3.82
Fly Ash	TYPE F FLY ASH, ASTM C618	125 lb	2.30	0.87
Coarse Aggregate	ASTM C33 No. 8 Pea Gravel	1637 lb	2.73	9.61
Fine Aggregate	SAND - WASHED CONCRETE...	1075 lb	2.69	6.41
Water	POTABLE WATER	37.0 gal	1.00	4.95
Admixture	AE ADMIXTURE - ASTM C260	2 lq oz	-	-
Admixture	WATER REDUCER - ASTM C494 TYPE A, D	9 lq oz	-	-
Admixture	WATER REDUCER - ASTM C494 TYPE A, F	53 lq oz	-	-
	Air Content	**5.00 %**	–	**1.35**
	Yield	**3896 lb**	–	**27.00**

NOTES

Admixture dosage may vary based on conditions.

Prepared By :

Frank Houston

FRANK HOUSTON

GENEVA ROCK PRODUCTS, INC.
1565 West 400 North • P.O. Box 538 • Orem, UT 84059 • (801) 765-7800 • Fax (801) 765-7830 • www.genevarock.com

AGGREGATE SUBMITTAL

Report of Physical Properties

GRP Material Description: Washed, Concrete
GRP Material Code: SAND
Source Location/Code: Cove / 596
Report Date: January 24, 2020
Reviewed by: Victor Johnson
Report No. 596SAND00120

TEST RESULTS				
Standard	**PHYSICAL PROPERTIES**		**Result**	**Test Source**
ASTM C 29 AASHTO T19	**Unit Weight**	Unit Weight, lbs./cu.ft. =	**112**	
		Voids, % =	**32**	
		☐ Jigged ☐ Loose ☐ Rodded		
ASTM D1557 AASHTO T180	**Modified Proctor**	Max. density, lbs./cu.ft. =		
		Optimum Moisture, % =		
ASTM D698 AASHTO T99	**Standard Proctor**	Max. density, lbs./cu.ft. =		
		Optimum Moisture, % =		
ASTM D4318 AASHTO T89/90	**Liquid Limit**	Liquid Limit=	**0**	
	Plastic Limit	Plastic Limit=	**0**	
	Plasticity Index	Plasticity Index=	**NP**	
ASTM C131 AASHTO T96	**L.A. Abrasion**	Small Coarse Loss, % =		
		Grading/Revolutions, =		
ASTM C535	**L.A. Abrasion**	Large Coarse Loss, % =		
		Grading/Revolutions, =		
ASTM C 128 AASHTO T84	**Fine Specific Gravity & Absorption**	Bulk Specific Gravity (dry) =	**2.639**	
		Bulk Specific Gravity, SSD =	**2.690**	
		Apparent Specific Gravity =	**2.782**	
		Absorption, % =	**1.9**	
ASTM C 127 AASHTO T85	**Coarse Specific Gravity & Absorption**	Bulk Specific Gravity (dry) =		
		Bulk Specific Gravity, SSD =		
		Apparent Specific Gravity =		
		Absorption, % =		
ASTM D2419 AASHTO T176	**Sand Equivalent**	Sand Equivalent, % =	**79**	
ASTM C 88 AASHTO T104	**Soundness**	Coarse Soundness Loss, % =		
		Sodium No. of Cycles =		
	Soundness	Fine Soundness Loss, % =	**1**	
		Sodium No. of Cycles =	**5**	
ASTM C 1252 AASHTO T304	**Fine Aggregate Angularity**	Uncompacted Voids, % =	**44.2**	
		Method C (as received material)		
ASTM C40 AASHTO T21	**Organic Impurities**	Coarse Aggregate, % =		
		Fine Aggregate, % =	**Less than 1**	
ASTM C142 AASHTO T112	**Clay / Friable Particles**	Coarse Aggregate, % =		
		Fine Aggregate, % =	**0**	
ASTM C123 AASHTO T113	**Lightweight Pieces**	Coarse Aggregate, % =		
		Fine Aggregate, % =	**0**	
ASTM D1883 AASHTO T193	**CBR**	Surcharge = 10 lbs CBR @ 0.1"=		
		Swell% = 0.0% CBR @ 0.2"=		
ASTM D5821	**Fractured Face**	1 or 2 Faces =		
		Fractured Face, % =		
ASTM D2487	**Soil Classification**	Group Symbol =		
		Group Name =		
ASTM D2488	**Soil Description & Identification**	Group Symbol =		
		Group Name =		

SIEVE ANALYSIS		
ASTM C136 AASHTO T27		
Sieve Size	**% Passing**	**Spec.**
450 mm (18")		
375 mm (15")		
300 mm (12")		
250 mm (10")		
225 mm (9")		
200 mm (8")		
150 mm (6")		
125 mm (5")		
100 mm (4")		
75.0 mm (3")		
63.0 mm (2-1/2")		
50.0 mm (2")		
37.5 mm (1-1/2")		
25.0 mm (1")		
19.0 mm (3/4")		
12.5 mm (1/2")		
9.5 mm (3/8")	**100**	
6.3 mm (1/4")		
4.75 mm (No.4)	**100**	
2.36 mm (No.8)	**89**	
2.00 mm (No.10)		
1.18 mm (No.16)	**65**	
0.600 mm (No.30)	**44**	
0.425 mm (No.40)		
0.300 mm (No.50)	**22**	
0.180 mm (No.80)		
0.150 mm (No.100)	**6**	
0.075 mm (No.200)	**2.6**	
ASTM D422 **Hydrometer =**		
ASTM C566 AASHTO T255 **Moisture Content, % =**		
ASTM C136 AASHTO T27 **Fineness Modulus (FM) =**		
AASHTO M145 **Classification of Soils =**		
ASTM D4791 Ratio = **Flat & Elongated =**		

BORAL RESOURCES

Materials Testing & Research Facility
2650 Old State Hwy 113
Taylorsville, GA 30178
770-684-0102

ASTM C618 Testing of
Jim Bridger Fly Ash

Sample Date:	12/27 - 1/9/20	**Report Date:**	2/27/2020
Sample Type:	composite	**MTRF ID:**	159JB
Sample ID:	BR-042-19		

Chemical Analysis	**Results**	**ASTM Limit Class F**	**ASTM Limit Class C**
Silicon Dioxide (SiO2)	61.26 %		
Aluminum Oxide (Al2O3)	16.62 %		
Iron Oxide (Fe2O3)	4.78 %		
Sum (SiO2+Al2O3+Fe2O3)	82.66 %	50.0 min	50.0 min
Sulfur Trioxide (SO3)	0.86 %	5.0 max	5.0 max
Calcium Oxide (CaO)	6.36 %		
Magnesium Oxide (MgO)	2.24 %		
Sodium Oxide (Na2O)	3.03 %		
Potassium Oxide (K2O)	1.17 %		
Moisture	0.04 %	3.0 max	3.0 max
Loss on Ignition	0.33 %	6.0 max	6.0 max

Physical Analysis			
Fineness, % retained on 45-µm sieve	20.03 %	34 max	34 max
Strength Activity Index - 7 or 28 day requirement			
7 day, % of control	81 %	75 min	75 min
28 day, % of control	83 %	75 min	75 min
Water Requirement, % control	95 %	105 max	105 max
Autoclave Soundness	0.01 %	0.8 max	0.8 max
Density	2.37 g/cm3		

The test data listed herein was generated by applicable ASTM methods. The reported results pertain only to the sample(s) or lot(s) tested. This report cannot be reproduced without permission from Boral Resources.

Christy Sieg

Christy Sieg
Lab Manager

AASHTO
ACCREDITED

gcp applied technologies

GCP Applied Technologies
62 Whittemore Avenue
Cambridge MA 02140

gcpat.com

SCC Customer Service:
1-877- 423-6491

Darren Smith
Geneva Rock
1565 W 400 N
Orem, Utah 84057
Project Name: Various

March 05, 2020

This is to certify that **Daravair® AT30**, a **Air Entraining Agent**, as manufactured and supplied by GCP Applied Technologies Inc., is formulated to comply with the Specifications for Chemical Admixtures for Concrete, ASTM: **C260**, AASHTO: **M154**.

Daravair® AT30 does not contain calcium chloride or chloride containing compounds as a functional ingredient. Chloride ions may be present in trace amounts contributed from the process water used in manufacturing.

Yours sincerely

Robert J. Hoopes

Robert J. Hoopes
Product Development Engineer
GCP Applied Technologies

gcp applied technologies

GCP Applied Technologies
62 Whittemore Avenue
Cambridge MA 02140

gcpat.com

SCC Customer Service:
1-877- 423-6491

Darren Smith
Geneva Rock
1565 W 400 N
Orem, Utah 84057
Project Name: Various

March 05, 2020

This is to certify that **WRDA® 82**, a **Water Reducer**, as manufactured and supplied by GCP Applied Technologies Inc., is formulated to comply with the Specifications for Chemical Admixtures for Concrete, ASTM: **C494, Type A, D**, AASHTO: **M194, Type A, D**.

WRDA® 82 does not contain calcium chloride or chloride containing compounds as a functional ingredient. Chloride ions may be present in trace amounts contributed from the process water used in manufacturing.

Yours sincerely

Robert J. Hoopes

Robert J. Hoopes
Product Development Engineer
GCP Applied Technologies

gcp applied technologies

GCP Applied Technologies
62 Whittemore Avenue
Cambridge MA 02140

gcpat.com

SCC Customer Service:
1-877- 423-6491

Darren Smith
Geneva Rock
1565 W 400 N
Orem, Utah 84057
Project Name: Various

March 05, 2020

This is to certify that **ADVA® 198**, a **High Range Water Reducer**, as manufactured and supplied by GCP Applied Technologies Inc., is formulated to comply with the Specifications for Chemical Admixtures for Concrete, ASTM: **C494 Type A, F and ASTM C1017**, AASHTO: **M194, Type A, F**.

ADVA® 198 does not contain calcium chloride or chloride containing compounds as a functional ingredient. Chloride ions may be present in trace amounts contributed from the process water used in manufacturing.

Yours sincerely

Robert J. Hoopes

Robert J. Hoopes
Product Development Engineer
GCP Applied Technologies

STRENGTH PERFORMANCE REPORT

Mix : 9357 PS - 9.3 ENG 40-60 AGG PAIR SUP
Period : 09 Aug 2017 To 02 Jan 2018

	Air Content %	Concrete Temp deg F	Slump in	Strength28D psi
Count	11	11	11	11
Average	4.73	74	6.64	9680
STDEV	0.81	7	1.08	870
COV%	17.1	9.9	16.3	9.0
Range Min	3.50	66	5.00	8560
Range Max	6.00	86	8.50	11420

Date	Sample	Air Content %	Concrete Temp deg F	Slump in	Strength28D psi
1/2/2018	4656	5.50	70	8.50	9420
12/19/2017	4228	4.50	69	5.00	11420
12/5/2017	3154	4.50	66	6.50	10760
11/30/2017	2879	5.00	69	6.00	9440
11/27/2017	2588	6.00	72	5.25	10190
11/16/2017	2125	4.50	68	5.75	8560
10/4/2017	7678	6.00	68	7.50	9710
9/18/2017	6354	4.00	80	6.50	8830
8/18/2017	4450	4.30	85	7.00	9490
8/16/2017	4266	3.50	86	7.50	8720
8/9/2017	3787	4.20	79	7.50	9900

Date : 11/2/2020 Page 1 of 1

APPENDIX B. ADDITIONAL FIGURES

Figure B.1 Photo of Slump Test

Figure B.2 Filling the GFRP Rebar Form with Concrete

Figure B.3 Adding Macro Fibers to Concrete Drum Mixer

Figure B.4 Filling the Mini-Beam Molds with FRC

Figure B.5 Creating Concrete Cylinders

Figure B.6 All Concrete Specimens after Initial Construction

Figure B.7 Insulated Tarp over Concrete Specimens

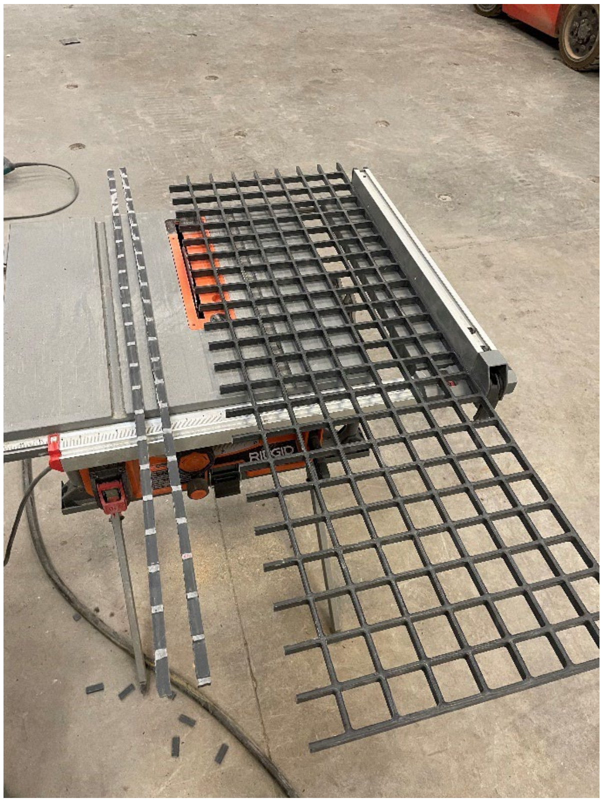

Figure B.8 Cutting Linear Testing Specimens from the FRP Grid

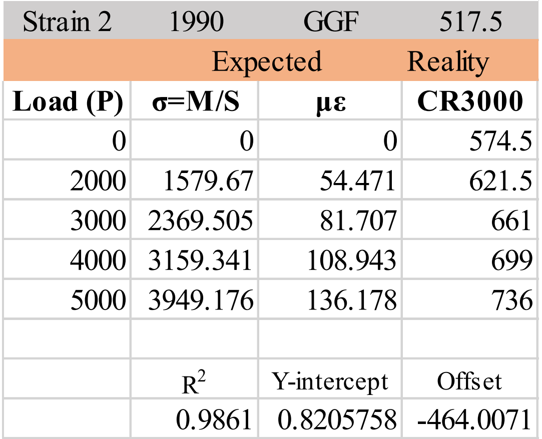

Strain 2	1990	GGF	517.5
	Expected		Reality
Load (P)	**σ=M/S**	**με**	**CR3000**
0	0	0	574.5
2000	1579.67	54.471	621.5
3000	2369.505	81.707	661
4000	3159.341	108.943	699
5000	3949.176	136.178	736
	R^2	Y-intercept	Offset
	0.9861	0.8205758	-464.0071

Figure B.9 Strain Gauge 2 Calibration Table

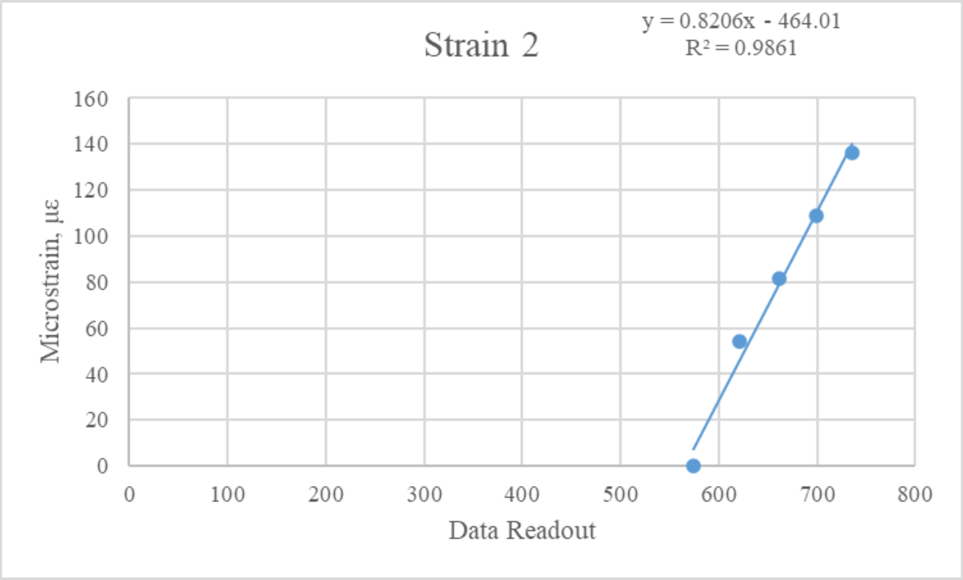

Figure B.10 Strain Gauge 2 Calibration Graph

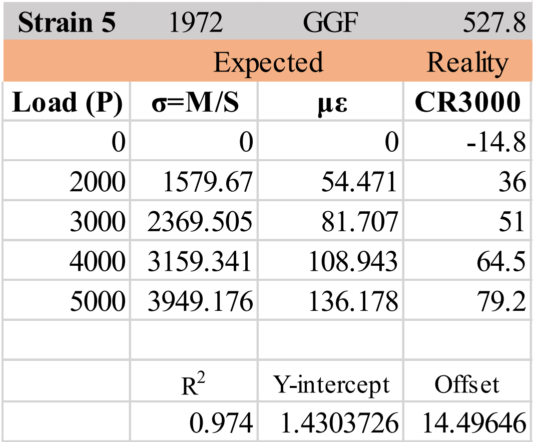

Strain 5	1972	GGF	527.8
	Expected		Reality
Load (P)	**σ=M/S**	**με**	**CR3000**
0	0	0	-14.8
2000	1579.67	54.471	36
3000	2369.505	81.707	51
4000	3159.341	108.943	64.5
5000	3949.176	136.178	79.2
	R^2	Y-intercept	Offset
	0.974	1.4303726	14.49646

Figure B.11 Strain Gauge 5 Calibration Table

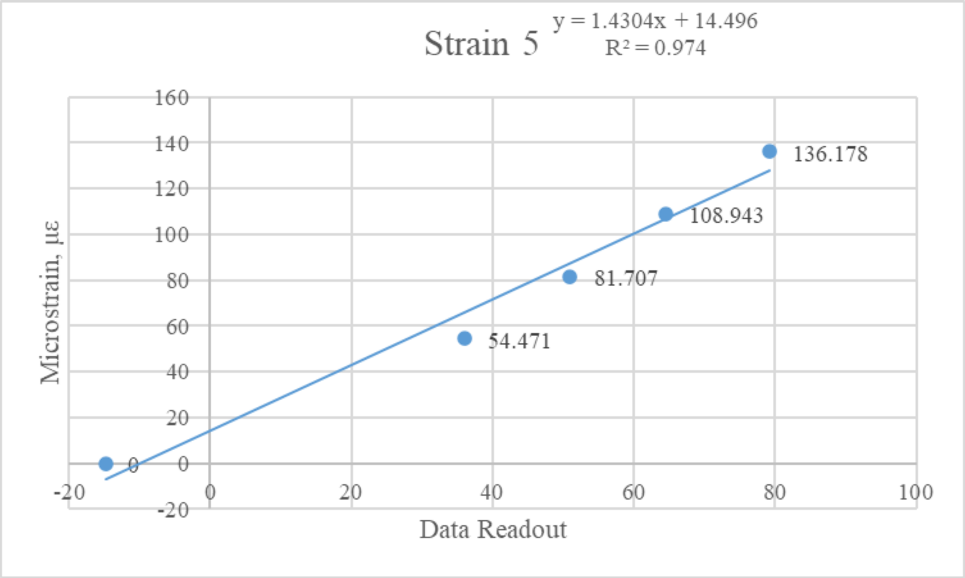

Figure B.12 Strain Gauge 5 Calibration Graph

Strain 6	2611	GGF	539.5
	Expected		Reality
Load (P)	**σ=M/S**	**με**	**CR3000**
0	0	0	1017
2000	1579.67	54.471	1047.5
3000	2369.505	81.707	1077
4000	3159.341	108.943	1106.5
5000	3949.176	136.178	1137.5
	R^2	Y-intercept	Offset
	0.9734	1.0896457	-1097.397

Figure B.13 Strain Gauge 6 Calibration Table

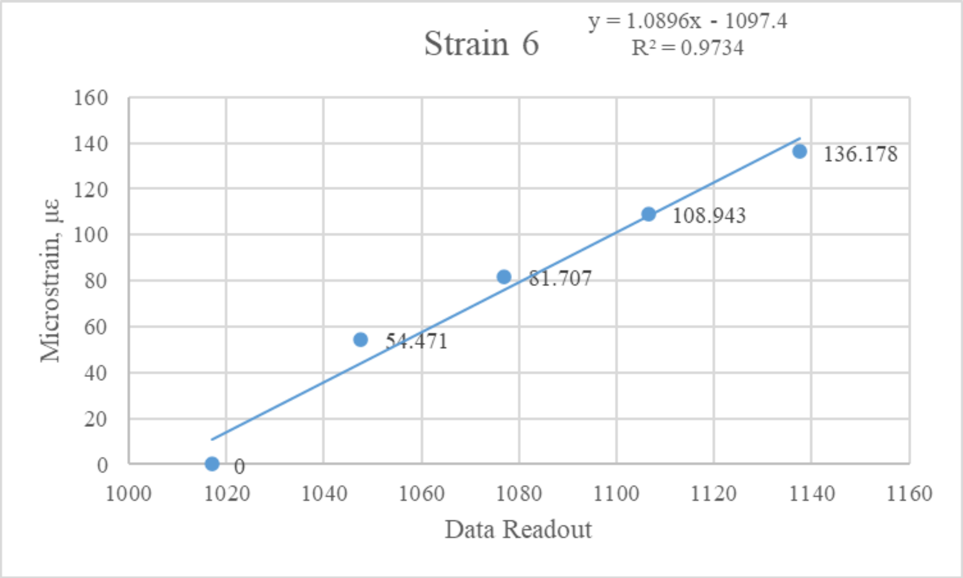

Figure B.14 Strain Gauge 6 Calibration Graph

Strain 7	1996	GGF	579.5
	Expected		Reality
Load (P)	**σ=M/S**	**με**	**CR3000**
0	0	0	5.5
2000	1579.67	54.471	77
3000	2369.505	81.707	115
4000	3159.341	108.943	149
5000	3949.176	136.178	182
	R^2	Y-intercept	Offset
	0.9995	0.7671122	-4.82381

Figure B.15 Strain Gauge 7 Calibration Table

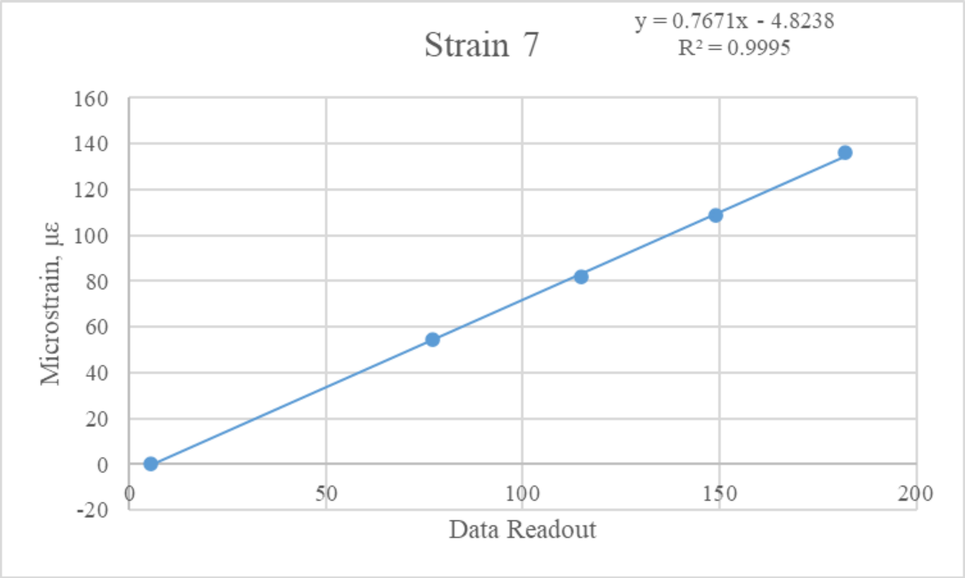

Figure B.16 Strain Gauge 7 Calibration Graph

Strain 8	1973	GGF	509.6
	Expected		Reality
Load (P)	**σ=M/S**	**με**	**CR3000**
0	0	0	1.5
2000	1579.67	54.471	40
3000	2369.505	81.707	71.5
4000	3159.341	108.943	106.5
5000	3949.176	136.178	138
	R^2	Y-intercept	Offset
	0.9819	0.9665078	7.1546363

Figure B.17 Strain Gauge 8 Calibration Table

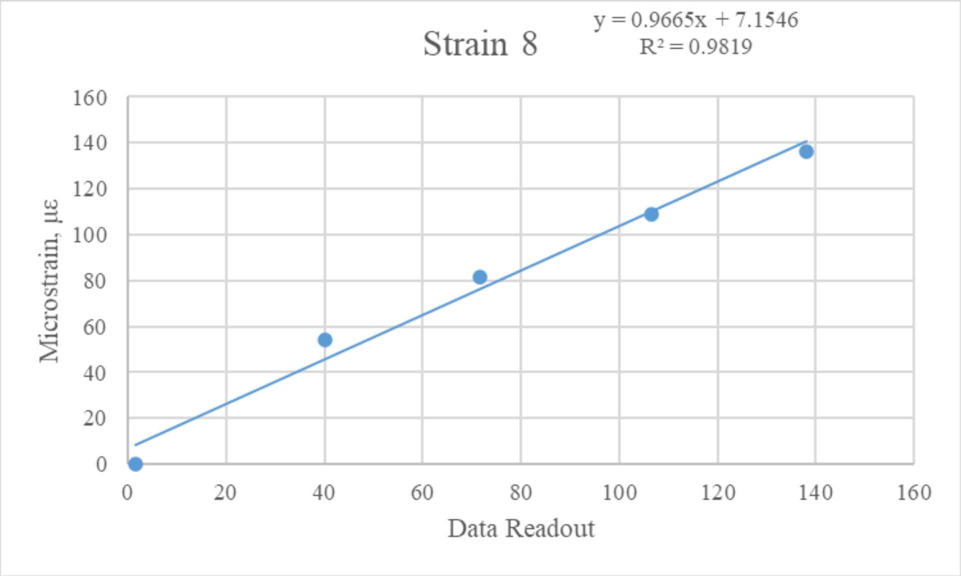

Figure B.18 Strain Gauge 8 Calibration Graph

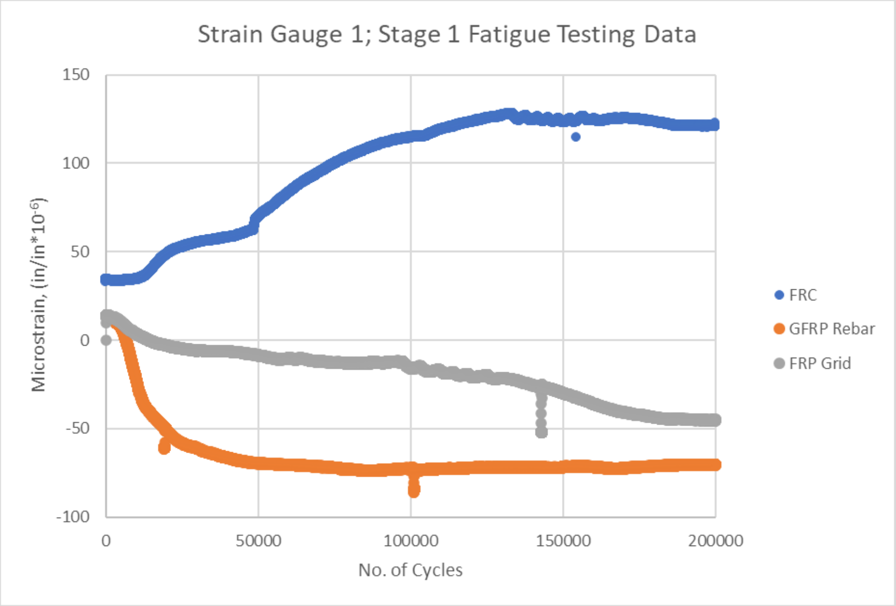

Figure B.19 Strain Gauge 1; Stage 1 Fatigue Testing Data

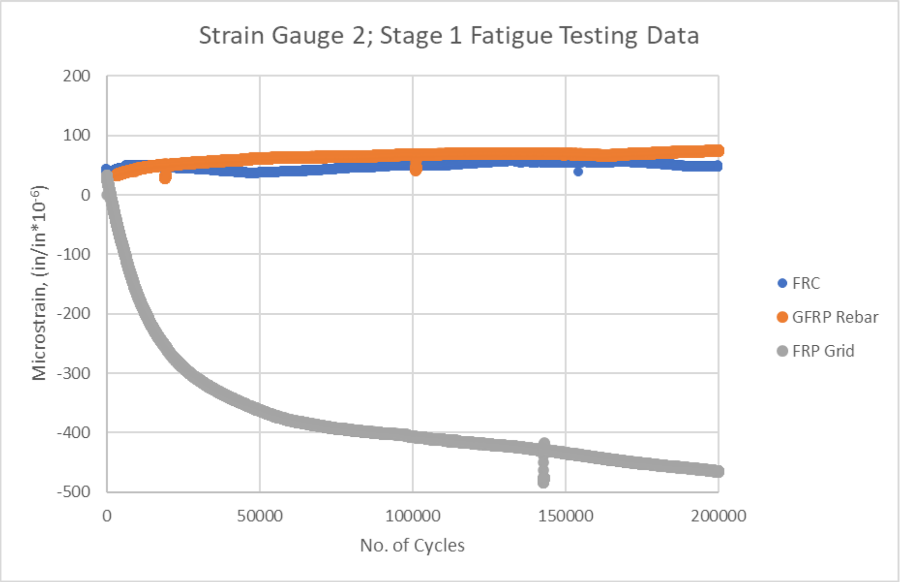

Figure B.20 Strain Gauge 2; Stage 1 Fatigue Testing Data

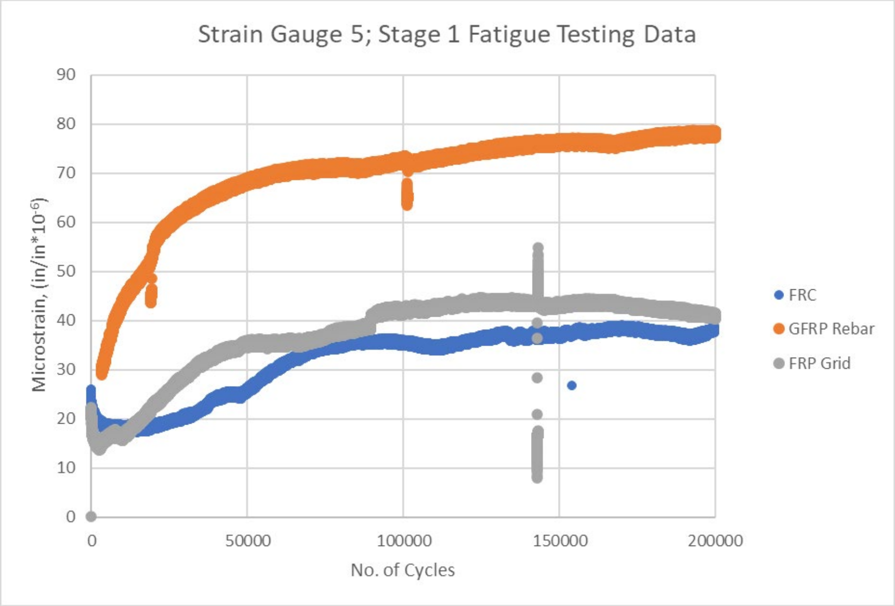

Figure B.21 Strain Gauge 5; Stage 1 Fatigue Testing Data

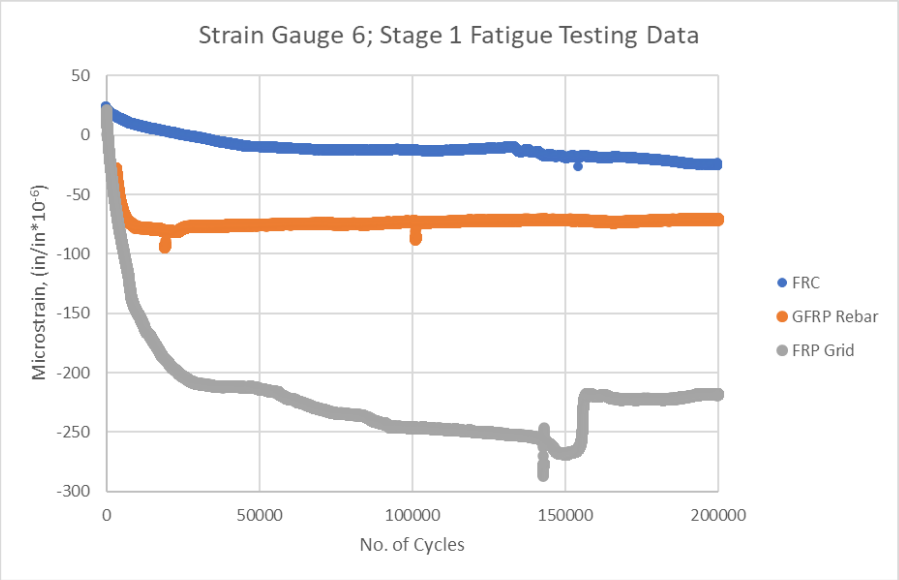

Figure B.22 Strain Gauge 6; Stage 1 Fatigue Testing Data

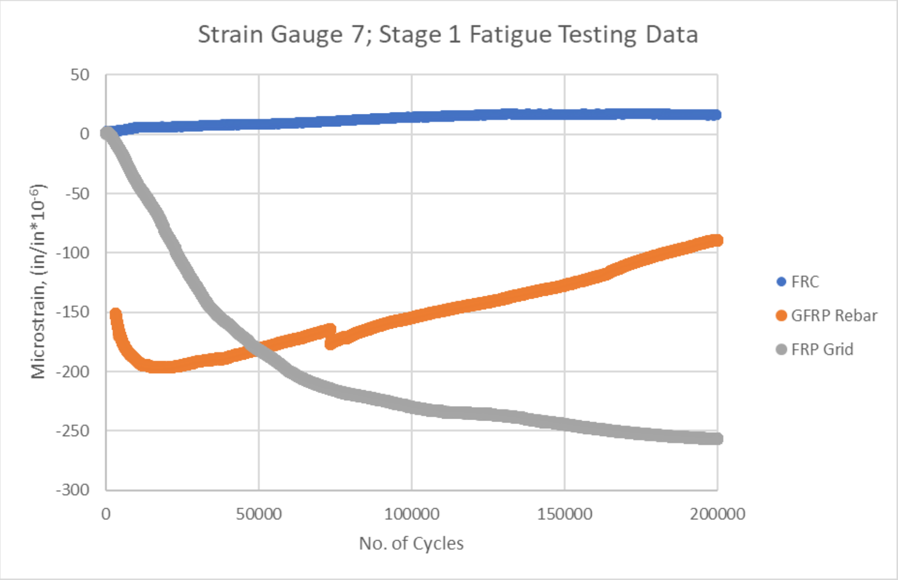

Figure B.23 Strain Gauge 7; Stage 1 Fatigue Testing Data

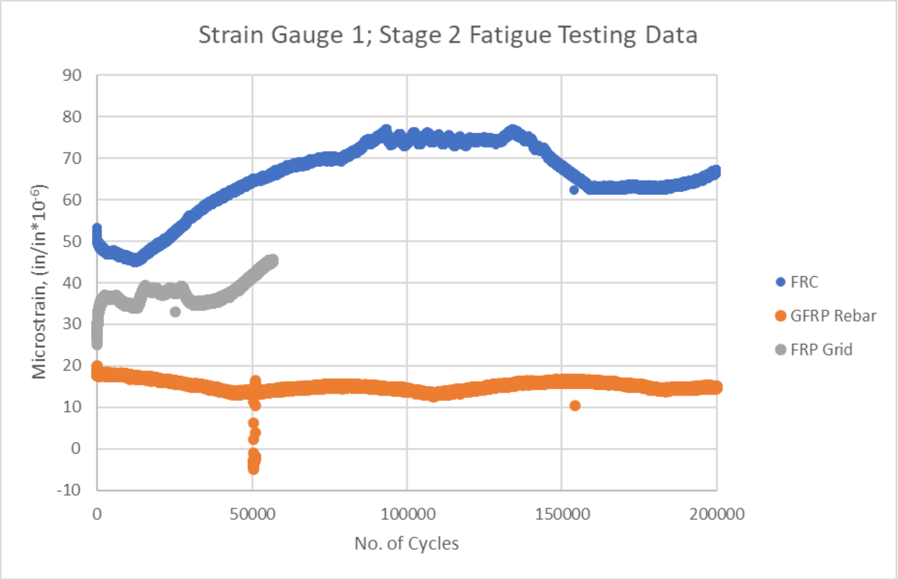

Figure B.24 Strain Gauge 1; Stage 2 Fatigue Testing Data

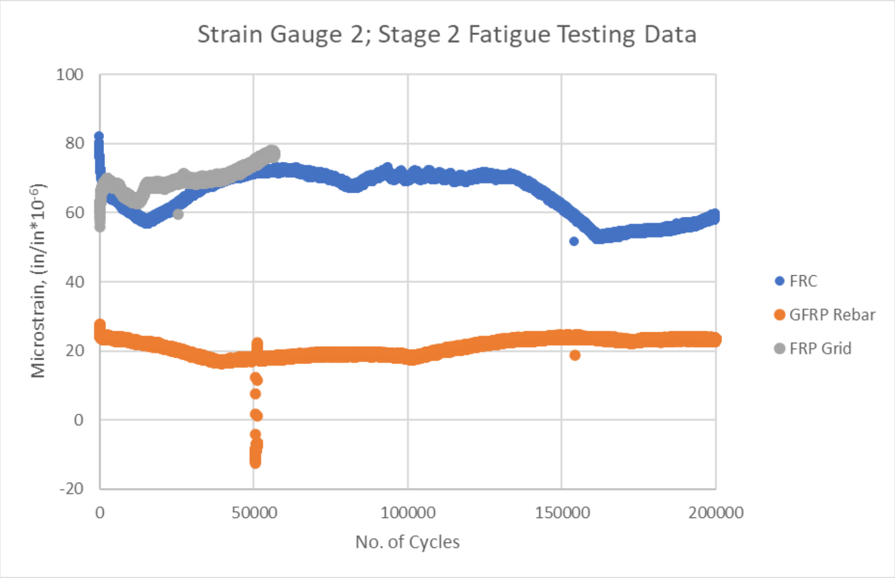

Figure B.25 Strain Gauge 2; Stage 2 Fatigue Testing Data

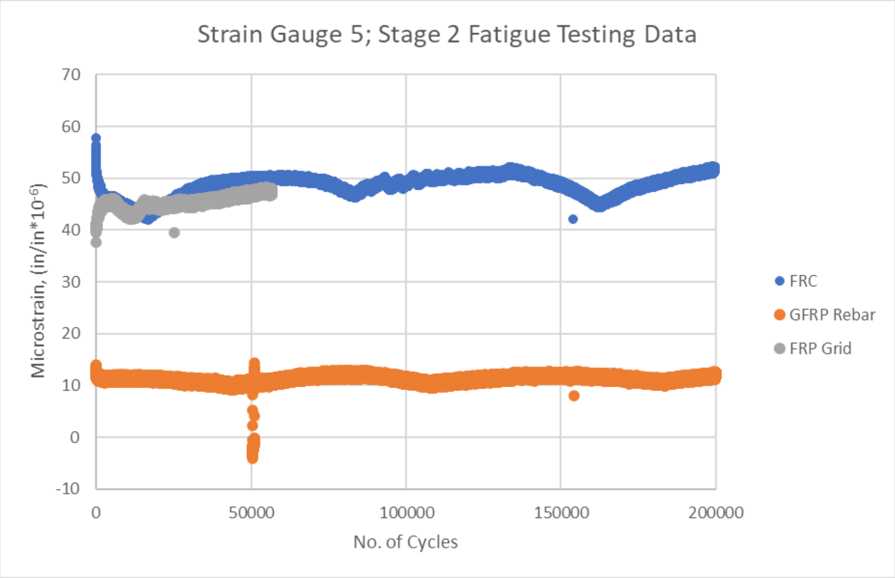

Figure B.26 Strain Gauge 5; Stage 2 Fatigue Testing Data

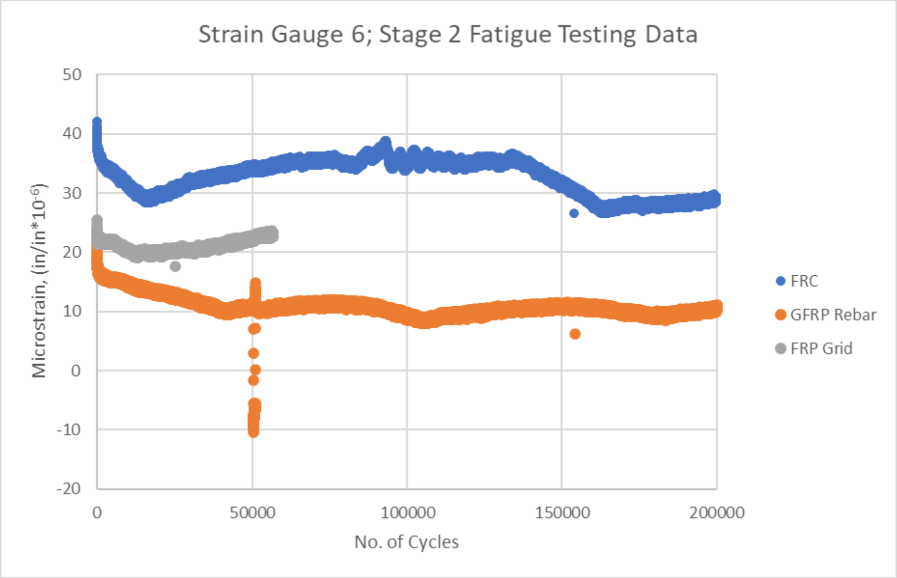

Figure B.27 Strain Gauge 6; Stage 2 Fatigue Testing Data

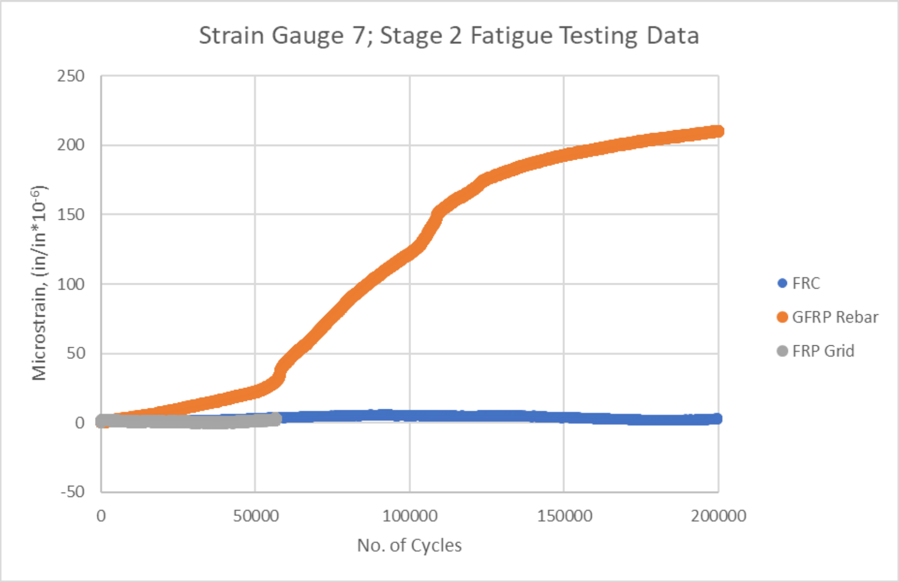

Figure B.28 Strain Gauge 7; Stage 2 Fatigue Testing Data

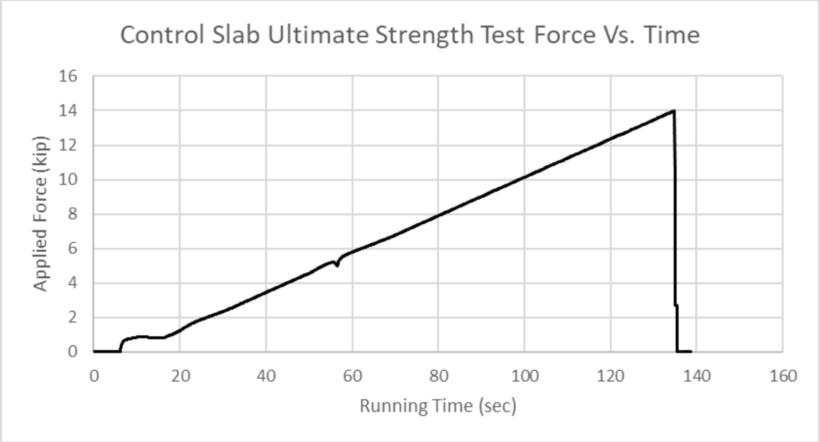

Figure B.29 Control Slab Ultimate Strength Test Force vs. Time

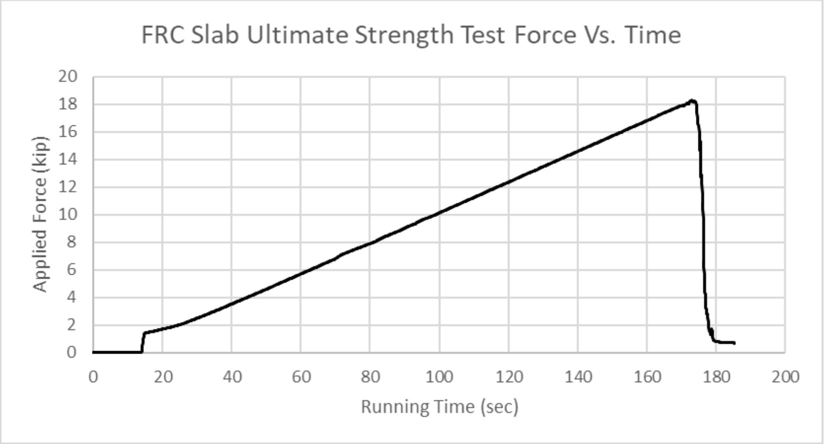

Figure B.30 FRC Slab Ultimate Strength Test Force vs. Time.

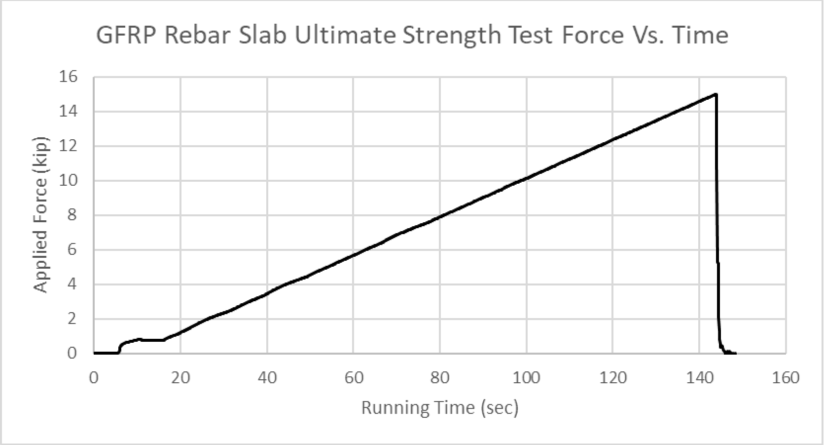

Figure B.31 GFRP Rebar Slab Ultimate Strength Test Force vs. Time

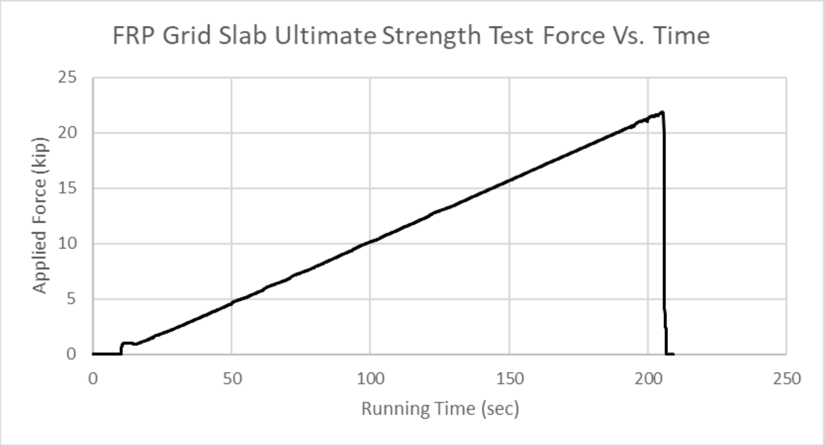

Figure B.32 FRP Grid Slab Ultimate Strength Test Force vs. Time

APPENDIX C. HAND CALCULATIONS

CALCULATE REINFORCEMENT BASED ON EQUAL STRESS

HS-20 ON 12" SLAB

$P_0 := 32\ \text{kip}$

$b_0 := 20\ \text{in}$

$h_0 := 12\ \text{in}$

$width_0 := 8.727\ \text{ft}$

*The width was determined by matching the ratio of the wheel spacing to total width of my experimental slabs

$$I_0 := \frac{b_0 \cdot h_0^{\,3}}{12} = 2880\ \text{in}^4$$

$$w_0 := \frac{P_0}{width_0} = 3.6668\ \frac{\text{kip}}{\text{ft}}$$

From a RISA-2D model:

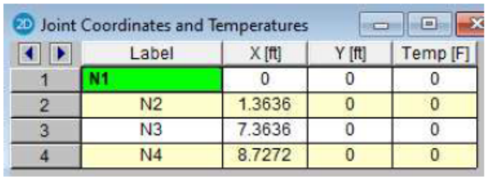

Joint Coordinates and Temperatures

	Label	X [ft]	Y [ft]	Temp [F]
1	N1	0	0	0
2	N2	1.3636	0	0
3	N3	7.3636	0	0
4	N4	8.7272	0	0

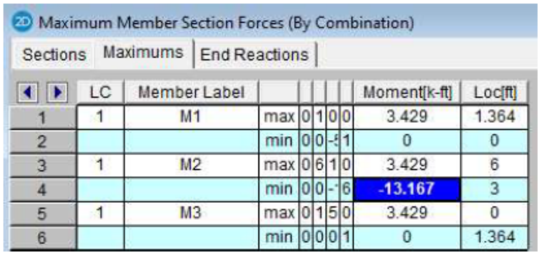

Maximum Member Section Forces (By Combination)

	LC	Member Label						Moment[k-ft]	Loc[ft]
1	1	M1	max	0	1	0	0	3.429	1.364
2			min	0	0	-5	1	0	0
3	1	M2	max	0	6	1	0	3.429	6
4			min	0	0	-1	6	-13.167	3
5	1	M3	max	0	1	5	0	3.429	0
6			min	0	0	0	1	0	1.364

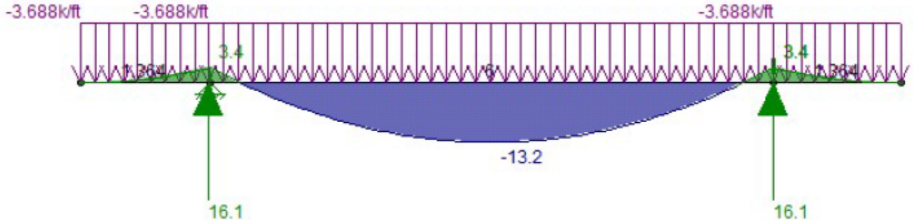

$M_0 := 13.167\ \text{kip ft}$

$$y_0 := \frac{h_0}{2} = 6\ \text{in}$$

$$\sigma := \frac{M_0 \cdot y_0}{I_0} = 329.175\ \text{psi}$$

EXPERIMENTAL SLABS

$b := 10\ \text{in}$

$h := 10\ \text{in}$

$$y := \frac{h}{2} = 5\ \text{in}$$

$$I := \frac{b \cdot h^3}{12} = 833.3333\ \text{in}^4$$

$$M := \frac{\sigma \cdot I}{y} = 4.5719\ \text{kip ft}$$

From a RISA-2D model:

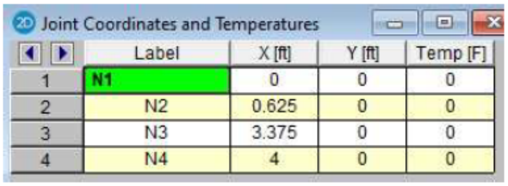

	Label	X [ft]	Y [ft]	Temp [F]
1	N1	0	0	0
2	N2	0.625	0	0
3	N3	3.375	0	0
4	N4	4	0	0

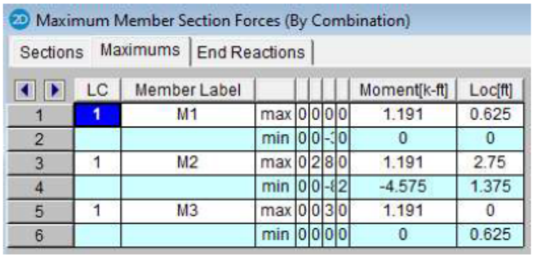

	LC	Member Label						Moment[k-ft]	Loc[ft]
1	1	M1	max	0	0	0	0	1.191	0.625
2			min	0	0	-3	0	0	0
3	1	M2	max	0	2	8	0	1.191	2.75
4			min	0	0	-8	2	-4.575	1.375
5	1	M3	max	0	0	3	0	1.191	0
6			min	0	0	0	0	0	0.625

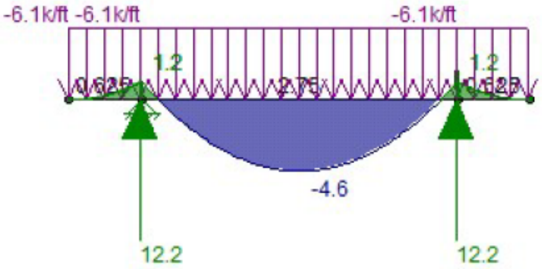

$w := 6.1\ \frac{\text{kip}}{\text{ft}}$

$f'c := 8\ \text{ksi}$

$f_y := 75\ \text{ksi}$

$P := \frac{w \cdot 4\ \text{ft}}{2} = 12.2\ \text{kip}$

$2 \cdot P = 24.4\ \text{kip}$

$d := h - 2.125\ \text{in} = 7.875\ \text{in}$

Assume #2 bars spaced at 5" o.c.

$A_s := \frac{\pi \cdot (0.25\ \text{in})^2}{4} \cdot \frac{12}{5} = 0.1178\ \text{in}^2$

$a := \frac{A_s \cdot f_y}{0.85 \cdot f'c \cdot b} = 0.1299\ \text{in}$

$M_n := A_s \cdot f_y \cdot \left(d - \frac{a}{2}\right) = 5.7506\ \text{kip ft}$

$\frac{M_n}{M} = 1.2578$

NOW FIND THE EQUIVALENT LOAD FOR A MAX. LOAD ALLOWED ON INTERSTATES

$P_{max} := 50\ \text{kip}$ See FHWA compilation of state weight limits report.

$w_{max} := \frac{P_{max}}{width_0} = 5.7293\ \frac{\text{kip}}{\text{ft}}$

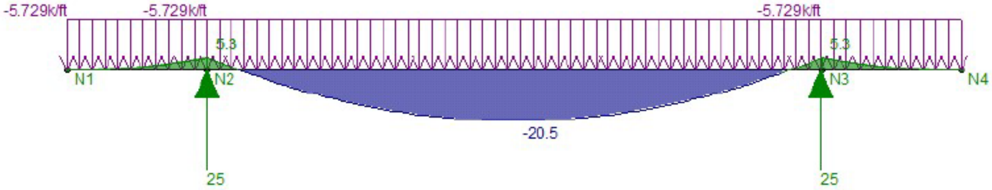

$M_{max} := 20.455 \text{ kip ft}$

$$\sigma_{max} := \frac{M_{max} \cdot Y_0}{I_0} = 511.375 \text{ psi}$$

$$M_{max.experiment} := \frac{\sigma_{max} \cdot I}{y} = 7.1024 \text{ kip ft}$$

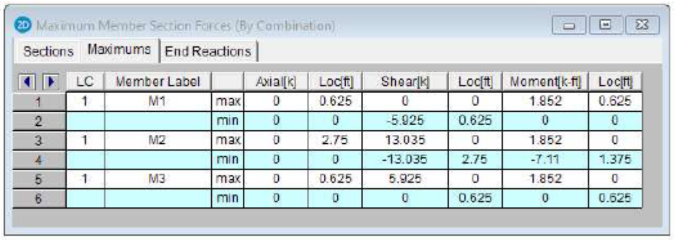

	LC	Member Label		Axial[k]	Loc[ft]	Shear[k]	Loc[ft]	Moment[k-ft]	Loc[ft]
1	1	M1	max	0	0.625	0	0	1.852	0.625
2			min	0	0	-5.925	0.625	0	0
3	1	M2	max	0	2.75	13.035	0	1.852	0
4			min	0	0	-13.035	2.75	-7.11	1.375
5	1	M3	max	0	0.625	5.925	0	1.852	0
6			min	0	0	0	0.625	0	0.625

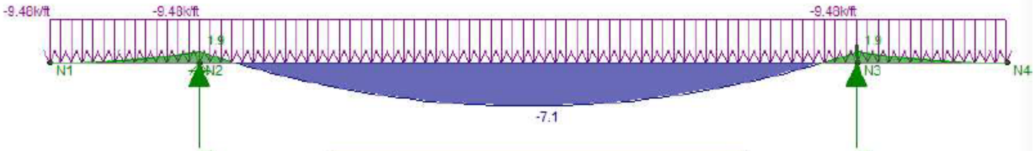

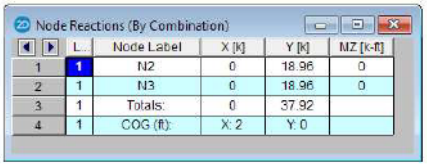

	L...	Node Label	X [k]	Y [k]	MZ [k-ft]
1	1	N2	0	18.96	0
2	1	N3	0	18.96	0
3	1	Totals:	0	37.92	
4	1	COG (ft):	X: 2	Y: 0	

$P := 18.96 \text{ kip}$

$2 \cdot P = 37.92 \text{ kip}$ Load applied by RAM to experimental slab.

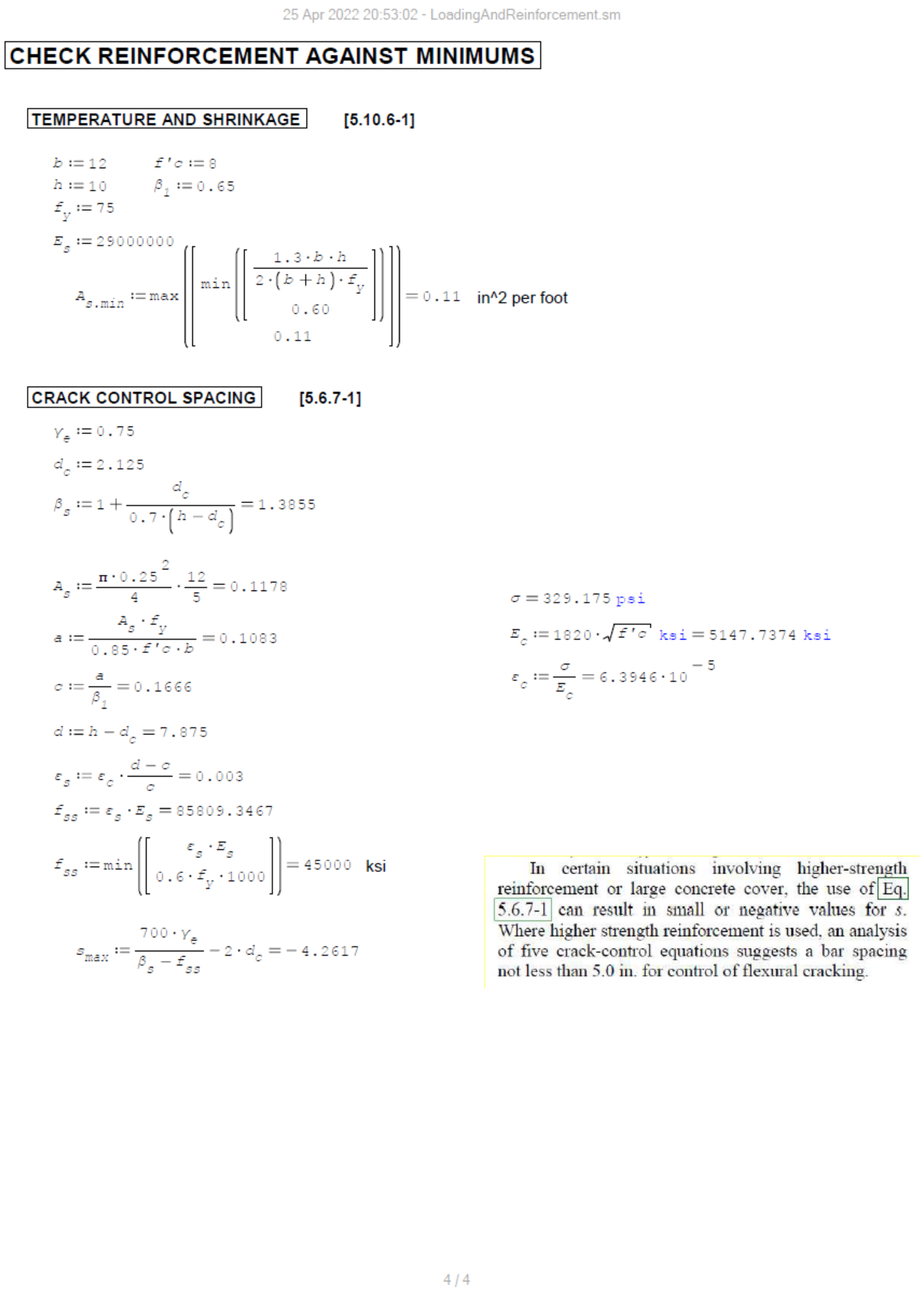

25 Apr 2022 20:53:02 - LoadingAndReinforcement.sm

CHECK REINFORCEMENT AGAINST MINIMUMS

TEMPERATURE AND SHRINKAGE [5.10.6-1]

$b := 12 \qquad f'c := 8$

$h := 10 \qquad \beta_1 := 0.65$

$f_y := 75$

$E_s := 29000000$

$$A_{s.min} := \max\left(\begin{bmatrix} \min\left(\begin{bmatrix} \dfrac{1.3 \cdot b \cdot h}{2 \cdot (b+h) \cdot f_y} \\ 0.60 \end{bmatrix}\right) \\ 0.11 \end{bmatrix}\right) = 0.11$$ in^2 per foot

CRACK CONTROL SPACING [5.6.7-1]

$\gamma_e := 0.75$

$d_c := 2.125$

$$\beta_s := 1 + \frac{d_c}{0.7 \cdot (h - d_c)} = 1.3855$$

$$A_s := \frac{\pi \cdot 0.25^2}{4} \cdot \frac{12}{5} = 0.1178$$

$$a := \frac{A_s \cdot f_y}{0.85 \cdot f'c \cdot b} = 0.1083$$

$$c := \frac{a}{\beta_1} = 0.1666$$

$d := h - d_c = 7.875$

$$\varepsilon_s := \varepsilon_c \cdot \frac{d - c}{c} = 0.003$$

$f_{ss} := \varepsilon_s \cdot E_s = 85809.3467$

$$f_{ss} := \min\left(\begin{bmatrix} \varepsilon_s \cdot E_s \\ 0.6 \cdot f_y \cdot 1000 \end{bmatrix}\right) = 45000$$ ksi

$$s_{max} := \frac{700 \cdot \gamma_e}{\beta_s - f_{ss}} - 2 \cdot d_c = -4.2617$$

$\sigma = 329.175$ psi

$E_c := 1820 \cdot \sqrt{f'c}$ ksi $= 5147.7374$ ksi

$$\varepsilon_c := \frac{\sigma}{E_c} = 6.3946 \cdot 10^{-5}$$

In certain situations involving higher-strength reinforcement or large concrete cover, the use of Eq. 5.6.7-1 can result in small or negative values for *s*. Where higher strength reinforcement is used, an analysis of five crack-control equations suggests a bar spacing not less than 5.0 in. for control of flexural cracking.

4 / 4

CALCULATE LOADING RATE, r

$S := 150\ \frac{\mathrm{psi}}{\mathrm{min}}$

$b := 24\ \mathrm{in}$

$d := 10\ \mathrm{in}$

$L := 36\ \mathrm{in}$

$$r := \frac{2 \cdot S \cdot b \cdot d^{2}}{3 \cdot L} = 6666.6667\ \frac{\mathrm{lbf}}{\mathrm{min}}$$

[ASTM C293 Eq 1]

ESTIMATE ULTIMATE LOAD OF CONTROL SPECIMEN

$f'c := 5291\ \ psi$

$\lambda := 1.0$

$R := 7.5 \cdot \lambda \cdot \sqrt{f'c}\ \mathrm{psi} = 545.5445\ \mathrm{psi}$

[ACI 318-14 Eq 19.2.3.1]

$$\left(R = \frac{M \cdot c}{I}\right) = \frac{\left(\frac{w \cdot L^{2}}{8} + \frac{P \cdot L}{4}\right) \cdot c}{I}$$

The stress in the extreme tension fiber is limited by the Modulus of Rupture, R.

$$w := 145\ \frac{\mathrm{lbf}}{\mathrm{ft}^{3}} \cdot b \cdot d = 241.6667\ \frac{\mathrm{lbf}}{\mathrm{ft}}$$

$$c := \frac{d}{2} = 5\ \mathrm{in}$$

$$I := \frac{b \cdot d^{3}}{12} = 2000\ \mathrm{in}^{4}$$

$$P_{estimate} := \left(\frac{R \cdot I}{c} - \frac{w \cdot L^{2}}{8}\right) \cdot \frac{4}{L} = 23.8839\ \mathrm{kip}$$

VERIFY ULTIMATE LOAD OF CONTROL SPECIMEN USING ASTM EQUATION

$$P_{verify} := \frac{R \cdot 2 \cdot b \cdot d^{2}}{3 \cdot L} = 24.2464\ \mathrm{kip}$$

[ASTM C293 Eq 2]

CALCULATE MAGNITUDE OF STARTING LOAD, P_0

$$P_0 := \min\left(\begin{bmatrix} P_{estimate} \\ P_{verify} \end{bmatrix}\right) \cdot 0.03 = 716.5176\ \mathrm{lbf}$$

APPENDIX D. CAMPBELL SCIENTIFIC CR3000 MICROLOGGER CODE

```
'\Program description

' Measures 1 LVDT and 8 each BDI ST350 strain gages at 100Hz sample rate.


'\\Program history


'\Original version:

' IPTS DAQ.CR3, Signature=60808, Received from Nathan Raine 7 January 2021.


'\ Modification m1, 7 January 2021, markw@campbellsci.com, 435-227-9574, technical support
{case:132407}

' Added channel assignments table.

' Changed LVDT measurement count from 2 to 1 and added 8 each BDI ST350 strain gages.

'\ Modification m2, 28 January 2021, nateraine, modified BrFull program, DiffChan from 1 to 7

' which is where the strain gauges start.

'\ Modification m3, 31 January 2021, nateraine, testing and modifying hysterisis and strain gauge

' calibration factors.

' test: hysterisis set to 10 from 1e6, public strain gauges set to corresponding GGF

' Modification m4, 1 February 2021, nateraine, assigned channels to new strain gauges. Modifying

' GGF and hystersis - lines 123 and 131 from 100 to 20 and line 198 from 10 to 50

' both are done to try and get 20 Hz sampling.

' Modification m5, January 2022, thadhansen, updated GGF and hysteresis for updated calibration

' of strain gauges. Changed sampling rate to 10 Hz. Reviewed with Campbell Sci Technician to

' ensure the code was functioning correctly.


'\Program notes:
```

```
' (1) before starting, need to calibrate the hysteresis items on a specimen to get an accurate calibration

'\\Channel assignments:

'12VDC_PowerOut      : 12VDC power for LVDT's
'G_PowerGround       : Ground for 12VDC power return for LVDT';s
'DiffVoltCh01H_SECh_01:
'DiffVoltCh01L_SECh_02:
'DiffVoltCh02H_SECh_03: LVDT#01_Signal+
'DiffVoltCh02L_SECh_04: LVDT#02_Signal-
'DiffVoltCh03H_SECh_05:
'DiffVoltCh03L_SECh_06:
'DiffVoltCh04H_SECh_07:
'DiffVoltCh04L_SECh_08:
'DiffVoltCh05H_SECh_09:
'DiffVoltCh05L_SECh_10:
'DiffVoltCh06H_SECh_11:
'DiffVoltCh06L_SECh_12:
'DiffVoltCh07H_SECh_13: ST350#01_Signal+
'DiffVoltCh07L_SECh_14: ST350#01_Signal-
'DiffVoltCh08H_SECh_15: ST350#02_Signal+
'DiffVoltCh08L_SECh_16: ST350#02_Signal-
'DiffVoltCh09H_SECh_17: ST350#03_Signal+
'DiffVoltCh09L_SECh_18: ST350#03_Signal-
'DiffVoltCh10H_SECh_19: ST350#04_Signal+
```

```
'DiffVoltCh10L_SECh_20: ST350#04_Signal-
'DiffVoltCh11H_SECh_21: ST350#05_Signal+
'DiffVoltCh11L_SECh_22: ST350#05_Signal-
'DiffVoltCh12H_SECh_23: ST350#06_Signal+
'DiffVoltCh12L_SECh_24: ST350#06_Signal-
'DiffVoltCh13H_SECh_25: ST350#07_Signal+
'DiffVoltCh13L_SECh_26: ST350#07_Signal-
'DiffVoltCh14H_SECh_27: ST350#08_Signal+
'DiffVoltCh14L_SECh_28: ST350#08_Signal-
'AnalogGrond_AG       : Return ground for ST350 excitations. All AGs (upside down trees) are same ground.
'Excitation_Ch_Vx1    :
'Excitation_Ch_Vx2    : Excitation for ST350's #01-#03
'Excitation_Ch_Vx3    : Excitation for ST350's #04-#06
'Excitation_Ch_Vx4    : Excitation for ST350's #07-#08
'AnalogGrond_AG       :
'Excitation_CAO_01    :
'Excitation_CAO_02    :
'Excitation_Ch_IX1    :
'Excitation_Ch_IX2    :
'Excitation_Ch_IX3    :
'Excitation_Ch_IX4    :
'PulseChannel_01      :
'PulseChannel_02      :
'PulseChannel_03      :
'PulseChannel_04      :
```

```
'Switched12V#1        :

'//



'\\ Declarations:

'###################################################
' for offset zero of strain sensors
Public FieldcalAvgs
Public Flag(8) As Boolean 'Flag 8 Zeros offset of strain sensor
Public CalFileLoaded As Boolean
Dim R
Public GStrain(8): Units GStrain() = unitless


'\\\\\\\\\\\\\\\\\\\\\\\\\\\\\\\\\\\\\\\\\\\\\\\\\For Mainraw
'          Public ST350_Ref          ={       1,       2,       3,       4,       5,       6,       7,       8 }
'                       ={    1996,    1990,    1982,    3211,    1972,    2611,    2612,    1973 }
          Public ST350_Mult2(8)        ={  579.50 ,  517.50 ,  422.27 ,  499.20 ,  527.80 ,  539.50 ,  515.90 ,
509.6  }
          Public ST350_oSet2(8)        ={  000.00 ,  000.00 ,  000.00 ,  000.00 ,  000.00 ,  000.00 ,  000.00 ,
000.00  }
'///////////////////////////////////
```

```
Public StrainGF(8) = {  1000/579.50 ,  1000/517.50 ,  1000/422.27  , 1000/499.20 ,  1000/527.80 ,
1000/539.50 ,  1000/515.90 ,  1000/509.6  }

Units StrainGF() = unitless

Public ScanFlg1x(8) As Boolean

Public GStrainRaw(8): Units GStrainRaw() = unitless

Public CalStartIdx

Public FlagMode8

Public StrainZeroMV(8): Units StrainZeroMV() = unitless

Public CalMode

Public SKnownVar(8)



'#############################################

        Public StorageFlag(2) As Boolean = {  True,  True }

        Alias  StorageFlag(1) = Store_Main 'Alias is used to assign the second name of Public variable

        Alias  StorageFlag(2) = Store_Raw

        Public LVDT_Distance : Units LVDT_Distance = TBD 'To be determined

        Public LVDT_mV 'raw data

        Public LVDT_Mult = -0.01141229*.0387 '0.0387 is a slope in calibration cal

        Public LVDT_oSet = 1.3013


        Public ST350_uStrain(8), ST350_mVPV(8),ST350_uStrainraw(8)

 Units ST350_uStrain() = microstrain

 Units ST350_mVPV() = mV/V
```

```
	Public ST350_Mult(8) ={  0.68344 ,  1.62052 ,  0.70256 ,  0.96906 ,  1.154 ,  1.111 ,  0.695 , 1.372  } 'from a slope in calibration excel



'\\\ Data Tables:


	DataTable(Main,Store_Main,-1)

	CardOut(0,-1)' -1 for spending all spaces in a memory card

	DataInterval(0,0,0,10)

	Sample(8,ST350_uStrain(),IEEE4)

	Sample(1,LVDT_Distance(),IEEE4)'\\\\\\I don't know about which unit it is for the displacement? Pilaiwan

	EndTable

	'\\\\\\\\\\\\\\\\\\\

  DataTable(Mainraw,true,-1)

	CardOut(0,-1)

	DataInterval(0,0,0,10)

	Sample(8,ST350_uStrainraw(),IEEE4)

	EndTable

'\\\\\\\\\\\\\\\\\\\\\\\\\\


  DataTable(CalHist,NewFieldCal,100) 'Cal table that store Calibration values

	CardOut(0,100)' only 100 data for checking

	SampleFieldCal

	EndTable ' will get zeroMV/V and Gstrain
```

```
        DataTable(Raw,Store_Raw,-1)' this contains all raw data of strain and displacement Piliwan

        CardOut(0,-1)

        DataInterval(0,0,0,10)

        Sample(1,LVDT_mV       ,IEEE4)

        Sample(8,ST350_mVPV()  ,IEEE4)

        EndTable




        BeginProg


'#########

Flag(8) = True


For R = 1 To 8                                'Do the following to all of Strain

   GStrain(R) = StrainGF(8)                            'Assign default gauge factor (2) to GStrain

 Next R                                        'Repeat above until finished

 For R = 1 To 8 ' already come up with 8

   ScanFlg1x(R) = True

 Next R

 For R = 1 To 8

   GStrainRaw(R) = GStrain(R)

 Next R


 CalFileLoaded = false
```

```
 CalFileLoaded = LoadFieldCal(1)
 FieldcalAvgs = 20
'############


            Scan(100,mSec,1000,0)'Main scan and set up sample rate


'###########
If Flag(8) Then     'Flag 8 zeroing control for the Strain Gages(zeroing calibration).
    If ScanFlg1x(8) Then
      CalStartIdx = 1
      FlagMode8 = 1
      ScanFlg1x(8) = False
    EndIf
  If (FlagMode8 <= 0) OR (FlagMode8 = 6) Then Flag(8) = 0 ' 6 values current status of calibration
  Else
   ScanFlg1x(8) = True
  EndIf
'############


                    VoltDiff(LVDT_mV,1,mV5000,2,True,0,250,1.0,0.0)
                    LVDT_Distance = (LVDT_mV*LVDT_Mult)+LVDT_oSet ' Equation for converting raw data to main by multiply with GF


                    BrFull(ST350_mVPV(),8,mV50,7,Vx2,3,5000,False,False,0,250,1.0,0.0)
```

```
                '\\\\\\\\\\\\\\\\\\\\\\\\\\\\\\\\\\\\\\\\For Mainraw table

                ST350_uStrainraw()=(ST350_mVPV()*ST350_Mult2())+ST350_oSet2() ' Equation for converting raw data to main by multiply with GF

  '///////////////////////////////////




  StrainCalc(ST350_uStrain(),8,ST350_mVPV(),StrainZeroMV(),-4,GStrain(),0) 'Strain calculation, +4 or -4 doesn't matter for data just the direction only

  'When send the program or code, the data will set to be zero automatically no matter whether it has a load applying on or not, it always be zeros.

'   ST350_uStrain() = (ST350_mVPV()-StrainZeroMV())*GStrain()+ST350_oSet() the equation to clarify what StrainClac did


  'Shunt Calibration


FieldCalStrain(43,ST350_uStrain(),1,GStrain(),0,CalMode,SKnownVar(),1,FieldcalAvgs,GStrainRaw(),0)


  'Zeroing Calibration


FieldCalStrain(10,ST350_mVPV(),8,0,StrainZeroMV(),FlagMode8,0,CalStartIdx,FieldcalAvgs,0,ST350_uStrain())

  ST350_uStrain() = ST350_uStrain()*ST350_Mult()




'\ Feed the data tables:


                CallTable Main

                CallTable Mainraw
```

```
                         CallTable Raw

    CallTable CalHist

'/




                 NextScan



        EndProg
```